INFORMATION TO USERS

The most advanced technology has been used to photograph and reproduce this manuscript from the microfilm master. UMI films the text directly from the original or copy submitted. Thus, some thesis and dissertation copies are in typewriter face, while others may be from any type of computer printer.

The quality of this reproduction is dependent upon the quality of the copy submitted. Broken or indistinct print, colored or poor quality illustrations and photographs, print bleedthrough, substandard margins, and improper alignment can adversely affect reproduction.

In the unlikely event that the author did not send UMI a complete manuscript and there are missing pages, these will be noted. Also, if unauthorized copyright material had to be removed, a note will indicate the deletion.

Oversize materials (e.g., maps, drawings, charts) are reproduced by sectioning the original, beginning at the upper left-hand corner and continuing from left to right in equal sections with small overlaps. Each original is also photographed in one exposure and is included in reduced form at the back of the book.

Photographs included in the original manuscript have been reproduced xerographically in this copy. Higher quality 6" x 9" black and white photographic prints are available for any photographs or illustrations appearing in this copy for an additional charge. Contact UMI directly to order.

U·M·I

University Microfilms International
A Bell & Howell Information Company
300 North Zeeb Road, Ann Arbor, MI 48106-1346 USA
313/761-4700 800/521-0600

Order Number 9115737

A closed loop GPS-based orbit trim system for Gravity Probe B

Axelrad, Penina, Ph.D.

Stanford University, 1991

Copyright ©1991 by Axelrad, Penina. All rights reserved.

U·M·I
300 N. Zeeb Rd.
Ann Arbor, MI 48106

A CLOSED LOOP GPS BASED ORBIT TRIM SYSTEM FOR GRAVITY PROBE B

A DISSERTATION SUBMITTED TO THE
DEPARTMENT OF AERONAUTICS AND ASTRONAUTICS
AND THE COMMITTEE ON GRADUATE STUDIES
OF STANFORD UNIVERSITY
IN PARTIAL FULFILLMENT OF THE REQUIREMENTS
FOR THE DEGREE OF
DOCTOR OF PHILOSOPHY

By
Penina Axelrad
October 1990

© Copyright by Penina Axelrad 1991

All Rights Reserved

I certify that I have read this dissertation and that in my opinion it is fully adequate, in scope and quality, as a dissertation for the degree of Doctor of Philosophy.

Bradford W. Parkinson

Bradford W. Parkinson (Principal Advisor)

I certify that I have read this dissertation and that in my opinion it is fully adequate, in scope and quality, as a dissertation for the degree of Doctor of Philosophy.

John V. Breakwell

John V. Breakwell

I certify that I have read this dissertation and that in my opinion it is fully adequate, in scope and quality, as a dissertation for the degree of Doctor of Philosophy.

C.W. Francis Everitt

Approved for the University Committee
on Graduate Studies:

Elizabeth Closs Traugott

Dean of Graduate Studies

ABSTRACT

This dissertation describes an onboard closed loop navigation and control system capable of executing extremely precise orbit maneuvers. In particular, a system to adjust the orbit of the Gravity Probe B (GP-B) spacecraft is developed and evaluated. This onboard system relies on the Global Positioning System (GPS) to provide navigation information directly to the vehicle, thus alleviating the need for extensive ground support.

GP-B is a NASA project designed to measure two relativistic effects on orbiting gyroscopes to an unprecedented accuracy. The exacting science goals of the mission place extremely stringent requirements on the spacecraft orbit. The ideal orbit is circular, polar, and contains the line of sight to a guide star which serves as a distant inertial reference. However, once the experiment begins, the spacecraft will be controlled by a drag compensation system; thus, the only opportunity to adjust the orbit is prior to the start of science data collection. In this research, we specify the *target* injection orbit based on orbit modeling over the entire 18 month mission, in order to best satisfy the ideal conditions on average. The perturbing effects of the geopotential, the Sun and the Moon gravity gradients, and other forces on the orbit are considered. Simulations show that the target inclination must be achieved to an accuracy on the order of 2×10^{-4} deg (25 m) to satisfy the experiment goals.

The design of a GPS based navigation system and onboard orbit trim system is presented. The role of the navigation system is to provide an estimate of the satellite position and velocity state to the control system in a form that can be used to determine the necessary orbit adjustments. This is accomplished by breaking the state estimate into two parts, the target state and linearized deviations from the target. The target state is propagated in closed form including the effects of the Earth oblateness and other significant terms in the geopotential. An extended Kalman filter propagates the linearized state estimate and incorporates information provided by GPS. Two types of GPS receivers are considered: a high quality, dual frequency receiver capable of eliminating the effects of Selective Availability (SA), and a lower accuracy variety which is subjected to SA level errors. Although the navigation accuracy of the lower quality receiver is degraded, both types were found to perform well in the closed loop orbit trim system.

The objective of the trim system is to achieve the target state in minimum time. Actuation is provided by the onboard helium micro-thrusters with maximum specific force of 0.2 μg in each axis. In the linearized dynamical equations, the in-plane and out-of-plane motions are decoupled. The time optimal control calls for maximum authority at all times with the direction determined by a switching curve. Orbit plane maneuvers of 0.01 deg and eccentricity adjustments of 0.001 are demonstrated.

ACKNOWLEDGMENTS

I would like to thank my advisor, Professor Brad Parkinson, for his guidance and encouragement over the past few years. His creative ideas and enthusiasm helped me to overcome stumbling blocks and develop a strong approach to conducting research. The help of Professor John Breakwell has also been invaluable to me. I have learned a great deal from him both through my research and the fascinating courses he offered at Stanford. I feel honored that he has taken the time to carefully read my thesis and provide many useful comments and suggestions. I would also like to thank Professor Francis Everitt, the principal investigator of the Gravity Probe B project, for his helpful suggestions, sound advice, and continued support throughout my studies.

The other members of the GP-B group, both students and staff, have also helped me tremendously, not only in their technical support and ideas, but also by their encouragement and enthusiasm for the various projects I have undertaken. In addition, I would like to thank Richard Vassar for his valuable advice and assistance.

I also wish to express my thanks to Monica Jarnot for her careful editing and proofreading of this manuscript.

The greatest thanks go to my family and friends who have continually and enthusiastically encouraged me throughout my academic career.

This research was sponsored under NASA grant # NAS8-36125.

TABLE OF CONTENTS

Abstract iv

Acknowledgments vi

1 Introduction 1

1.1 Problem Statement 1
1.2 Contributions 3
1.3 Gravity Probe B (GP-B) 3
1.4 Gravity Probe B Launch and Injection 8
1.5 Global Positioning System (GPS) 9
1.6 Thesis Outline 11

2 Orbit Modeling for Gravity Probe B 12

2.1 Introduction 12
2.2 Orbit Requirements 13
  2.2.1 Relativity Drifts 14
  2.2.2 Newtonian Precessions 15
  2.2.3 Altitude Variations 17
2.3 Orbit Perturbation Equations 17
  2.3.1 Disturbing Potential 18
  2.3.2 Disturbing Forces 21
  2.3.3 Euler-Hill Equations 22
2.4 Earth Harmonics 23
  2.4.1 Earth Oblateness 24
  2.4.2 Zonal Harmonics 28
  2.4.3 Tesseral Harmonics 30
2.5 Sun and Moon 42
  2.5.1 Gravity Gradient 44
  2.5.2 Second Order Lunar Effect 46
  2.5.3 Solid Earth Tides 49

2.6 Precession of the Equinoxes 50
2.7 Drag Models 50
  2.7.1 Orbit Injection Drag Model 51
  2.7.2 Long Term Drag Model 52
2.8 Short Term Orbit Motions 53
2.9 Long Term Orbit Motions 56
  2.9.1 Out-of-plane Long Term Results 56
  2.9.2 In-plane Long Term Results 64
2.10 Orbit Modeling and Requirements Summary 64

3 Navigation 67
3.1. Introduction 67
3.2 Navigation Requirements 67
3.3 Coordinate Systems 69
3.4 Global Positioning System 69
  3.4.1 GPS Signal 70
  3.4.2 Antennas 72
  3.4.3 Receiver 73
  3.4.4 Measurements 76
3.5 Navigation Processor 80
  3.5.1 Reference State 82
  3.5.2 Deviation State 83
  3.5.3 Integrity Checking 87
  3.5.4 Antenna Management 88
3.6 Navigation System Performance 90
  3.6.1 Simulation Description 90
  3.6.2 Coverage 96
  3.6.3 High Accuracy Results 97
  3.6.4 Low Accuracy Results 98
  3.6.5 Closed Loop Navigation Results 99

4 Closed Loop Orbit Trim 109
4.1 Introduction........ 109
4.2 Orbit Trim Requirements........ 109
4.3 Control Actuator........ 110
4.4 Controller Reference Orbit........ 111
4.5 Out-of-plane Time Optimal Control........ 113
4.5.1 Algorithm........ 115
4.5.2 Closed Loop Performance........ 116
4.5.3 LQR Control........ 123
4.6 In-plane Time Optimal Control........ 125
4.6.1 Algorithm........ 125
4.6.2 Closed Loop Performance........ 127
4.7 Closed Loop Control System Summary........ 131

5 Summary and Conclusions 132
5.1 Overview........ 132
5.2. GP-B Orbit Modeling........ 132
5.3. GPS Based Navigation System........ 134
5.4. Closed Loop Orbit Trim........ 135

References 137

LIST OF TABLES

2.1 Average Rate of Change of ξ Due to the Odd Harmonics 29
2.2 Amplitude of $\Delta i'$ and $\Delta\Omega$ due to Tesserals Up to $l=5$, $m=5$ 32
2.3 Near Resonances for Polar 650 km GP-B Orbit 34
2.4 Tesseral Terms Contributing to Librational Near Resonances 35
2.5 Maximum Amplitude of $\Delta i'$ and $\Delta\Omega$ Due to Near Resonant Tesserals 37
2.6 Maximum Amplitude of Oscillation in ξ or η for Tesserals Up to $l=5$, $m=5$ 39
2.7 Tesseral Terms Contributing to Dynamical Near Resonances 41
2.8 Sun and Moon Gravitational Potential Parameters 43
2.9 Summary of Long Term Simulation Models 57
2.10 Target Values of i' and Ω for Orbit Injection 57
2.11 Mean and Maximum i' and Ω Due to Inclination Orbit Injection Errors 59
2.12 GP-B Orbit Requirements Summary 66

3.1 GPS Signal Requirements 71
3.2 GPS Receiver Tradeoffs 76
3.3 Simulation Actual Orbit Initialization Errors 95
3.4 High Accuracy GPS Navigation Results 101
3.5 Lower Accuracy GPS Navigation Results 102

4.1 Summary of Out-of-plane Closed Loop Simulation Results 119

LIST OF FIGURES

1.1 Geodetic and Frame-dragging Precessions 4

2.1 Definition of Orbit Elements for GP-B 19
2.2 Hill's Coordinate Frame 23
2.3 Variation of the Instantaneous Eccentricity Vector Due to J_2 27
2.4 Low Order Tesseral Variations of the Coinclination 33
2.5 Low Order Tesseral Variations of the Ascending Node 33
2.6 Out-of-plane Variations Due to 15:1 Resonance 36
2.7 Eccentricity Vector Variations Due to Tesserals up to $l=5$, $m=5$ 40
2.8 Eccentricity Vector Variations for 15:1 Resonance Terms to Degree 36 41
2.9 Geometry for Disturbing Body (Sun or Moon) 43
2.10 Solar Perturbations on the Coinclination and Node 45
2.11 Motion of the Lunar Orbit Plane with Respect to the Earth 47
2.12 Average Secular Rates Due to the Moon 48
2.13 Lunar Orbit Perturbations Launch in 2000 48
2.14 Eccentricity Vector Variations Caused by Second Order Lunar Potential 49
2.15 Short Term Eccentricity Vector Motion 54
2.16 Short Term Out-of-plane Dynamics 55
2.17 Newtonian Gyro Drifts for Nominal Orbit Injection 58
2.18 Long Term Motion of the Coinclination and Node - March 21, 1997 61
2.19 Long Term Motion of the Coinclination and Node - March 21, 2000 62
2.20 Newtonian Gyro Drift - March 21, 1997 63
2.21 Newtonian Gyro Drift - March 21, 2000 63
2.22 Long Term Motion of the Orbit Average Eccentricity Vector 65

3.1 GPS 24 Satellite Constellation 70
3.2 GPS Signal Components 71
3.3 Potential GPS Antenna Locations on the GP-B Spacecraft 73
3.4 Generic Digital Receiver Architecture 75
3.5 GPS Range Errors 78
3.6 Navigation Processor Diagram 81
3.7 Navigation System Simulation Block Diagram 91
3.8 Simulated SA Errors for Low Accuracy Receiver 93
3.9 GPS Satellite Coverage for GP-B 96
3.10 NAV1 Orbit Estimate Errors - Good GPS 103
3.11 NAV1 Deviation State Estimate Errors - Good GPS 104
3.12 NAV4 Orbit Estimate Errors - Poor GPS 105
3.13 NAV4 Deviation State Estimate Errors - Poor GPS, ... 106
3.14 NAV7 Closed Loop Orbit Estimate Errors - Good GPS 107
3.15 NAV8 Closed Loop Orbit Estimate Errors - Poor GPS 108

4.1 Reference Orbit Coinclination 114
4.2 Reference Orbit Ascending Node 114
4.3 Switch Curve for Out-of-plane Control 115
4.4 Optimal Out-of-plane Trajectories in the Z Phase Plane 117
4.5 CON1 Out-of-plane Bang-Bang Control Results - 9 Days 120
4.6 CON2 Out-of-plane Bang-Bang Control Results - 14 Days 121
4.7 CON5 Higher Thrust Control Results - 3 Days 122
4.8 CON6 LQR Out-of-plane Control Results - 9 Days 124
4.9 In-plane Time Optimal Switch Curves 126
4.10 Time Optimal Trajectories for In-plane Control 128
4.11 CON1 In-plane Time Optimal Control Results - 9 Days 129
4.12 CON2 In-plane Time Optimal Control Results - 14 Days 129
4.13 In-plane Results Mean Eccentricity 130

NOTATION

a	- orbit semimajor axis
A_G	- geodetic drift coefficient
A_{FD}	- frame dragging drift coefficient
A	- spacecraft cross sectional area
b	- GPS receiver clock bias
c	- speed of light = 2.99×10^8 m/s
C_{lm}, S_{lm}	- geopotential coefficients of degree l, and order m
d	- drag
$\mathbf{e}$, e	- orbit eccentricity vector and its magnitude
f	- orbit true anomaly
f (Chapt. 3)	- GPS receiver clock drift
f_r, f_θ, f_h	- forces in the direction of $\mathbf{i}_r$, $\mathbf{i}_\theta$, $\mathbf{i}_h$
F_{lmp}	- inclination function
g	- gravitational acceleration at the surface of the Earth = 9.8 m/s^2
G	- gravitational constant
G_{lpq}	- eccentricity function
$\mathbf{h}$, h	orbit angular momentum vector and its magnitude
I_E	- principal moment of inertial of the Earth
i	- orbit inclination
i'	- orbit coinclination
J_2	- Earth oblateness coefficient = 1.082×10^{-3}
$J_{l,m}$	- magnitude of geopotential coefficient of degree l, and order m
k_2	- Love number = 0.3

l	- gravitational potential term degree
M	- mean anomaly
m	- gravitational potential term order
$\mathrm{m_{s/c}}$	- mass of the spacecraft
n	- orbit rate
n_{R}	- reference orbit rate
P	- covariance matrix
$\mathrm{P_0}$, $\mathrm{P_1}$	- Poisson matrices for classical and low eccentricity high inclination orbit elements, respectively
P_{lm}	- Legendre coefficient of degree l and order m
$\mathbf{r}$, r	- position vector from the Earth center to the spacecraft and its magnitude
R_E	- mean equatorial radius of the Earth = 6378 km
$\mathrm{s_{FD}}$	- science gyro drift due to frame-dragging effect
$\mathrm{s_G}$	- science gyro drift due to geodetic effect
$\mathrm{s_{gg}}$	- science gyro drift due to Newtonian torques
t	- time
U	- disturbing potential
u	- orbit argument of latitude $= f + \omega$
u_0	- orbit mean argument of latitude $= M + \omega$
$\mathbf{v}$, v	velocity vector of the spacecraft and its magnitude
w_r, w_θ, w_h	- random forces in the direction of $\mathbf{i}_r$, $\mathbf{i}_\theta$, $\mathbf{i}_h$
x_{H}, y_{H}, z_{H}	- radial, along-track, and out-of-plane positions measured from the center of the hill reference frame

$\boldsymbol{\alpha}$	- orbit element state vector
δ	- declination of an object
δ_R	- declination of Rigel
ζ	- angle between science gyro spin axis and the orbit plane
η	- northward component of the orbit eccentricity vector
λ	- geocentric longitude of satellite subpoint
λ_B	- right ascension of a body
λ_R	- right ascension of Rigel = 78.464 deg
μ_E	- gravitational constant of the Earth = 398600.5 km^3/s^2
μ_M	- gravitational constant of the Moon = 4.903 x 10^3 km^3/s^2
μ_S	- gravitational constant of the Sun = 1.327 x 10^{11} km^3/s^2
v	- spacecraft velocity
ξ	- equatorial component of the orbit eccentricity vector
ρ_i	- pseudo range from user to GPS satellite i
$\dot{\rho}_i$	- pseudo range rate from user to GPS satellite i
$\boldsymbol{\rho}$	- vector of pseudo ranges from user to all visible GPS satellites
ρ	- average atmospheric density
σ	- standard deviation
τ	- time constant
ϕ	- geocentric latitude
Φ	- state transition matrix
ψ	- tesseral driving frequency
ω	- argument of perigee of the orbit
ω_E	- sidereal rotation rate of the Earth

Ω	- right ascension of the ascending node relative to Rigel
Ω_0	- right ascension of the ascending node measured from the vernal equinox J2000
Ω'	- right ascension of the ascending node referenced to the right ascension of the orbit of a disturbing body

Conventions

^	- a hat over a symbol indicates an estimate
$\mathbf{x}$	- bold indicates a vector
$\mathbf{i}$	- bold "i" is a unit vector
$\mathbf{x}^N$	- superscript indicates the reference frame in which the vector is evaluated

CHAPTER 1. INTRODUCTION

1.1 Problem Statement

Advances in sensor technology and onboard processing capability have prompted a shift in the control of many spacecraft functions from ground based commands to onboard closed loop control. For example, autonomous attitude control is routinely performed using sensors, actuators, and digital control logic. In fact, major spacecraft slewing maneuvers, such as those performed during initial acquisition, are carried out under onboard closed loop control. *Orbit* adjustment and major stationkeeping, however, is still carried out by execution of a sequence of commands sent from the ground. This has been driven by the requirement for ground tracking to determine the spacecraft orbit. The advent of the Global Positioning System (GPS) eliminates this constraint by providing position and velocity information of unprecedented accuracy directly to the vehicle.

This dissertation describes an onboard closed-loop navigation and control system capable of executing extremely precise orbit maneuvers. By utilizing GPS navigation information and an onboard controller to perform a precise orbit trim, the system *circumvents the need for extensive ground support.*

The particular application considered is an orbit trim system for NASA's Gravity Probe B (GP-B) spacecraft; however, the same technique is adaptable to other satellite missions. GP-B is a good example because it requires a circular, near Earth, polar orbit which would be useful for other missions such as Earth observation. One unusual aspect of GP-B is that the orbit control system will only be used at the start of the mission to guide the satellite to its target orbit after separation from the launch vehicle upper stage. After this final orbit trim, the spacecraft will follow a "drag-free" orbit, and no additional translational control may be applied. On a more conventional mission, the closed loop system would be employed continuously or perhaps periodically.

The first step in the design of such a system for any space vehicle is to select the appropriate target orbit. For GP-B this involved modeling the orbit motions over the course of the 18 month mission to first of all determine *if* certain stringent requirements could be met, and second to find the optimal initial offsets from the nominal orbit. The results of the orbit modeling studies indicate that a very precise orbit injection must be achieved to meet the tight requirements of the GP-B science mission. Based on this work, it was realized that the launch year would have a significant effect on the orbit motion and on the type of disturbance modeling needed for the science data reduction.

The design of a GPS based navigation system and onboard orbit trim system is presented. The navigation system is required to provide estimates of the GP-B orbit to the onboard controller and to the ground for verification purposes. The controller is designed to adjust the spacecraft orbit to the target in minimum time. The control actuators are continuously operating helium thrusters with a maximum force capability of only about 10 mN. The performance of the closed loop navigation and control system is evaluated via computer simulation. The results demonstrate that the expected range of Delta II injection errors can be corrected in approximately 10 days of controller operation using the helium thrusters.

The following sections summarize the contributions of this work and provide background information on the GP-B mission, the launch vehicle, and the Global Positioning System.

1.2 Contributions

The research described in this dissertation represents a significant development for the GP-B program and serves as a starting point for the design of a similar system for other applications. It has extended earlier work on modeling of the GP-B orbit, and forms the basis for the baseline navigation system design and post launch orbit adjust. The specific contributions may be summarized as follows:

1. Modeled long term orbit motions of the spacecraft orbit.
2. Identified *average* target orbit elements based on the mission start date and determined the allowable injection errors.
3. Derived *instantaneous* target orbit elements to account for significant short term gravitational effects.
4. Outlined the design of a GPS based onboard orbit *determination* system.
5. Developed a *closed loop* control algorithm for orbit trim (utilizing navigation information from GPS) to issue commands to the onboard, low thrust helium actuators.

This work represents the first use of GPS in a closed loop spacecraft application. It draws on past research from both the GP-B program development and the GPS navigation field. It has specific applicability to GP-B and has a broad potential for other spacecraft missions.

1.3 Gravity Probe B (GP-B)

GP-B is a NASA project primarily designed to test two aspects of Einstein's theory of General Relativity. Based on General Relativity, L.I. Schiff predicted that a gyroscope in orbit around the Earth will undergo two motions not predicted by Newtonian analysis. These are known as the *geodetic* and *frame-dragging* precessions. In a precisely polar orbit at an altitude of approximately 650 km, the two effects would be orthogonal, with magnitudes of 6.6 arcsec/yr and 42 marcsec/yr, respectively (Figure 1.1). The GP-B spacecraft, planned to be launched in 1997, will carry extremely sensitive gyroscopes designed to measure these relativity effects to an accuracy of three tenths of a milliarcsecond (0.3 marcsec) or better. The history of the program development, which began about 1963, and the technology applied to solving the problems associated with measuring the relativity effects are described in references such as Everitt [*1980*].

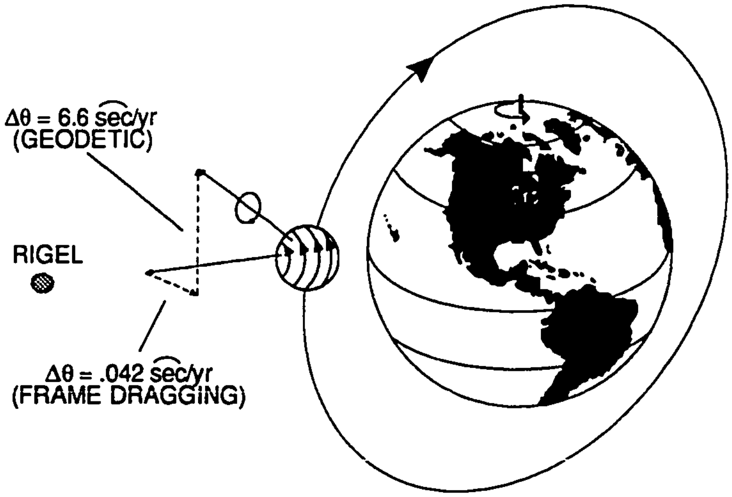

Figure 1.1 Geodetic and Frame-dragging Precessions

Every effort is taken to reduce disturbances which would cause Newtonian drifts of the gyroscopes in order to achieve this unprecedented level of accuracy. The experimental package has been carefully designed making use of cryogenics and superconductivity to create a stable, disturbance-free environment. The relativity gyros are quartz spheres coated with superconducting niobium, electrostatically supported inside a quartz housing. The entire cryogenically cooled experimental package is carried on a "drag-free" satellite which uses proportional helium thrusters to counteract all nongravitational forces acting on the spacecraft. Each of the four gyros is spun up so that its axis is initially aligned with the line of sight to the star Rigel to within a few arcseconds.

The direction to Rigel serves as a "distant inertial" reference against which the relativity drifts are to be compared. A telescope mounted along the vehicle axis of symmetry senses the apparent position of the guide star. The pointing control system will keep the spacecraft aligned toward this image to within 20 marcsec [*Parkinson and Kasdin, 1988*]. Over the course of the experiment, the star image will move due to both the physical drift of the star, known as proper motion, and optical effects such as parallax, deflection of starlight, and annual aberration. All of these effects are well known and can be reliably calibrated and removed in the data reduction.

Proper motion refers to the change in the position of the star relative to very distant objects in the universe. In 1979, Anderson and Everitt calculated that for Rigel this motion was known to better than 1.7 marcsec/yr [*Everitt*, 1980]. They also anticipated that significant improvements in this knowledge would be made prior to the launch of the GP-B spacecraft in the late 1990s. Parallax is an apparent motion of the star with period of one year and amplitude of less than 3 marcsec which is due to the finite distance from the Earth to Rigel [*Everitt, 1980*]. The bending of starlight by the Sun is a relativistic effect which has a yearly period and produces a maximum deflection of the gyroscope of 15 marcsec [*Duhamel, 1984*]. Finally, the annual aberration is due to the component of the velocity of the Earth around the Sun perpendicular to the line of sight to the star. It also has a yearly period with a much larger amplitude of about 20 arcsec [*Vassar, 1982a*]. This large motion provides a very reliable means for calibrating the measurements from the science gyroscopes.

An additional *gyro* drift term must also be identified in the data reduction. A geodetic drift of 19.2 marcsec due to the Sun is expected to occur in the same direction as the frame-dragging effect. This can be accurately calibrated based on the results of the determination of the Earth geodetic effect.

The most difficult errors to correct are Newtonian drifts of the gyros. These drifts would be caused by forces exerted by the suspension system on the *nearly* spherical gyros. The spacecraft has been designed so that most of these forces will average to zero over an orbit or over the 10 minute roll period. However, if the spacecraft symmetry axis does not lie in the orbit plane, gravity gradient torques on the spacecraft will not average to zero, and there will be a net support force exerted on the gyros. Such a misalignment will occur for two reasons: 1) the spacecraft must rotate to track the apparent motion of the star, and 2) the orbit plane will rotate due to perturbing gravitational forces. The largest contributor to the spacecraft rotation is the 20 arcsec annual aberration which must be tracked. This dissertation focuses on the errors which are produced by the orbit plane motion and provides a means for them. Further background information on GP-B can be found in references such as Parkinson et al. [*1986, 1987*].

The orbit of the GP-B satellite is critical to minimize the disturbances on the gyros. Ideally, the spacecraft must follow a purely gravitational path, or geodesic, through space. It should be preferably in a precisely polar orbit which contains the guide star to cause the geodetic and frame-dragging effects to be orthogonal, and as circular as possible to simplify the data reduction. Motions out of the prescribed orbit plane are particularly harmful because they cause Newtonian drifts, described above, which will be difficult to calibrate in the data [*Vassar, 1986*].

In addition to the primary relativity experiment, the spacecraft also may serve as a platform for two co-experiments in geodesy and aeronomy. The objective of the geodesy experiment is to use GPS data collected onboard GP-B to improve the accuracy of the geodetic model of the Earth. It is expected to reduce the GEM T1

Earth Model errors by a factor of more than 100 for coefficients of degree 5 through 32 [*Tapley, et al., 1989*]. The aeronomy experiment uses the data from the drag-free translational control system to determine a better model of the Earth's atmosphere at orbital altitude [*Jafry, 1989*]. Both of these projects require accurate orbit determination and a nearly circular orbit. Thus, a precisely determined orbit is required for relativity, geodesy, and aeronomy objectives. A GPS based navigation system as part of an onboard optimal trim system should also be able to satisfy these needs.

Some previous work has been done on modeling the GP-B spacecraft orbit by Vassar presented in his thesis [*1982b*] and in subsequent reports at Lockheed [*1986*]. In particular, he considered the effect of launch date and orbit inclination on the accuracy of the relativity measurement. Later, he also modeled the solar effect on the orbit plane [*Vassar, 1986*]. Orbit effects on the relativity data were considered by Vassar, Breakwell, and Van Patten [*1982a*]. In his 1977 Ph.D. dissertation entitled "*A Theoretical Analysis of a Relativity Mission with Two Counter-Orbiting Drag-Free Satellites*," Schaechter evaluated the influences of the higher Earth harmonics, Sun and Moon, precession of the equinoxes, and other disturbances on ranging measurements made between two proposed relativity satellites [*1977*].

Orbit modeling and prediction in general has been addressed in a tremendous number of papers. Recent work of satellite geodesists has greatly improved the accuracy of the gravitational model of the Earth. In particular, resonance effects on near Earth satellites have yielded information for individual harmonic coefficients of relatively high order. The orbit modeling performed in this research is based on the approaches presented by Breakwell in the Stanford course AA279B [*1987*]. This thesis represents the most comprehensive study, thus far, of the orbit effects for the current GP-B mission concept.

1.4 Gravity Probe B Launch and Injection

The current plan is to launch the GP-B spacecraft on a two-stage Delta II booster equipped with an improved guidance system [*McDonnell Douglas Inc., 1989; Green, 1990*]. Guidance for the Delta is provided by an inertial system known as DIGS. The currently used configuration does not have the ability to target an inertially fixed orbit plane except through the selection of the launch time and allowable window. A planned upgrade to the onboard computer will rectify this situation in order to permit a payload such as GP-B to target the desired ascending node direction [*Green, 1990*].

The first stage of the Delta II consists of a main engine and nine solid-rocket motor boosters which burn out and separate from the rest of the vehicle after about 250 sec. Following a short coast period, the second restartable stage ignites prompting the release of the payload fairing. At this point, the GPS receiver on the GP-B spacecraft is expected to acquire satellite signals and compute a reliable position and velocity fix. The GPS fix will be provided to the Delta computer in order to calibrate the DIGS gyro misalignments and possibly to reset the onboard position and velocity estimates. This is expected to improve significantly the achievable injection accuracy.

The second stage burns for about 200-400 seconds, and then the vehicle coasts in a Hohmann transfer orbit for about 2900 seconds. The upper stage is then reignited to circularize the orbit. Proper timing of the cutoff should permit accurate attainment of the orbit altitude and eccentricity required, as further discussed below. The vehicle separation from the payload will impart only a minute Δv to the spacecraft.

At this point the GP-B spacecraft will begin its initialization and checkout procedures. An attitude reference must be established to provide coarse information to the onboard navigation and control systems. Thruster calibrations and telemetry and command verifications are then carried out. Calibration of the extremely low force thrusters is critical for translational and attitude control during the science mission.

Once this has been completed, the task of the closed loop orbit trim system begins to maneuver the orbit so as to remove any residual orbit errors left by the booster system. This phase may last about 10-15 days during which time other housekeeping and start-up procedures such as gyro spin-up may also be accomplished.

The task of the onboard GP-B orbit trim system is to adjust the orbit achieved by the booster so that it meets the requirements. For the purposes of this study, two sets of booster injection accuracies are considered. The first is a "poor injection" with errors in the coinclination and node of ± 0.01 deg (1.25 km), and errors in the eccentricity vector of ± 0.0015. The second is a "good injection" with orbit plane errors of ± 0.005 deg (625 m) and eccentricity errors of 0.0007. In both cases we assume altitude errors of ± 0.5 km. These numbers are consistent with the performance expected from the improved Delta II guidance with GPS updates.

1.5 Global Positioning System (GPS)

The NAVSTAR GPS is a satellite based navigation system currently under deployment by the United States Air Force. In its planned configuration it will consist of a constellation of 24 satellites, each broadcasting a highly accurate ranging signal and its own orbital and clock parameters. The signal consists of an L-band carrier, modulated by 1 MHz and 10 MHz identifying codes and a 50 Hz navigation message. A user receiving signals from four or more satellites can passively determine its position and velocity. Further information on GPS can be found in references such as Milliken and Zoller [*1980*], ION [*1980, 1984, 1987*], or Wells et al. [*1986*].

To perform onboard orbit determination, a spacecraft must be equipped with a GPS receiver, a set of antennas, and a navigation processor. Recent advances in GPS receiver technology have made possible highly accurate and reliable units suitable for space applications. These receivers are capable of simultaneously tracking both the code and carrier signals from all GPS satellites in view. Antenna designs have also progressed significantly, resulting in small units which are highly resistant to multipath interference. A minimum of three such antennas must be mounted on the spacecraft to provide continuous tracking of all available satellites. Additional antennas may be required if the spacecraft has large obstructions such as solar panels, or if vehicle attitude is to be derived from GPS as well. The receiver takes signals from the antennas and provides both range and range rate measurements to the navigation processor. Using these state-of-the-art components, GPS range accuracy is expected to be approximately 5 m (1- σ) and range rate accuracy about 0.01 m/s (1- σ). Less accurate measurements will occur during any period when the Air Force deliberately degrades the GPS signals. A more detailed discussion of GPS navigation and error sources will be given in Chapter 3.

In the past five years there has been an explosion of interest in the use of GPS for a wide array of applications. Most near Earth spacecraft planned for the 1990s and beyond- including the Shuttle, Space Station Freedom, and TOPEX- will have GPS receivers onboard performing a broad range of navigation functions [c.f. *Jekeli, 1990*]. The use of GPS in a closed loop system was first suggested by Parkinson and Fitzgibbon for an aircraft automatic landing system [*1989*]. The orbit adjustment system proposed here draws on much of this prior navigation research and ties it together with time optimal control theory for a linear dynamic system.

1.6 Thesis Outline

The following chapters correspond to the three main topics of this research: (1) orbit modeling, (2) spacecraft navigation, and (3) spacecraft translational control. The orbit modeling section describes the orbit requirements for GP-B, the methods used to predict the trajectory of the spacecraft over its 18 month mission, and simulation results used to determine the target injection orbit. Chapter 3 discusses the navigation system design including the basic layout of the GPS receiver and the navigation processor. It illustrates open loop navigation system performance and raises the significant implementation issues. The closed loop orbit trim system is described in Chapter 4. A bang-bang control algorithm is described which adjusts the orbit in minimum time using the onboard helium thrusters. Simulations of the closed loop system performance are presented and discussed. The final chapter summarizes the results and contributions of this work and provides an outline of future study and related applications of the techniques described.

CHAPTER 2. ORBIT MODELING FOR GRAVITY PROBE B

2.1 Introduction

The primary drivers in the selection of an appropriate orbit for the GP-B spacecraft mission are minimization of torques from nongravitational forces on the science gyros, separation of the geodetic and frame-dragging effects, and maximization of the relativity and geodesy data signals. This translates into an ideal orbit which is circular, polar, and contains the guide star, Rigel. Nongravitational disturbances on the orbit during the science mission are reduced to less than 10^{-10} g's through the use of a drag compensation system; however, this precludes any type of orbit adjustments to maintain the nominal orbit. There are three major ramifications: 1) orbit corrections can *only* be performed prior to the start of science data collection, 2) the orbit requirements can only be satisfied on average, and 3) the target injection orbit must be determined very accurately, accounting for the deviations which will occur over the course of the mission. Clearly, *a priori* modeling of the GP-B orbit is critical.

This chapter describes the modeling of the GP-B orbit. The first section provides background on the the orbit requirements. Variational equations are derived for the set of orbit elements used to describe the GP-B orbit in Section 2.3. The following sections develop the models of the perturbations caused by the Earth's noncentral gravitational field, the Sun and Moon, the precession of the equinoxes, and the spacecraft residual drag. Both analytical formulae and numerical simulation results are presented to show the orbit variations over the course of the 18 month GP-B mission.

2.2 Orbit Requirements

The parameters of the spacecraft orbit influence both the relativistic drift and the Newtonian precession of the science gyros. The ideal orbit is circular, polar, and aligned with the direction to the guide star, i.e. Rigel lies within the orbital plane. If such an orbit could be achieved, it would have the following advantages.*

1. Gravity gradient torques on the gyros average to zero over an orbit.
2. Suspension torques on the gyros average to zero over an orbit.
3. Geodetic and frame-dragging effects are orthogonal.
4. Data reduction is simplified.

If the orbit is nearly circular, it has the added benefit of obtaining the minimum average altitude for a given dewar size.

Of course, it is impossible to maintain or even to inject the spacecraft into the nominal orbit perfectly. Thus there will be precessions of the science gyros other than the northerly geodetic and the eastwardly frame-dragging drifts. There are two ways to deal with these disturbances to the relativity signals. The first is to try to reduce the disturbance to an acceptably small level. If this is not possible, the second approach is to account for the disturbance by mathematically modeling it in the data reduction. In practice it is likely that a combination of these methods will be employed. The current goal is to reduce the physical error in the frame-dragging drift to 1% of the expected value, i.e. 0.4 marcsec/yr. Of this we allocate about 0.1 marcsec/yr to errors caused by orbital effects. In the following paragraphs the contributions to the measured science gyro drifts due to orbit deviations from the nominal are summarized and possible calibration methods are briefly discussed. The general recommendation is that deviations from the ideal orbit plane should be reduced to the lowest level possible.

---

* These advantages are only approximate. That is, given the ideal orbit, the Newtonian torques on the gyros will *approximately* average to zero. Further discussion of this can be found in Keiser [*1985*].

2.2.1 Relativity Drifts

The orbit averaged geodetic and frame-dragging drift rates were given by Everitt [*1980*] as follows:

$$\begin{aligned} \dot{s}_G &= A_G \left(\cos i \cos \delta_R - \sin i \sin \delta_R \sin \Omega \right) \hat{E} + A_G \sin i \cos \Omega \, \hat{N} \\ \dot{s}_{FD} &= -\frac{1}{2} A_{FD} \left[\left(1 + 3\cos 2i \right) \cos \delta_R - 3 \sin 2i \sin \delta_R \sin \Omega \right] \hat{E} \\ &\quad - \frac{3}{2} A_{FD} \sin 2i \cos \delta_R \, \hat{N} \end{aligned} \tag{2.1}$$

where the relativity drift constants A_G and A_{FD} are,

$$A_G = \frac{3}{2} \frac{\mu_E \, n}{c^2 a \left(1 - e^2\right)}, \quad A_{FD} = \frac{G \, I_E \, \omega_E}{2 \, c^2 a^3 \left(1 - e^2\right)^{3/2}}. \tag{2.2}$$

and μ_E is the Earth's gravitational constant, I_E is its moment of inertia, and c is the speed of light. The orbit rate is n; a, i, and e, are the semimajor axis, inclination, and eccentricity of the orbit; ω_E is the Earth's sidereal rotation rate. The declination of Rigel is δ_R, and the right ascension of the orbit ascending node, referred to Rigel, is Ω.

For a 650 km circular orbit the computed values of A_G and $A_{FD} \cos \delta_R$ are 6.6 arcsec and 42 marcsec per year, respectively [*Parkinson, et al., 1986*]. Notice that these coefficients would become smaller if the semimajor axis, a, were increased.

By making approximations for small values of the coinclination, i', and node, Ω, Eq. 2.1 becomes

$$\begin{aligned} \dot{s}_G &= A_G \left(i' \cos \delta_R - \Omega \sin \delta_R \right) \hat{E} + A_G \, \hat{N} \\ \dot{s}_{FD} &= A_{FD} \cos \delta_R \, \hat{E} - A_{FD} \, 3 \, i' \cos \delta_R \, \hat{N} \end{aligned} \tag{2.3}$$

Thus the geodetic signal appears primarily in the north direction, whereas the frame-dragging drift is primarily easterly. However, since A_G is two orders of magnitude larger than A_{FD}, we should compare the eastward component of the geodetic drift to the primary frame-dragging term. Substituting the declination of Rigel into Eq. 2.3 gives,

$$\dot{s}_{G_{East}} \approx A_G\,(i' - 0.15\,\Omega) \tag{2.4}$$

In order to separate this term from the frame-dragging drift, we must know the values of the coinclination and node of the orbit to better than about 10^{-3} deg (125 m). The eastward component of the geodetic drift can be determined by first obtaining the geodetic coefficient based on the northward drift alone (the northward frame-dragging drift is negligible). The frame-dragging term is then isolated by estimating and removing the eastward geodetic drift based on $\hat{A}_G$ and the time history of the inclination and node.

2.2.2 Newtonian Precessions

Vassar [*1982b, 1986*] identified and modeled the orbit dependent torques and the resulting Newtonian precessions of the gyroscopes as part of an end to end error analysis of the relativity mission. The most significant drifts are caused by torques produced by the gyro suspension system acting on the nearly perfect gyros. The suspension system keeps each of the science gyroscopes centered within the housing and supports it against residual specific forces including gravity gradients due to the separation of the gyro from the proof mass, centrifugal acceleration due to spacecraft roll, random drag, and disturbances caused by the pointing system.

Vassar found that the largest contribution was due to the gravity gradient forces, and computed the resulting gyro drift rates to first order in the angle between the gyro spin axis and the orbit plane (γ). This angle is given by the following combination of the orbit coinclination (i') and node measured relative to Rigel (Ω) [*Vassar, 1986*].

$$\gamma \equiv i' \sin \delta_R + \Omega \cos \delta_R \tag{2.5}$$

Gyro drifts due to both primary suspension torques caused by the interaction of the support forces counteracting the gravity gradient with the gyro out of roundness, and the secondary suspension torques due to the asphericity of the gyro and the asphericity of its housing were considered. The rotor shape is modeled by a spherical harmonic expansion similar to the model of the Earth's graviational field. Vassar found the dominant component to be the primary torque due to the even terms in the harmonic expansion which produces a northward drift of approximately 500 γ marcsec/ yr, where γ is measured in radians. Thus

$$\dot{s}_{gg} \approx 500 \; (i' \sin \delta_R + \Omega \cos \delta_R) \; milliarc \; sec/yr \tag{2.6}$$

This expression can be integrated using the results of long term simulations of the variations of the orbit plane to determine if the Newtonian drift will be within the desired error margin of 0.1 marcsec. In Section 2.8 it will be shown that this goal ***can*** be achieved if highly precise orbit injection requirements are met.

The suggestion has been made that if the Newtonian drift is in fact significant, it would be possible to calibrate it in the data reduction based on the orbit plane time history. There are several difficulties which might arise in trying to carry out this scheme. For example, the effects of capacitance differences, gyro mis-centering, drifts in the suspension system null, and thermal gradients would be impossible to model and calibrate. It may be possible to extract from the measured data enough information to determine coefficients describing the mean shape of the gyroscopes using techniques developed by Feteih [*1990*], and Cohen [*1990*]. However this would add significant complications to an already difficult data reduction task.

2.2.3 Altitude Variations

The requirement for the GP-B spacecraft to be placed in a nearly circular orbit is based on two objectives - to make the eccentricity small enough that second order terms can be ignored, and to keep the average orbit altitude as low as possible. In order for the spacecraft to remain drag free, the translational control system must have sufficient control authority to compensate for the maximum atmospheric drag, which generally occurs at the perigee of the orbit. Since the dewar must be sized for the altitude at perigee, the minimum average semimajor axis would be achieved by a circular orbit. Unfortunately, as will be shown in Section 2.9.2, the combination of the Earth oblateness and odd harmonic terms, cause even an initially circular orbit to become elliptical. Based on the nominal dewar lifetime, periodic altitude variations of 15 km are considered tolerable; corresponding to a maximum eccentricity of 0.002.

2.3 Orbit Perturbation Equations

Figure 2.1 shows the orbit elements used to describe the GP-B orbit. They are similar to the Delaunay and the equinoctial elements often mentioned in the literature [*Battin, 1987*]. The semimajor axis, a, and right ascension of the ascending node, Ω, in this case referred to Rigel, are two of the classical elements. The coinclination, $i' = \frac{\pi}{2} - i$ is substituted for the inclination, i, to facilitate small angle approximations for the near polar orbit. Because the orbit is nearly circular, the classical perigee angle and true anomaly are poorly defined, so the components of the eccentricity vector in the equatorial plane, ξ, and in the northward direction, η, and the argument of latitude, u, or the mean argument of latitude, u_0, are used instead.

$$\xi = e \cos\omega , \quad \eta = e \sin\omega , \quad u = f + \omega , \quad u_0 = M + \omega \tag{2.7}$$

Disturbing forces exerted on the GP-B spacecraft cause its orbit to deviate from a Keplerian ellipse. For a typical near Earth spacecraft these disturbances are primarily due to the noncentral terms in the gravitational field of the Earth, gravity gradients of the Sun and the Moon, and atmospheric drag. GP-B is unusual in that the drag compensation system will eliminate the atmospheric drag and solar pressure effects on the orbit down to a level of less than 10^{-10} g's. Other sources of orbit perturbations which must be considered are solid Earth tides, precession of the equinoxes, and residual drag.

The effects of these disturbances on the orbit elements can be analyzed using standard variational methods, expressed in terms of either a perturbing potential or force. For small disturbances to a near circular orbit we can model the position and velocity deviations from a Keplerian orbit using the linearized Euler-Hill equations.

2.3.1 Disturbing Potential

The perturbation equations for the classical elements, known as Lagrange's Planetary Equations, are given in Eq. 2.8, where U is any perturbing potential [*Breakwell, 1987*].

$$
\begin{aligned}
\frac{da}{dt} &= 2\sqrt{\frac{a}{\mu_E}}\,\frac{\partial U}{\partial M} \\
\frac{de}{dt} &= -\frac{\gamma}{e\sqrt{\mu_E a}}\left(\gamma\frac{\partial U}{\partial M} - \frac{\partial U}{\partial \omega}\right) \\
\frac{d\omega}{dt} &= \frac{\gamma}{e\sqrt{\mu_E a}}\,\frac{\partial U}{\partial e} - \frac{ctn\, i}{\gamma\sqrt{\mu_E a}}\,\frac{\partial U}{\partial i} \\
\frac{dM}{dt} &= \sqrt{\frac{\mu_E}{a^3}} - 2\sqrt{\frac{a}{\mu_E}}\,\frac{\partial U}{\partial a} + \frac{\gamma^2}{e\sqrt{\mu_E a}}\,\frac{\partial U}{\partial e} \\
\frac{di}{dt} &= \frac{ctn\, i}{\gamma\sqrt{\mu_E a}}\,\frac{\partial U}{\partial \omega} - \frac{1}{\gamma\sqrt{\mu_E a}\,\sin i}\,\frac{\partial U}{\partial \Omega} \\
\frac{d\Omega}{dt} &= -\frac{1}{\gamma\sqrt{\mu_E a}\,\sin i}\,\frac{\partial U}{\partial i}
\end{aligned}
\tag{2.8}
$$

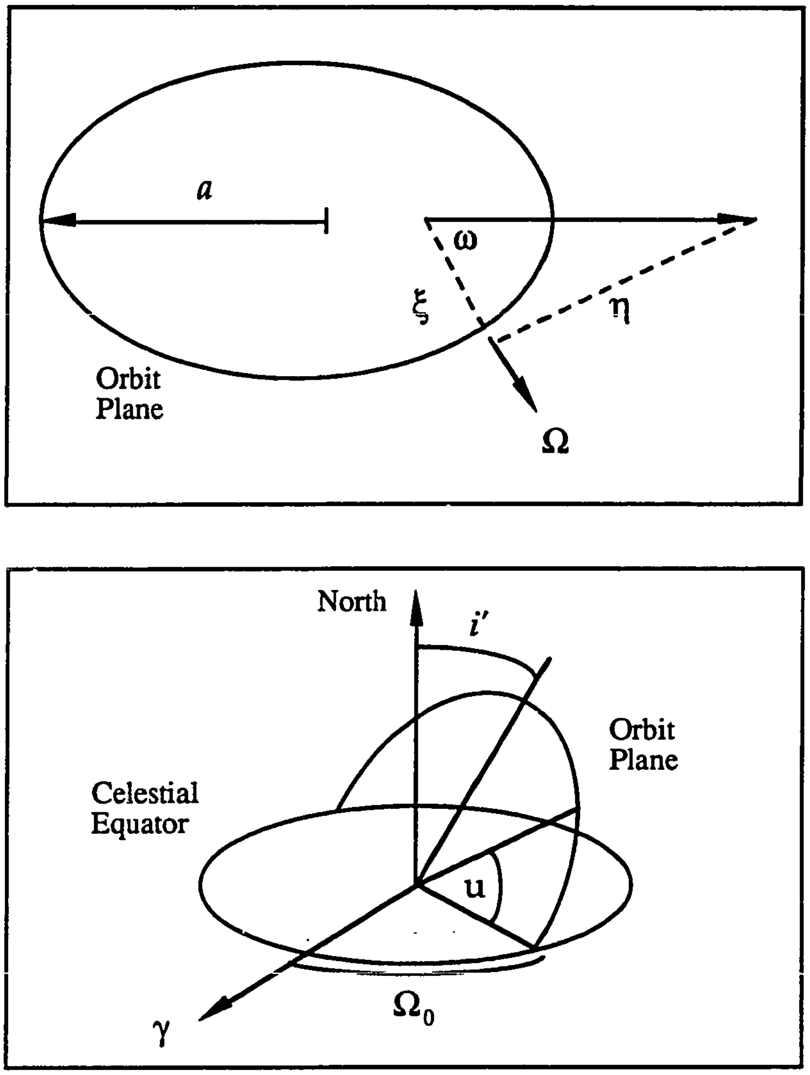
a
ω
ξ
η
Orbit Plane
Ω
North
i'
Orbit Plane
Celestial Equator
u
Ω0
γ

a - semimajor axis

$\xi = e \cos \omega$ - component of e vector in equatorial plane

$\eta = e \sin \omega$ - component of e vector orthogonal to equatorial plane

i' - coinclination

Ω_0- right ascension of the ascending node

u - argument of latitude

Figure 2.1 Definition of Orbit Elements for GP-B.

Eliminates singularities of classical elements for a polar, near circular orbit.

They can also be expressed as

$$\frac{d\boldsymbol{\alpha}_0}{dt} = \mathrm{P}_0 \frac{\partial U}{\partial \boldsymbol{\alpha}_0} \tag{2.9}$$

where $\gamma = \sqrt{1 - e^2}$ and $\boldsymbol{\alpha}_0 = [\, a, e, \omega, M, i, \Omega \,]^{\mathrm{T}}$.
P_0 is known as the Poisson Matrix.

The potential form of the variational equations is particularly useful because there is no explicit dependence on the time variable, M. Thus, to determine the average rate of change of the elements to first order, we need only average the potential, U, and compute the rates using Eq. 2.8.

The perturbation equations for an alternate set of elements, ($\boldsymbol{\alpha}$) can be obtained from [*Broucke* and *Cefola,* 1972]

$$\frac{d\boldsymbol{\alpha}}{dt} = \mathrm{P} \frac{\partial \mathrm{U}}{\partial \boldsymbol{\alpha}} = \left[\frac{\partial \boldsymbol{\alpha}}{\partial \boldsymbol{\alpha}_0}\right] \mathrm{P}_0 \left[\frac{\partial \boldsymbol{\alpha}}{\partial \boldsymbol{\alpha}_0}\right]^{\mathrm{T}} \frac{\partial \mathrm{U}}{\partial \boldsymbol{\alpha}} \tag{2.10}$$

For our set of orbit elements, $\boldsymbol{\alpha} = [\, a, \xi, \eta, u_0, i', \Omega \,]^{\mathrm{T}}$

$$\left[\frac{\partial \boldsymbol{\alpha}}{\partial \boldsymbol{\alpha}_0}\right] = \begin{bmatrix} 1 & 0 & 0 & 0 & 0 & 0 \\ 0 & \cos\omega & 0 & 0 & -e\sin\omega & 0 \\ 0 & \sin\omega & 0 & 0 & e\cos\omega & 0 \\ 0 & 0 & 1 & 0 & 1 & 0 \\ 0 & 0 & 0 & -1 & 0 & 0 \\ 0 & 0 & 0 & 0 & 0 & 1 \end{bmatrix}$$

Then the orbit perturbation equations for the new orbit elements in terms of a disturbing potential become

$$
\begin{aligned}
\frac{da}{dt} &= 2\sqrt{\frac{a}{\mu_E}}\,\frac{\partial U}{\partial u_0} \\
\frac{d\xi}{dt} &= -\frac{\gamma}{\sqrt{\mu_E a}}\frac{\partial U}{\partial \eta} - \frac{\gamma\xi}{(1+\gamma)\sqrt{\mu_E a}}\frac{\partial U}{\partial u_0} - \frac{\tan i'\,\eta}{\gamma\sqrt{\mu_E a}}\frac{\partial U}{\partial i'} \\
\frac{d\eta}{dt} &= \frac{\gamma}{\sqrt{\mu_E a}}\frac{\partial U}{\partial \xi} - \frac{\gamma\eta}{(1+\gamma)\sqrt{\mu_E a}}\frac{\partial U}{\partial u_0} + \frac{\tan i'\,\xi}{\gamma\sqrt{\mu_E a}}\frac{\partial U}{\partial i'} \\
\frac{du_0}{dt} &= \sqrt{\frac{\mu_E}{a^3}} - 2\sqrt{\frac{a}{\mu_E}}\frac{\partial U}{\partial a} + \frac{\gamma\xi}{(1+\gamma)\sqrt{\mu_E a}}\frac{\partial U}{\partial \xi} + \frac{\gamma\eta}{(1+\gamma)\sqrt{\mu_E a}}\frac{\partial U}{\partial \eta} + \frac{\tan i'}{\gamma\sqrt{\mu_E a}}\frac{\partial U}{\partial i'} \\
\frac{di'}{dt} &= \frac{\tan i'\,\eta}{\gamma\sqrt{\mu_E a}}\frac{\partial U}{\partial \xi} - \frac{\tan i'\,\xi}{\gamma\sqrt{\mu_E a}}\frac{\partial U}{\partial \eta} - \frac{\tan i'}{\gamma\sqrt{\mu_E a}}\frac{\partial U}{\partial u_0} + \frac{1}{\gamma\sqrt{\mu_E a}\cos i'}\frac{\partial U}{\partial \Omega} \\
\frac{d\Omega}{dt} &= -\frac{1}{\gamma\sqrt{\mu_E a}\cos i'}\frac{\partial U}{\partial i'}
\end{aligned}
\tag{2.11}
$$

Notice that by changing orbit parameters we have eliminated the eccentricity factor from the denominators as compared to the classical form given in Eq. 2.8. Eq. 2.11 will be used extensively to evaluate the effects of various disturbances on the GP-B orbit.

2.3.2 Disturbing Forces

An alternate set of equations for evaluating the rates of change of the orbit elements due to a disturbing specific force is given by Eq. 2.12 which was obtained from *Small* [*1963*] and *Battin* [*1987*].

$$\begin{aligned}
\frac{da}{dt} &= \frac{2a^2}{h}\left\{ (\xi \cos u + \eta \sin u) f_r + \frac{a\gamma^2}{r} f_\theta \right\} \\
\frac{d\xi}{dt} &= \eta \frac{d\Omega}{dt} \sin i' + \frac{r}{h}\left\{ \psi \sin u f_r + \alpha f_\theta \right\} \\
\frac{d\eta}{dt} &= -\xi \frac{d\Omega}{dt} \sin i' + \frac{r}{h}\left\{ -\psi \cos u f_r + \beta f_\theta \right\} \\
\frac{du}{dt} &= \frac{h}{r^2} - \frac{d\Omega}{dt} \sin i' \\
\frac{di'}{dt} &= -\frac{r}{h} \cos u f_h \\
\frac{d\Omega}{dt} &= \frac{r \sin u}{h \cos i'} f_h
\end{aligned} \tag{2.12}$$

Where

$$\psi = 1 + \xi \cos u + \eta \sin u \,,\ \alpha = \xi + (1+\psi)\cos u \,,\ \beta = \eta + (1+\psi)\sin u$$

$$h = \gamma \sqrt{\mu a} \,,\ r = a\gamma^2/\psi$$

and the disturbing force is expressed in terms of its components f_r, f_θ, and f_h, which act in the radial direction, in the orbit plane perpendicular to $\mathbf{i}_r$, and along the angular momentum vector, respectively. Notice that in these equations the anomaly, u, appears explicitly, so each differential equation must be averaged *after* the expression for the perturbing force has been substituted.

2.3.3 Euler-Hill Equations

In the vicinity of a near circular orbit, linearized position and velocity deviations from Keplerian motion can be modeled by the Euler-Hill equations [*c.f. Kaplan, 1976*].

$$\begin{aligned}
\ddot{x}_H - 2n\dot{y}_H - 3n^2 x_H &= f_r \\
\ddot{y}_H + 2n\dot{x}_H &= f_\theta \\
\ddot{z}_H + n^2 z_H &= f_h
\end{aligned} \tag{2.13}$$

where x_H, y_H, and z_H, are the radial, along track, and out-of-plane positions as shown in Figure 2.2. These equations are particularly useful for looking at short term orbit dynamics, and for the computation of the the orbit adjust commands.

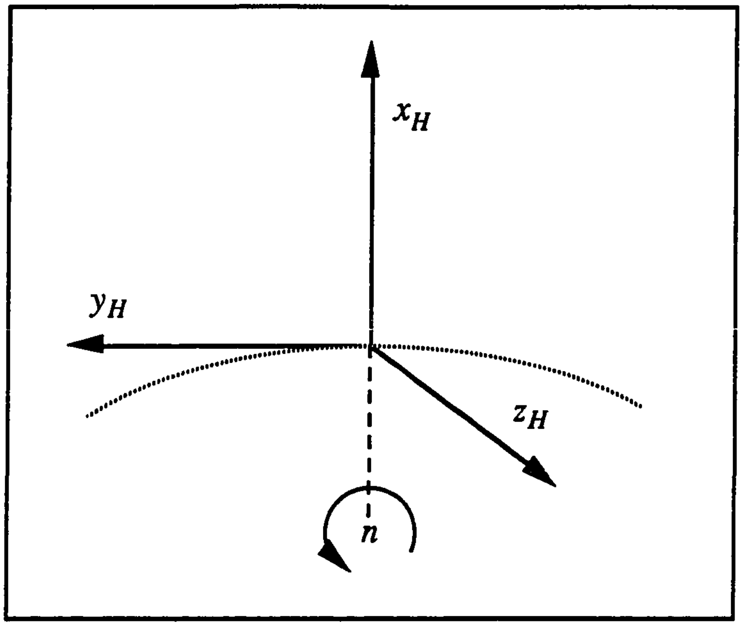

Figure 2.2 Hill's Coordinate Frame.

2.4 Earth Harmonics

In this section the influence of the geopotential on the spacecraft orbit is explored. The Earth oblateness, sometimes referred to as J_2, has the most significant effect on both the orbit plane and the evolution of the eccentricity vector. Various tesseral terms have periodic effects on the orbit, but no significant near resonances were found for the suggested choice of orbit altitude (650 km).

The harmonic expansion of the perturbing geopotential is given by Kaula [*1966*] as,

$$\begin{aligned} U_E &= \sum_{l=2}^{\infty} \sum_{m=0}^{l} U_{lm} \\ &= \sum_{l=2}^{\infty} \sum_{m=0}^{l} \frac{\mu_E R_E^l}{r^{l+1}} \left[C_{lm} \cos m\lambda + S_{lm} \sin m\lambda \right] P_{lm}(\sin\phi) \end{aligned} \tag{2.14}$$

where C_{lm} and S_{lm} are empirically determined coefficients, and P_{lm} are the associated Legendre Functions. The coefficients are often normalized for computation purposes.

$$\bar{C}_{lm} = \left[\frac{(l+m)!}{(l-m)!\,(2l+1)\,(2-\delta_{0m})} \right]^{\frac{1}{2}} C_{lm} \tag{2.15}$$

where $\delta_{0m} = 1$ for $m=0$ and $\delta_{0m} = 0$ otherwise.

The $C_{2,0}$ coefficient is three orders of magnitude bigger than the next largest coefficient. The magnitude of high order normalized coefficients can be approximated by Kaula's rule of thumb as follows, [*Kaula, 1966, p. 98*].

$$|\bar{C}_{lm}| \approx \frac{\sqrt{160} \times 10^{-6}}{\sqrt{2l^4 + l^3}} \approx \frac{10^{-5}}{l^2} \tag{2.16}$$

Terms with $m = 0$, known as the zonal harmonics, depend only on the geocentric latitude (ϕ) of the satellite subpoint. General terms, known as tesserals, have both latitude and geocentric longitude (λ) dependence. For a nearly circular, polar orbit, ϕ and λ can be approximated by, $\sin \phi = \sin u$, $\lambda = \Omega - \omega_E t$.

The following section deals with the U_{20} term by itself, followed by a description of the zonal and tesseral effects.

2.4.1 Earth Oblateness

The Earth's equatorial bulge or oblateness has an unnormalized coefficient $C_{2,0} = -J_2 = -1.082 \times 10^{-3}$. We will see in later sections that the coinclination and node will have variations on the order of 10^{-3} and that the eccentricity will also be of the same order of magnitude. Thus, J_2 will be considered first order small. Substituting $l = 2$, $m = 0$ in Eq 2.14 gives the J_2 potential

$$U_{J2} = -\frac{\mu_E J_2 R_E^2}{a^3 (1-e^2)^3} (1 + e \cos f)^3 \left(\frac{3}{2} \cos^2 i' \sin^2 u - \frac{1}{2} \right) \tag{2.17}$$

One averages this expression over time to obtain the slowly varying part of the potential.

$$\overline{U}_{J2} = -\frac{\mu_E J_2 R_E^2}{a^3\left(1-e^2\right)^{3/2}}\left(\frac{3}{4}\cos^2 i' - \frac{1}{2}\right) \tag{2.18}$$

Eq. 2.11 can then be used to determine the average rates of the orbit elements resulting from the J$_2$ perturbing potential. Keeping terms to second order, (i.e. e^2, η^2, ξJ_2, $i' J_2$, etc.) we obtain the following nonzero average rates for ξ, η, and Ω, and u_0:

$$\begin{aligned}
\frac{d\bar{\xi}_{J2}}{dt} &= \frac{3}{4} n J_2 \frac{R_E^2}{a^2\gamma^4}\eta \\
\frac{d\bar{\eta}_{J2}}{dt} &= -\frac{3}{4} n J_2 \frac{R_E^2}{a^2\gamma^4}\xi \\
\frac{d\bar{\Omega}_{J2}}{dt} &= -\frac{3}{2} n J_2 \frac{R_E^2}{a^2\gamma^4} i' \\
\frac{d\bar{u}_{0J2}}{dt} &= n\left(1 - \frac{3}{2} J_2 \frac{R_E^2}{a^2\gamma^3}\right)
\end{aligned} \tag{2.19}$$

If this were the only disturbance on the orbit, the average eccentricity vector would rotate in the orbit plane at a rate of 6.69 x 10^{-4} rad/orbit (period of 101 days) in the direction opposite the orbit motion. The node would have a secular drift rate of 45.5 i' per year in the same units as i'.

To investigate the short term effects of J$_2$ we use the Hill formulation of Eq. 2.13 with the disturbing forces computed by [*Kechichian, 1989*].

$$\begin{aligned}
f_{rJ2} &= -\frac{3\mu_E J_2 R_E^2}{r^4}\left(\frac{1}{2} - \frac{3}{2}\cos^2 i' \sin^2 u\right) \\
f_{\theta J2} &= -\frac{3\mu_E J_2 R_E^2}{r^4}\cos^2 i' \sin u \cos u \\
f_{hJ2} &= -\frac{3\mu_E J_2 R_E^2}{r^4}\sin i' \cos i' \sin u
\end{aligned} \tag{2.20}$$

A first order closed form solution for this perturbing function is given by Breakwell [*1987*]. The perturbed position and velocity are modeled as deviations from a reference circular orbit with mean radius of r_0, which precesses at a constant rate. To first order in eccentricity and coinclination, this reference orbit is defined as follows.

The reference orbit rate, n_R, is given by

$$n_R \equiv \sqrt{\frac{\mu_E}{r_0^3}} \left\{ 1 - \frac{3}{8} J_2 \left(\frac{R_E}{r_0} \right)^2 \right\} \tag{2.21}$$

The reference orbit precesses about the north pole at the rate

$$\dot{\Omega}_R = -\frac{3}{2} J_2 \left(\frac{R_E}{r_0} \right)^2 n_R \; i' \tag{2.22}$$

The deviations from the reference orbit in the orbit plane are given by

$$\begin{aligned}
\delta r_R &= r_0 \left\{ \frac{1}{4} J_2 \left(\frac{R_E}{r_0} \right)^2 (\cos 2 u_R) - e_0 \cos (u_R - \omega) \right\} \\
\delta u_R &= \frac{1}{8} J_2 \left(\frac{R_E}{r_0} \right)^2 \sin 2 u_R + 2 e_0 \sin (u_R - \omega) \\
\delta \dot{r}_R &= n_R \, r_0 \left\{ -\frac{1}{2} J_2 \left(\frac{R_E}{r_0} \right)^2 (\sin 2 u_R) + e_0 \sin (u_R - \omega) \right\} \\
\delta \dot{u}_R &= \frac{1}{4} n_R J_2 \left(\frac{R_E}{r_0} \right)^2 \cos 2 u_R + 2 e_0 \, n_R \cos (u_R - \omega)
\end{aligned} \tag{2.23}$$

where e_0 is the mean eccentricity of the orbit.

For a 650 km polar orbit with $e_0=0$, the radial position variation is ±1500 m. The instantaneous eccentricity vector varies periodically in both magnitude and direction as illustrated Figure 2.3.

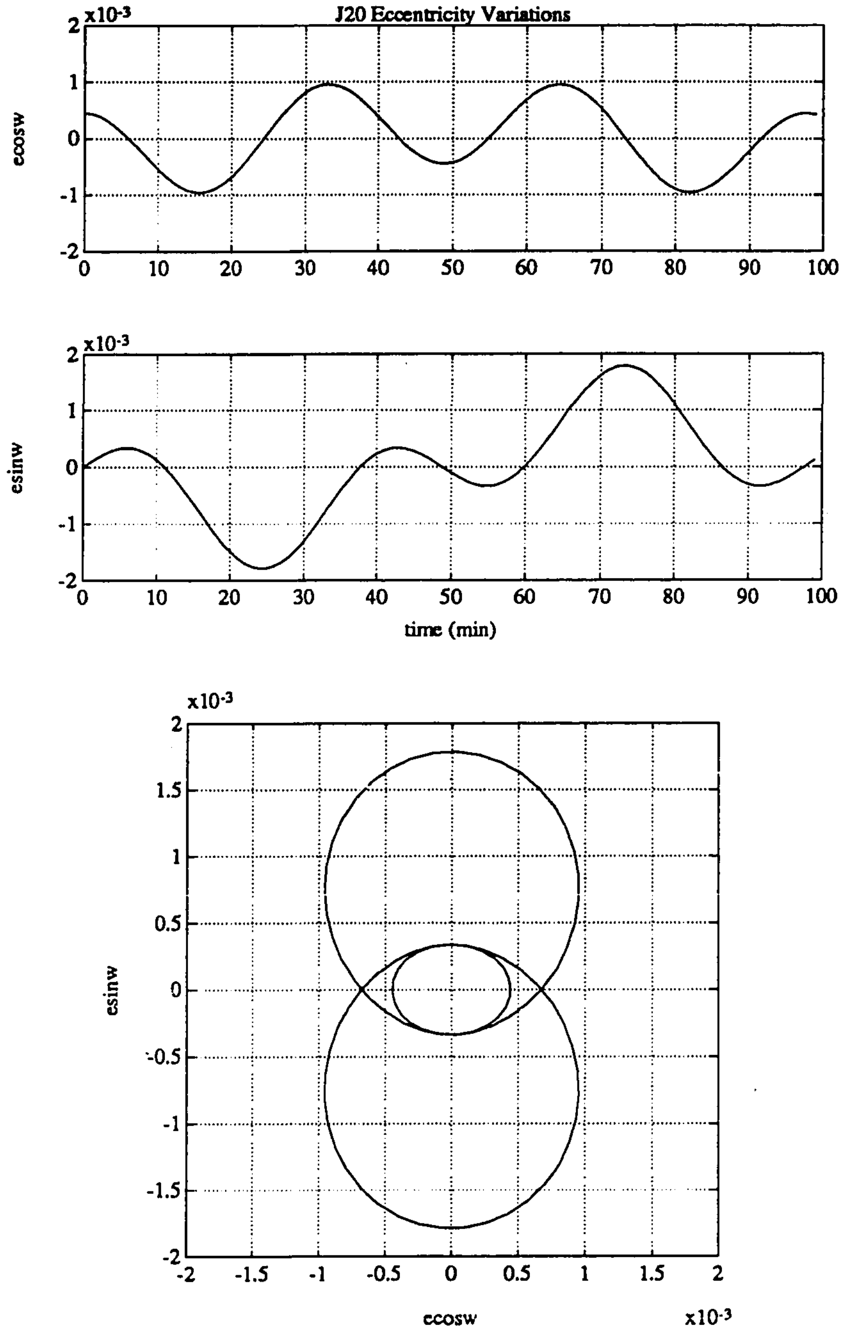

Figure 2.3 Variation of the Instantaneous Eccentricity Vector Due to J_2.

The top two graphs show $\xi = e\cos\omega$ and $\eta = e\sin\omega$ as a function of time. The bottom one illustrates the motion of the instantaneous eccentricity vector over one orbit period.

2.4.2 Zonal Harmonics

The terms in the spherical expansion of the gravitational field which do not depend on longitude are known as zonal harmonics. In this section we discuss the influence of the zonal harmonics of order 3 and higher.

The disturbing potential for each zonal term in the model can be expressed as

$$U_{l,0} = -\frac{\mu_E R_E^l}{r^{l+1}} J_l \; P_l\,(sin\phi\,) \tag{2.24}$$

where $P_l\,(sin\phi) = 2^{-l} \sum_{j=0}^{k} \alpha_{lj} \; sin^{l-2j}\,\phi$

$$\alpha_{l,j} = \frac{(-1)^j\,(2\,l-2j)\,!}{j\,!\,(\,l-j\,)\,!\,(\,l-2j\,)\,!}\,, \quad k = \begin{cases} l\,/2 & for\, l\, even \\ (\,l-1\,)\,/2 & for\, l\, odd \end{cases}$$

For l greater than 2, the average potential over an orbit to first order in e and i' is

$$\begin{aligned} \overline{U}_{l,0} &= -\frac{\mu_E R_E^l J_l}{a^{l+1}\,\gamma^{2l-1}}\,\frac{1}{2\pi}\int_0^{2\pi} (1+e\,cos\,f\,)^{l-1} P_l\,(cos\,i'\,sin\,u\,)\,du \\ &= -\frac{\mu_E R_E^l J_l}{a^{l+1}}\,\frac{1}{2\pi}\int_0^{2\pi} [\,1+(l-1)\,\xi\,cos\,u + (l-1)\,\eta\,sin\,u]\sum_{j=0}^{k} \alpha_{lj}\,sin^{l-2j}\,u\,du \end{aligned} \tag{2.25}$$

To first order, the average potential for the even zonals, J_4, J_6, J_8, etc., does not depend on the orbit elements ξ, η, i', or Ω. Thus the average rates of change of the orbit elements are all zero.

For l odd, the average potential can be expressed as

$$\begin{aligned}\overline{U}_{l\,odd} &= -\frac{\mu_E R_E^l J_l}{a^{l+1}} \frac{1}{2\pi}\int_0^{2\pi} (l\text{-}1)\,\eta \sum_{j=0}^{\frac{l-1}{2}} \alpha_{l\,j}\, sin^{l-2j+1} u\, du \\ &= -\frac{\mu_E R_E^l J_l\,(l\text{-}1)\,\eta}{a^{l+1}} \sum_{j=0}^{\frac{l-1}{2}} \alpha_{l\,j} \frac{(l\text{-}2j+1)\,!}{2^{l-2j+1}\left(\frac{l+1}{2}-j\right)!\left(\frac{l+1}{2}-j\right)!} \\ &= -\frac{\mu_E R_E^l J_l\,(l\text{-}1)\,\eta}{a^{l+1}} P_{l,1}\end{aligned} \tag{2.26}$$

where $P_{l,1} = \sum_{j=0}^{\frac{l-1}{2}} \dfrac{(-1)^{\frac{l-1}{2}-j}(l+2j+1)\,!}{2^{l+2j+1}\left(\frac{l+1}{2}+j\right)!\left(\frac{l-1}{2}-j\right)!\; j\,!\,(j+1)\,!}$

When this is substituted into Eq. 2.11 one finds that each odd term drives ξ at a constant rate given by

$$\frac{d\,\xi_{l\,odd}}{dt} = \sqrt{\frac{\mu_E}{a^3}}\, J_l\, \frac{R_E^l}{a^l}\,(l-1)\,P_{l,1} \tag{2.27}$$

Table 2.1 gives the rates due to J_3 through J_{35}. The sum of the rates is 0.894 x 10^{-6} per orbit. The sum of the odd harmonic rates divided by the rotation rate of the eccentricity vector due to the Earth oblateness, gives the "frozen eccentricity" offset of 0.00134 This will be illustrated in Section 2.9.

TABLE 2.1 Average Rate of Change of ξ (Equatorial component of the eccentricity vector) per orbit due to the odd harmonics.

Degree	Rate (x 10^{-6} per orbit)	Degree	Rate (x 10^{-6} per orbit)	Degree	Rate (x 10^{-6} per orbit)
3	-0.7098	15	-0.0014	27	-0.0013
5	-0.0658	17	-0.0135	29	0.0011
7	-0.0911	19	0.0027	31	-0.0012
9	-0.0278	21	-0.0049	33	-0.0005
11	0.0469	23	0.0106	35	-0.0002
13	-0.0352	25	-0.0026	Total	-0.8940

2.4.3 Tesseral Harmonics

Terms in the gravitational potential given in Eq. 2.14 for which $m \geq 1$, are known as tesseral harmonics. In general they are a function of both latitude and longitude. Sectoral harmonics, for which $l = m$, depend only on longitude. Kaula [*1966, p. 24*] gives the following form for the potential due to a single tesseral of degree l and order m in terms of the spacecraft orbit elements:

$$U_{lm} = \frac{\mu_E}{r}\left(\frac{R_E}{a}\right)^l \sum_{p=0}^{l} \sum_{q=-\infty}^{\infty} F_{lmp}(i)\; G_{lpq}(e)\, J_{lm} \begin{bmatrix} \cos\psi \\ \sin\psi \end{bmatrix}_{l\text{-}m\ odd}^{l\text{-}m\ even}$$

$$\psi = (\,l - 2\,p\,)\,u_0 + q\,M + m\,(\Omega - \omega_E\,t - \varphi_{lm}) \tag{2.28}$$

$$J_{lm} = \sqrt{C_{lm}^2 + S_{lm}^2}\;,\quad \tan(m\varphi_{lm}) = \frac{S_{lm}}{C_{lm}}$$

The inclination function F_{lmp} as expressed by Allan [*1967a*] is

$$F_{lmp}(i) = \frac{(l+m)!}{2^l p!\,(l-p)!} \sum_k (-1)^{k+j} \begin{pmatrix} 2l-2p \\ k \end{pmatrix} \begin{pmatrix} 2p \\ l\text{-}m\text{-}k \end{pmatrix} c^{3l-m-2p-2k}\, s^{m-l+2p+2k} \tag{2.29}$$

where $c = \cos i/2$, $s = \sin i/2$, $j = 0$ for $l - m$ even and $j = 1$ for $l - m$ odd, and k ranges from $\max(0,\, l - m - 2p)$ to $\min(l - m,\, 2l - 2p)$. A normalized inclination function, $\overline{F}_{lmp}$, is also defined such that $\overline{F}_{lmp}\,\overline{J}_{lm} = F_{lmp}\,J_{lm}$. The eccentricity function G_{lpq} is a complicated sum which is of order $e^{|q|}$, with $G_{lp0}(e) = 1$.

Most tesseral terms will have only small periodic effects on the orbit elements; however terms which are nearly commensurate with the orbital period may produce large, long term variations in the inclination, node, eccentricity and semimajor axis. Many papers have been written analyzing orbit resonances, and in fact orbital data from near Earth satellites in near resonance have provided the means to estimate certain high order coefficients very accurately [*c.f. Allan, 1967a,b, 1973*]. In the next two sections the effects of the tesseral harmonics on the GP-B orbit plane, and the spacecraft motion within the orbit plane are described.

2.4.3.1 Out-of-plane Motions

To investigate the change in the coinclination and node of the orbit due to the tesseral harmonics, set e=0, and keep only terms which are first order in i' in Eq. 2.28. Substituting this in the variational equations Eq. 2.11 gives the following expressions for the rate of change of i' and Ω due to a single term U_{lm}.

$$\begin{aligned} \frac{d i'_{lm}}{dt} &= n\left(\frac{R_E}{a}\right)^{l} \sum_{p=0}^{l} F_{lmp}\left(\frac{\pi}{2}\right) m \; J_{lm} \begin{bmatrix} -\sin\psi \\ \cos\psi \end{bmatrix}_{l-m\,odd}^{l-m\,even} \\ \frac{d\Omega_{lm}}{dt} &= -\,n\left(\frac{R_E}{a}\right)^{l} \sum_{p=0}^{l} F'_{lmp}\left(\frac{\pi}{2}\right) J_{lm} \begin{bmatrix} \cos\psi \\ \sin\psi \end{bmatrix}_{l-m\,odd}^{l-m\,even} \end{aligned} \qquad (2.30)$$

where $F'_{lmp}\left(\frac{\pi}{2}-i'\right) \cong \dfrac{(l+m)!}{2^{2l}p!(l-p)!}\sum_{k}(-1)^{k+j}\begin{pmatrix} 2l-2p \\ k \end{pmatrix}\begin{pmatrix} 2p \\ l-m-k \end{pmatrix}(2l-m-2p-2k)$

Thus, one would expect the coinclination and node to vary sinusoidally unless $\dot{\psi}$ is close to zero. The amplitude of these oscillations can be bounded by

$$\begin{aligned} \left|\Delta i'_{lm}\right| &= n J_{lm}\left(\frac{R_E}{a}\right)^{l} \sum_{p=0}^{l} \left|\frac{F_{lmp}\left(\frac{\pi}{2}\right) m}{\dot{\psi}_{lmp}}\right| \\ \left|\Delta\Omega_{lm}\right| &= n J_{lm}\left(\frac{R_E}{a}\right)^{l} \sum_{p=0}^{l} \left|\frac{F'_{lmp}\left(\frac{\pi}{2}\right)}{\dot{\psi}_{lmp}}\right| \end{aligned} \qquad (2.31)$$

Table 2.2 gives the amplitudes for terms in the potential up to degree and order 5.

The largest contributor to the short term inclination variations is the $J_{2,2}$ term. It contains frequency components at $2\omega_E$ and $2(\omega_E \pm n)$. Figure 2.4 illustrates the time history of i' over one day due to all tesserals up to $J_{5,5}$, as well as the i' variation produced by the $J_{2,2}$ term alone for an orbit altitude of 650 km.

The largest nodal variation is due to $J_{4,1}$; however, contributions from $J_{3,1}$ and $J_{4,3}$ are also significant. Figure 2.5 illustrates the variations caused by these three terms and all terms up to fifth order.

TABLE 2.2 Amplitude of $\Delta i'$ and $\Delta\Omega$ due to Tesserals Up to $l = 5$, $m = 5$.

l	m	$\lvert \Delta i' \rvert$ (x 10^{-3} deg)	$\lvert \Delta\Omega \rvert$ (x 10^{-3} deg)	l	m	$\lvert \Delta i' \rvert$ (x 10^{-3} deg)	$\lvert \Delta\Omega \rvert$ (x 10^{-3} deg)
2	1	0.00	0.00	5	1	0.00	0.03
2	**2**	**2.02**	0.13	5	2	0.07	0.11
				5	3	0.07	0.10
3	**1**	0.07	**0.43**	5	4	0.07	0.05
3	2	0.15	0.15	5	5	0.23	0.06
3	3	0.37	0.15				
4	**1**	0.02	**1.16**				
4	2	0.31	0.07				
4	**3**	0.11	**0.47**				
4	4	0.21	0.02				

A ***librational*** resonance occurs when the driving frequency $\dot{\psi}$ associated with a particular harmonic is nearly zero [*Allan, 1967a*]; expressed mathematically as,

$$\begin{aligned} &\dot{\psi} = (\,l - 2\,p\,)\,\dot{u}_0 - m\,\omega_E \approx 0 \\ \text{or}\quad &\dot{\psi} = \alpha\,\dot{u}_0 - \beta\,\omega_E \approx 0 \end{aligned} \tag{2.32}$$

for some integers α and β.

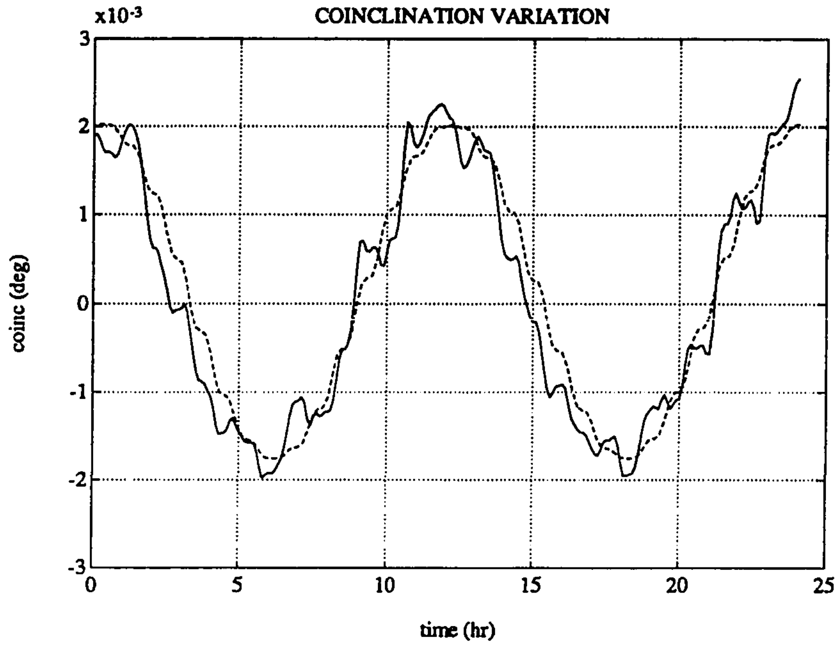

Figure 2.4 Low Order Tesseral Variations of the Coinclination.

Solid line shows the coinclination variations for all terms (l,m) ={(2,1) (2,2) (3,1) (3,2) (3,3) (4,1) (4,2) (4,3) (4,4) (5,1) (5,2) (5,3) (5,4) (5,5) }. Dashed line shows effect of $J_{2,2}$ *only.*

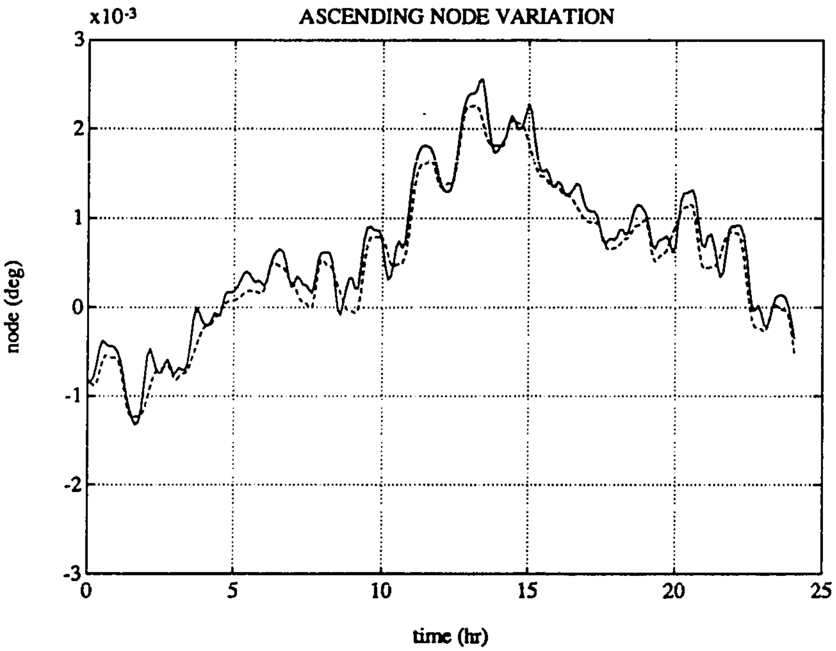

Figure 2.5 Low Order Tesseral Variations of the Ascending Node.

Solid line shows the node variations for all terms (l,m) ={(2,1) (2,2) (3,1) (3,2) (3,3) (4,1) (4,2) (4,3) (4,4) (5,1) (5,2) (5,3) (5,4) (5,5) }. *Dashed line shows combined effects of* $J_{3,1}$, $J_{4,1}$, *and* $J_{4,3}$ *only.*

For any set of orbit rate and Earth rate multipliers α and β, we can compute the orbit altitude for which resonance will occur. (For reasonable accuracy in predicting these altitudes the effect of the Earth oblateness must be included in the orbit rate as in Eq. 2.19.) Table 2.3 lists the closest resonances for terms up to degree and order 60, for a polar orbit at an altitude of 650 km. The exact resonant altitude and the period of the driving frequency for GP-B associated with these near resonances are also shown.

In general, lower order resonances will be stronger than higher order ones because both the normalized geopotential coefficients and inclination functions slowly decrease as the degree and order increase. That is, although the GP-B orbit is closer to the 44:3 resonance than to 15:1, the latter will probably produce a more substantial variation in the orbit elements.

Table 2.3 Near Resonances for Polar 650 km GP-B Orbit.

α	2	3	4	1
β	29	44	59	15
Resonant Altitude (km)	706.5	652.6	626.1	547.9
Period (days)	2.85	40.64	3.32	3.07

Each β/α resonance is composed of contributions from a sequence of tesseral terms, which satisfy the conditions $(l\text{-}2p) = \alpha$, and $m = \beta$. Table 2.4 lists the resonant terms up to degree and order 60. Linear analysis can be used to approximate the element rates for these near resonant terms; however if the computed value for $\dot{\psi}$ is too small, the linear approximations are no longer valid and a more involved analysis must be performed. In this situation the value of $\dot{\psi}$ may vary considerably and secondary influences must be taken into account.

Table 2.4 Tesseral Terms Contributing to Librational Near Resonances.

β/α	(l,m,p) Pairs
29/2	(30,29,14), (32,29,15), (34,29,16), (36,29,17), (38,29,18), (40,29,19), (42,29,20), (44,29,21), (46,29,22), (48,29,23), (50,29,24), (52,29,25), (54,29,26), (56,29,27), (58,29,28)
44/3	(45,44,21), (47,44,22), (49,44,23), (51,44,24), (53,44,25), (55,44,26), (57,44,27), (59,44,28)
59/4	(60,59,28)
15/1	(15,15,7), (17,15,8), (19,15,9), (21,15,10), (23,15,11), (25,15,12), (27,15,13), (29,15,14), (31,15,15), (33,15,16), (35,15,17), (37,15,18), (39,15,19), (41,15,20), (43,15,21), (45,15,22) (47,15,23), (49,15,24), (51,15,25), (53,15,26), (55,15,27), (57,15,28), (59,15,29) (30,30,14), (32,30,15), (34,30,16), (36,30,17), (38,30,18), (40,30,19), (42,30,20), (44,30,21), (46,30,22), (48,30,23), (50,30,24), (52,30,25), (54,30,26), (56,30,27), (58,30,28) (45,45,21), (51,45,24), (57,45,27)

Figure 2.6 shows the coinclination and node variation results from a simulation which includes the terms in 15:1 resonance up to degree 36 over a 6 day period. It is based on the GEM10B coeffecients [*Lerch, et al., 1981*]. Also shown are the variations if only the lowest order term, (15,15,7), is included. Notice that the oscillation in both the inclination and node is clearly dominated by the leading terms and the node variation is neglibly small. The resonant inclination variation is an order of magnitude smaller than the dominant short term variations caused by $J_{2,2}$.

The maximum possible amplitudes of variations of the inclination and node due to the 15:1 and 29:2 resonances were computed for terms up to degree 36 based on the GEM10B coeffecients [*Lerch, et al., 1981*]. They are listed at the top of Table 2.5. The second half of the table shows conservative upper limits for the maximum amplitudes of the variations due to the first resonant term for the 15:1, 29:2, 44:3, and 59:4 near resonances. These approximations were made based on the following.

Using the normalized coefficients and inclination functions, Eq. 2.31 for a single (l,m,p) combination becomes

$$|\Delta i'_{lmp}| = n\bar{J}_{lm}\left(\frac{R_E}{a}\right)^l \frac{\bar{F}_{lmp}(\pi/2)\,m}{\dot{\psi}_{lmp}} \tag{2.33}$$

Then, assuming that the normalized inclination function, $\bar{F}_{lmp}$, is less than or equal to 1, and using Kaula's rule (Eq. 2.16) to approximate $\bar{J}_{lm}$, we find

$$|\Delta i'_{lmp}| < \frac{n\bar{J}_{lm}\left(\frac{R_E}{a}\right)^l m}{\dot{\psi}_{lmp}} \approx \sqrt{\frac{16\times10^{-6}}{2l^4+l^3}}\,\frac{n(0.91)^l m}{\dot{\psi}_{lmp}} \tag{2.34}$$

For each of the near resonances the smallest values of (l,m) from Table 2.4 and the corresponding $\dot{\psi}_{lmp}$ from Table 2.3 were used in this formula to obtain the values in the second half of Table 2.5 below.

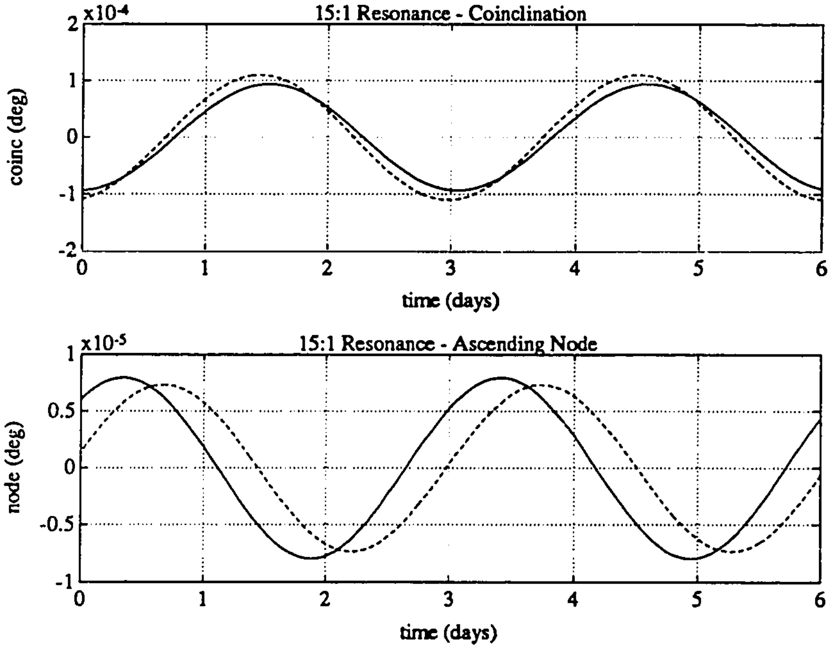

Figure 2.6 Out-of-plane Variations Due to 15:1 Resonance.

Solid lines represent coinclination and node variations due to terms with resonant indices up to degree and order 36. Dashed lines are due to only the (15,15,7) term.

TABLE 2.5 Maximum Amplitude of $\Delta i'$ and $\Delta\Omega$ Due to Near Resonant Tesserals. *For 15:1 and 29:2. Includes only resonant terms up to $l=36$, $m=36$.*

Variations Computed Based on Actual F_{lmp} and GEM 10B Coefficients

β/α	$\lvert \Delta i' \rvert^*$ (deg)	$\lvert \Delta\Omega \rvert^*$ (deg)	$\dot{\psi}$ (rad/s)
15:1	3.07×10^{-4}	1.56×10^{-4}	1.90×10^{-5}
29:2	0.12×10^{-4}	0.04×10^{-4}	3.42×10^{-5}

Conservative Estimates of Variations Based on $F_{lmp}=1$ and Kaula's Rule

β/α	l*	m*	Coinclination Amplitude $\lvert \Delta i' \rvert^*$ (deg)
15:1	15	15	3.5×10^{-4}
29:2	30	29	0.4×10^{-4}
44:3	45	44	0.8×10^{-4}
59:4	60	59	0.0×10^{-4}

It is difficult to precisely predict the effects of higher degree terms for two reasons. First, the coefficients themselves are not well known and second, the usual series expressions for the inclination function, $F_{lmp}(i)$, such as that given in Eq. 2.26, require infinite precision for large values of l. Recursive [*Kostelecky, 1986*], and FFT methods [*Goad, 1987*] have been developed recently for determining these coefficients reliably; however, these techniques require substantial computational and storage capabilities and are beyond the scope of this work.

The work that we have done indicates that the largest variation for GP-B is due to the first few terms in the 15:1 resonance. The simulation results show a $\pm\ 2 \times 10^{-5}$ deg variation in the coinclination, and an even smaller oscillation in the node. The *rate of change* in these elements due to any one high order resonant tesseral term, (l^*, m^*), can be bounded as follows. Kostelecky, et al. [*1986*] have demonstrated, for m in the range of 6 to 30, and l up to order 1000, that the normalized inclination functions for resonant indices slowly decrease with l. Then, assuming at worst the inclination function is constant, and again using Kaula's rule for $\bar{J}_{lm}$,

$$\begin{aligned} \frac{d i'_{l^*m^*}}{dt} &\sim 10^{-3}(0.91)^l \, \frac{10^{-5}}{l^2} m \\ \frac{d \Omega_{l^*m^*}}{dt} &\sim -\, 10^{-3}(0.91)^l \, \frac{10^{-5}}{l^2} (2l - m - 2p) \end{aligned} \qquad (2.35)$$

Since these rates are decreasing in l, and even the 15:1 and 29:2 resonance terms up to degree and order 36 were not found to produce substantial changes in i' and Ω, we can expect that higher order terms in the Earth's gravitational field will not have a significant effect on the GP-B orbit plane.

For GP-B we have the flexibility to select the semimajor axis of the orbit so as to avoid low order resonances. Based on these preliminary analyses, it appears that the suggested altitude of 650 km achieves this desired objective. The period of oscillations associated with the 15:1 resonance is three days is fairly short. A long 41 day resonance occurs for β/α=44/3, which is of high enough order that the effects appear to be negligible for long term orbit modeling purposes. If future work indicates otherwise, the orbit altitude can be adjusted accordingly.

2.4.3.2 In-plane Motions

To investigate the in-plane effects of the tesseral harmonics it is necessary to reintroduce terms in the series expansion of Eq. 2.25 to first order in e. Doing this and substituting the perturbing potential in Eq. 2.8, gives the following rates for the components of the eccentricity vector [*Allan, 1967b*].

$$\frac{d\xi_{lm}}{dt} = n\left(\frac{R_E}{a}\right)^l J_{lm} \sum_{p=0}^{l} F_{lmp}\, G^{+}_{lp} \begin{bmatrix} \cos\ \psi^{+} \\ \sin\ \psi^{+} \end{bmatrix}^{l\text{-}m\ even}_{l\text{-}m\ odd} + F_{lmp}\, G^{-}_{lp} \begin{bmatrix} \cos\ \psi^{-} \\ \sin\ \psi^{-} \end{bmatrix}^{l\text{-}m\ even}_{l\text{-}m\ odd}$$

$$\frac{d\eta_{lm}}{dt} = n\left(\frac{R_E}{a}\right)^l J_{lm} \sum_{p=0}^{l} F_{lmp}\, G^{+}_{lp} \begin{bmatrix} \sin\ \psi^{+} \\ -\cos\ \psi^{+} \end{bmatrix}^{l\text{-}m\ even}_{l\text{-}m\ odd} + F_{lmp}\, G^{-}_{lp} \begin{bmatrix} -\sin\ \psi^{-} \\ -\cos\ \psi^{-} \end{bmatrix}^{l\text{-}m\ even}_{l\text{-}m\ odd} \tag{2.36}$$

The maximum amplitude of the variation in either component of the eccentricity vector which is possible, due to tesseral harmonics up to degree five is given in Table 2.6. Figure 2.7 illustrates the net effect of these terms over a two day period. Clearly these oscillations are negligible in comparison to the variation caused by the earth oblateness shown in Figure 2.3.

TABLE 2.6 Maximum Amplitude of Oscillation in ξ or η for Tesserals Up to *(5,5)*.

l	*m*	*Amplitude* ($\times 10^{-5}$)	*l*	*m*	*Amplitude* ($\times 10^{-5}$)	*l*	*m*	*Amplitude* ($\times 10^{-5}$)
2	1	0.00	4	1	0.15	5	1	0.06
2	2	1.06	4	2	0.32	5	2	0.90
			4	3	0.28	5	3	0.34
3	1	1.30	4	4	0.18	5	4	0.21
3	2	1.04				5	5	0.54
3	3	1.31						
						total		7.69

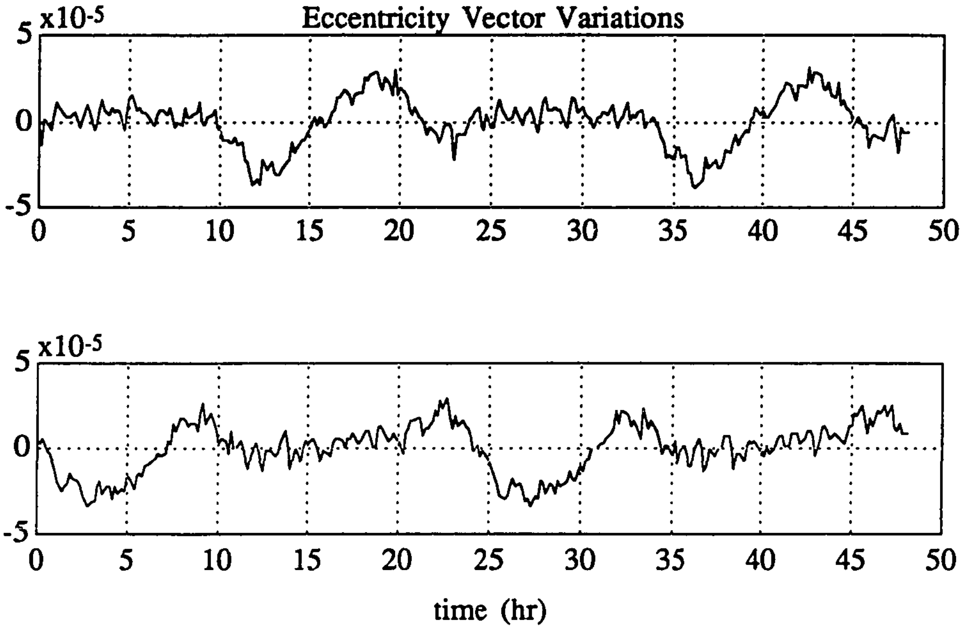

Figure 2.7 Eccentricity Vector Variations Due to Tesserals up to *l* =5, *m*=5.

As in the out-of-plane motions, a resonance will occur when $\dot{\psi}$ is near zero. In this case, however, the resonant perturbing force is periodic at the orbital frequency. Blitzer (*1966*) termed these in-plane effects, *dynamical* resonances. Expressed mathematically, the resonant condition is given by [*Allan, 1967b*],

$$\begin{aligned} &\dot{\psi} = (l - 2p \pm 1)\, \dot{u}_0 - m\, \omega_E \approx 0 \\ \text{or}\quad &\dot{\psi} = \alpha\, \dot{u}_0 - \beta\, \omega_E \approx 0 \end{aligned} \tag{2.37}$$

Thus, the same β/α combinations considered for the out-of-plane motions will cause in-plane resonances, but the resonant indices are different (Eq. 2.32). For each (l^*,m^*) pair there are two resonant values of p corresponding the +1 and -1 values of q. Table 2.7 lists the in-plane near resonant indices up to degree 36 and Figure 2.8 illustrates the variation of the components of the eccentricity vector due only to the terms in 15:1 resonance. The eccentricity vector has an amplitude of less than 2×10^{-6} and rotates clockwise in the plane with the period of 3.0 days associated with the 15:1

near resonance. This variation is insignificant in comparison to the short term changes produced by J_2 and does not have a long enough period to cause long term effects as did the odd zonal harmonics. If the spacecraft were in an orbit closer to a low order resonant altitude, tesseral terms could contribute slow or nearly constant offsets to the eccentricity vector which would appear similar to the odd zonal harmonics discussed in Section 2.4.2. Again the higher order tesseral terms in near resonance ($l \geq 44$, and $l \geq 59$) are expected to produce extremely small variations.

Table 2.7 Tesseral Terms Contributing to ***Dynamical*** Near Resonances.

β/α	(l,m,p) Pairs
29/2	(30,29,14), (32,29,15), (34,29,16), (36,29,17), (30,29,15), (32,29,16), (34,29,17), (36,29,18),
15/1	(16,15,7), (18,15,8), (20,15, 9), (22,15,10), (24,15,11), (26,15,12), (28,15,13), (30,15,14), (16,15,8), (18,15,9), (20,15,10), (22,15,11), (24,15,12), (26,15,13), (28,15,14), (30,15,15), (32,15,15), (34,15,16), (36,15,17), (31,30,14),(33,30,15),(35,30,16) (32,15,16), (34,15,17), (36,15,18), (31,30,15),(33,30,16),(35,30,17)

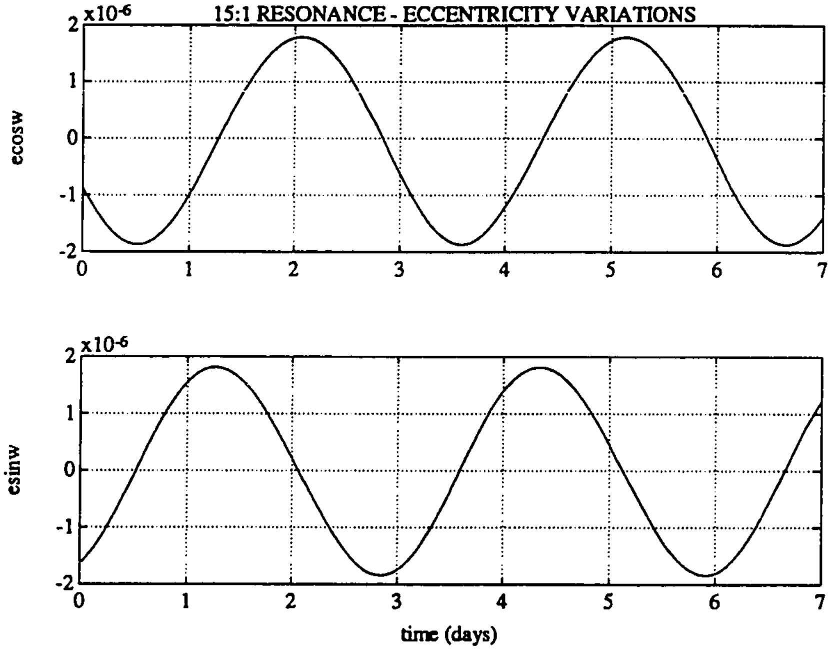

Figure 2.8 Eccentricity Vector Variations for 15:1 Resonance - Terms to $l = 36$.

2.5 Sun and Moon

The Sun and Moon affect the motion of the spacecraft both directly and indirectly through the solid Earth tides. In this section, the influence of the Sun and Moon is derived and computed. The primary gravity gradient effect of each body is a drift consisting of secular and periodic components in the coinclination and node. The second order effect of the Moon can influence the motion of the eccentricity vector; however, for GP-B it turns out to be negligible.

The potential due to a distant mass is given by

$$U_B = \frac{\mu_B}{|\mathbf{r}_B - \mathbf{r}|} - \frac{\mu_B\ \mathbf{r}_B \cdot \mathbf{r}}{r_B^3}$$

$$= \frac{\mu_B}{r_B} + \sum_{l=2}^{\infty} \frac{\mu_B\, r^l}{r_B^{l+1}} P_l(\, \mathbf{i}_B \cdot \mathbf{i}_{S/C}\,) \tag{2.38}$$

where μ_B is the gravitational constant of the disturbing body, r_B is the distance to the body, and P_l is the Legendre function of the angle between the spacecraft and the disturbing body at the Earth center. $\mathbf{i}_{S/C}$ and $\mathbf{i}_B$ represent unit vectors pointing from the center of the Earth toward the spacecraft and the disturbing body, respectively.

If Eq. 2.38 is expanded to third order in $\frac{r}{r_B}$, one obtains

$$\begin{aligned} U_B &= \frac{\mu_B}{r_B} + \frac{\mu_B}{r_B}\left(\frac{r}{r_B}\right)^2 \left[\frac{3}{2}(\, \mathbf{i}_B \cdot \mathbf{i}_{S/C})^2 - \frac{1}{2}\right] \\ &\quad + \frac{\mu_B}{r_B}\left(\frac{r}{r_B}\right)^3 \left[\frac{5}{2}(\, \mathbf{i}_B \cdot \mathbf{i}_{S/C})^3 - \frac{3}{2}(\, \mathbf{i}_B \cdot \mathbf{i}_{S/C})\right] \end{aligned} \tag{2.39}$$

Table 2.8 provides the data for the Sun and Moon needed to compute the potential. The gradient potential for the Moon is about 4 x 10^{-6} km^2/s^2 and for the Sun, 2 x 10^{-6} km^2/s^2. The *second* order lunar and solar potentials are on the order of 8 x 10^{-8} km^2/s^2 and 9 x 10^{-11} km^2/s^2, respectively. Thus, the second order solar term is negligible.

Table 2.8 Sun and Moon Gravitational Potential Parameters.

	μ_B (km^3/s^2)	r_B (km)	r/r_B	$\frac{\mu_B}{r_B^3}$ (sec^{-2})	$\frac{\mu_B}{r_B^3} r^2$ (km^2/sec^{-2})
Sun	1.327×10^{11}	1.496×10^{8}	4.7×10^{-5}	3.96×10^{-14}	1.96×10^{-6}
Moon	4.903×10^{3}	3.844×10^{5}	1.8×10^{-2}	8.63×10^{-14}	4.28×10^{-6}

The potential can be expressed in terms of the spacecraft orbit elements and the right ascension and declination of the perturbing body by making the following substitutions based on Figure 2.10.

$$\begin{aligned} \mathbf{i}_{s/c} &= \cos\phi \;\; \cos\alpha \;\; \mathbf{i}_1 + \cos\phi \;\; \sin\alpha \;\; \mathbf{i}_2 + \sin\phi \;\; \mathbf{i}_3 \\ \mathbf{i}_B &= \cos\delta_B \;\; \cos\alpha_B \;\; \mathbf{i}_1 + \cos\delta_B \;\; \sin\alpha_B \;\; \mathbf{i}_2 + \sin\delta_B \;\; \mathbf{i}_3 \end{aligned} \qquad (2.40)$$

Notice that the longitudes, right ascensions, and orbit node (Ω') are referred to the direction of the equatorial crossing of the perturbing body ($\mathbf{i}_2$).

For a nearly circular, nearly polar orbit, to first order in i',

$$\begin{aligned} &\alpha = \Omega' + \Delta\alpha, && \sin\phi = \sin u, \\ &\cos\phi \;\; \cos\Delta\alpha = \cos u, && \cos\phi \;\; \sin\Delta\alpha = i' \sin u. \end{aligned} \qquad (2.41)$$

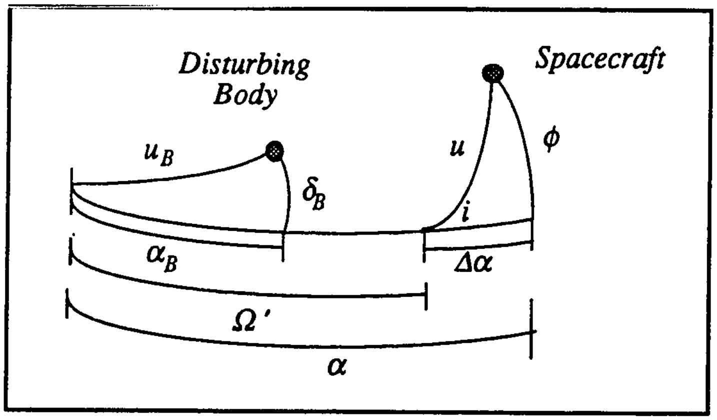

Figure 2.9 Geometry for Disturbing Body (Sun or Moon).

2.5.1 Gravity Gradient

The second term in Eq. 2.39 represents the potential of a gravity gradient torque acting on the spacecraft orbit. If this term is averaged over an orbital period and expressed in terms of the position of the disturbing body as follows:

$$\overline{U}_{B1} = \frac{\mu_B\, a^2}{r_B^3}\left[-\frac{1}{2}+\frac{3}{4}\left(\cos^2(\alpha_B-\Omega')\cos^2\delta_B + \sin^2\delta_B + i'\sin(\alpha_B-\Omega')\sin 2\delta_B\right)\right] \tag{2.42}$$

Then the average rates of change of i' and Ω due to the Sun and Moon can be computed from Eq. 2.11.

We find that

$$\begin{aligned}\frac{d\overline{i'}_{B1}}{dt} &= \frac{3}{4}\,\frac{\mu_B}{n\, r_B^3}\,\sin 2\,(\alpha_B-\Omega')\cos^2\delta_B\\ \frac{d\overline{\Omega}_{B1}}{dt} &= -\frac{3}{4}\,\frac{\mu_B}{n\, r_B^3}\,\sin(\alpha_B-\Omega')\sin 2\delta_B\end{aligned} \tag{2.43}$$

These rates can also be expressed in terms of the argument of latitude, u_B, and inclination, i_B, of the "orbit" of the perturbing body around the earth, by expanding Eq. 2.43, and making the following substitutions:

$$\begin{aligned}&\sin\delta_B = \sin i_B \sin u_B\\ &\cos\delta_B \cos\alpha_B = \cos u_B\\ &\cos\delta_B \sin\alpha_B = \cos i_B \sin u_B\end{aligned} \tag{2.44}$$

Then the average rates become

$$\begin{aligned}\frac{d\overline{i'}_{B1}}{dt} &= -\frac{3}{8}\frac{\mu_B}{n\, r_B^3}\Big\{ \sin 2\Omega' \sin^2 i_B\\ &\qquad - 2\cos 2\Omega' \cos i_B \sin 2u_B + \sin 2\Omega'\,(1+\cos^2 i_B)\cos 2u_B\Big\}\\ \frac{d\overline{\Omega}_{B1}}{dt} &= -\frac{3}{8}\frac{\mu_B}{n\, r_B^3}\Big\{ \sin 2i_B \cos\Omega'\\ &\qquad - \sin 2i_B \cos\Omega' \cos 2u_B - 2\sin i_B \sin\Omega' \sin 2u_B\Big\}\end{aligned} \tag{2.45}$$

The form given in Eq. 2.45 is particularly useful because it immediately shows that a perturbing body will contribute a secular drift plus a periodic term at twice the rate at which the body orbits the earth. The secular part is simply the first term in each of the expressions above.

Thus, the Sun will cause a secular drift plus a twice yearly oscillation in both inclination and node. The secular drift is approximately -1.6×10^{-3} deg/yr in coinclination, and -3.7×10^{-3} deg/yr in the right ascension of the node. Figure 2.10 illustrates the orbit variations due only to the Sun.

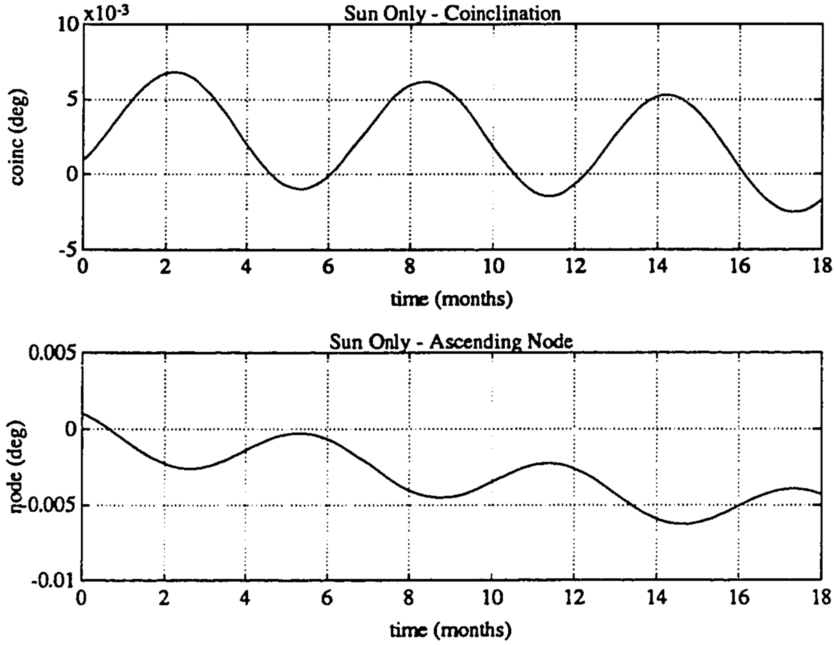

Figure 2.10 Solar Perturbations on the Coinclination and Node.

Secular drift plus twice yearly variation in coinclination and ascending node.

The Moon also produces a secular drift plus a twice *monthly* variation; however, the magnitude of the secular term depends on the position of the lunar orbit in its 18.6 year precessional cycle around the ecliptic pole. Figure 2.11 shows the motion of the lunar pole with respect to the ecliptic pole and the north pole of the Earth. In the top figure the 5 deg cone which the lunar orbit normal traverses about the ecliptic pole is illustrated. Notice that during part of the cycle it just crosses the nominal GP-B orbit plane. The second two plots of Figure 2.11 give the approximate time history of the lunar orbit plane inclination and node for the years 1990-2010.

The orbit plane secular drift rates as a function of the lunar motion are shown in Figure 2.12. Finally, Figure 2.13 illustrates the total first order lunar effect on the orbit plane for an 18 month mission beginning in the year 1997.

2.5.2 Second Order Lunar Effect

The third term in Eq. 2.39 can be expressed in terms of the spacecraft orbit elements and the perturbing body right ascension and declination as follows,

$$\overline{U}_{B2} = -\frac{75}{16}\frac{\mu_B a^3}{r_B^4}\left(\xi\ C_\eta + \eta\ C_\xi\right) \tag{2.46}$$

where $C_\eta = cos^3(\alpha_B\text{-}\Omega')cos^3\delta_B + cos(\alpha_B\text{-}\Omega')\ sin^2\delta_B\ cos\,\delta_B - \frac{4}{5}\,cos(\alpha_B\text{-}\Omega')\ cos\,\delta_B$

$C_\xi = sin^3\delta_B + cos^2(\alpha_B\text{-}\Omega')\ sin\,\delta_B\ cos^2\delta_B - \frac{4}{5}\,sin\ \delta_B$

The rates of change of the orbit elements ξ, and η due to the second order lunar perturbing potential are then derived from Eq. 2.11.

$$\begin{aligned} \frac{d\overline{\xi}_{B2}}{dt} &= \frac{75}{16}\,\frac{\mu_B}{n\,r_B^3}\left(\frac{a}{r_B}\right)C_\xi \\ \frac{d\overline{\eta}_{B2}}{dt} &= -\frac{75}{16}\,\frac{\mu_B}{n\,r_B^3}\left(\frac{a}{r_B}\right)C_\eta \end{aligned} \tag{2.47}$$

Figure 2.14 illustrates the evolution of the eccentricity vector described by this equation. Clearly, the effect of the second order lunar term is negligible in comparison to the Earth zonal harmonics.

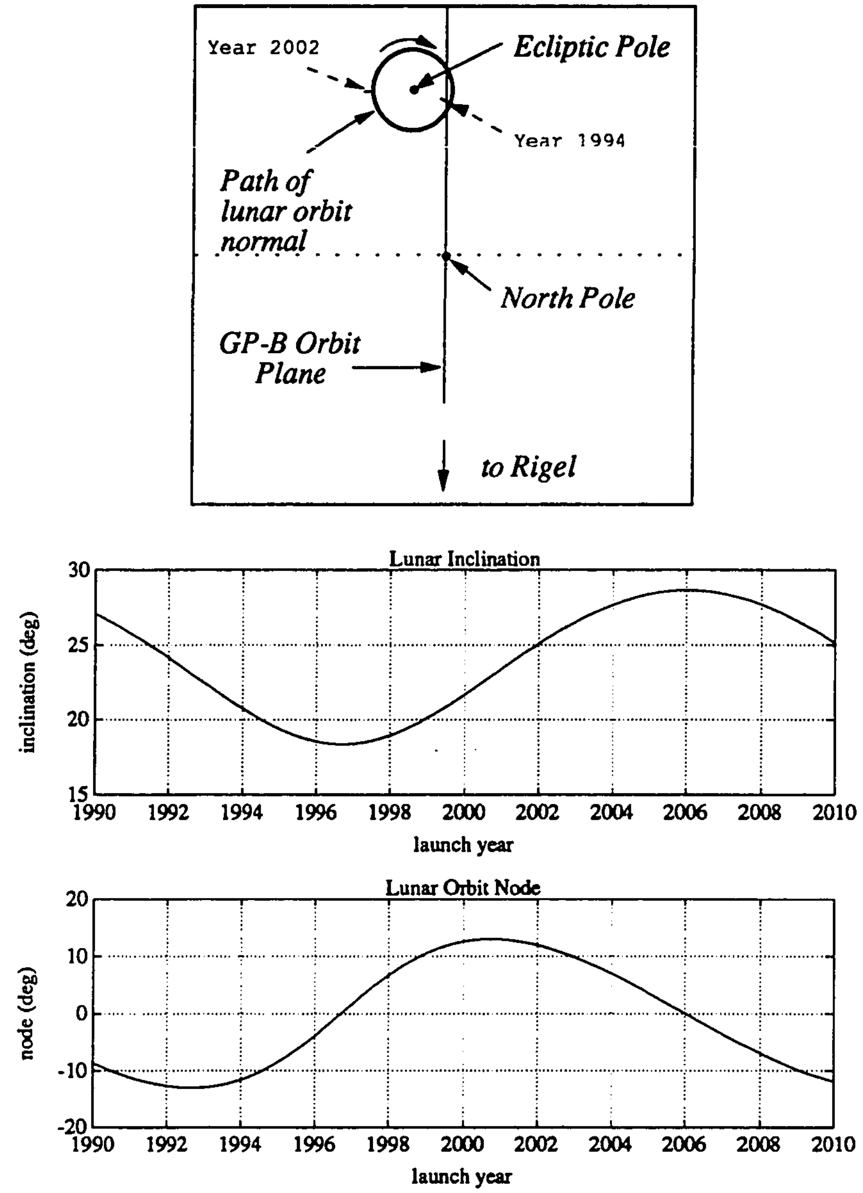

Figure 2.11 Motion of the Lunar Orbit Plane with Respect to the Earth.

The top figure shows the relative positions of the Earth's North Pole, the Eliptic Pole and the normal to the lunar orbit plane. The second two figures give the variation in the inclination and node of the lunar orbit plane over its 18.6 year precessional cycle.

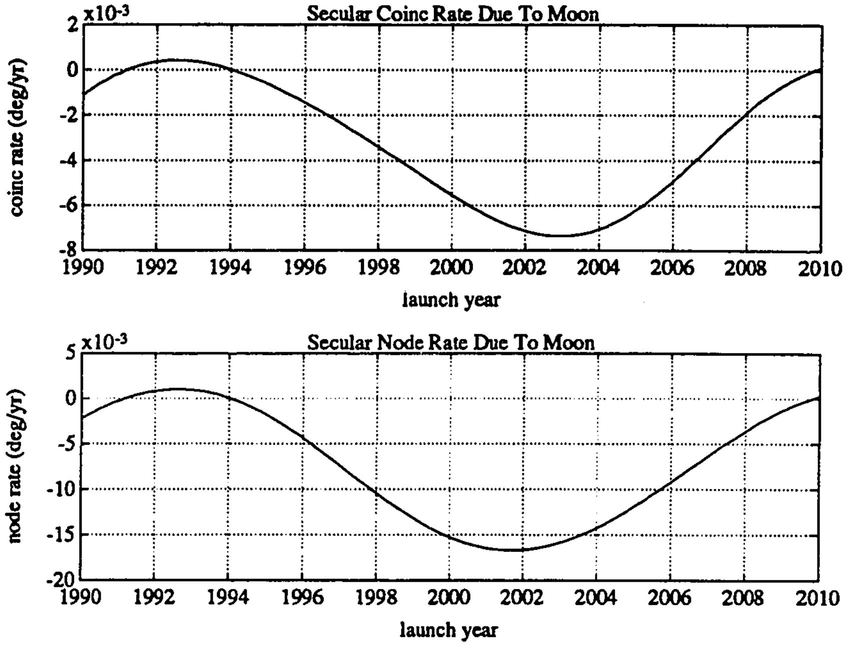

Figure 2.12 Average Secular Rates Due to the Moon.

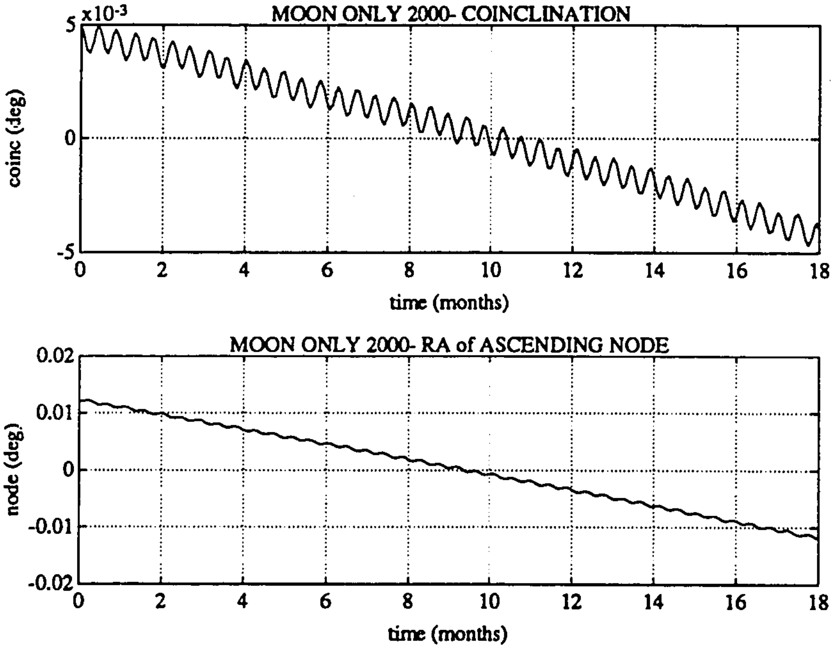

Figure 2.13 Lunar Orbit Perturbations Launch in 2000.

Secular drift plus twice monthly variation in coinclination and ascending node.

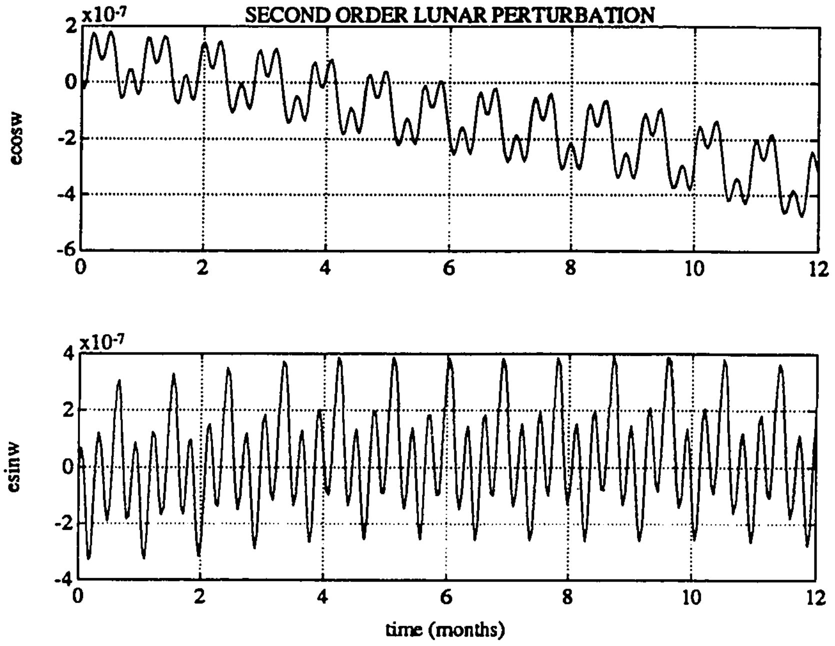

Figure 2.14 Eccentricity Vector Variations Caused by Second Order Lunar Potential.

2.5.3 Solid Earth Tides

The Sun and Moon exert forces on the Earth which cause variations in its shape. These bulges in turn have a noticeable effect on the orbit of a near Earth satellite. A simple model of this perturbation is often used in which the gravity gradient potential of the Sun or Moon is evaluated at the surface of the Earth and multiplied by the Love number, k_2, and a reduction factor of $\left(\frac{R_E}{r}\right)^3$ [*NASA, 1988, p. 152*].

This formulation was used in the long term simulations for both the Sun and Moon, assuming an elastic response time of zero and a typical Love number $k_2 = 0.3$ [*NASA, 1988, p. 155*]. These secondary effects of the Sun and Moon were found to be less than one fifth of the direct influence. Thus, the simple model seems adequate at this stage of the analysis.

2.6 Precession of the Equinoxes

Precession of the equinoxes refers to the movement of the Earth's spin axis in a 23.5 deg cone about the ecliptic pole. This motion, which is due primarily to the torque exerted by the Sun on the Earth's equatorial bulge, has a period of 25,700 years. As the Earth moves out from under the spacecraft orbit it produces an effective change in the inclination of the orbit.

The reference point from where the right ascensions of both the guide star and the ascending node of the orbit are normally measured, also shifts as a result of the precession of the equinoxes. However, because we are only interested in the relative position of the node relative to Rigel, this shift has no effect on Ω.

The annual general precession is westward at the rate

$$\dot{\psi}_{prec} = \frac{2\,\pi}{25700\,yr} = 0.000244\,rad/yr = 0.0139\,deg/yr \tag{2.48}$$

which produces a change in the coinclination of a polar orbit aligned with Rigel of

$$\begin{aligned} \frac{d\,i'_{prec}}{d\,t} &= sin\,(tilt_E)\,sin\,(\,\lambda_R)\,\dot{\psi}_{prec} \\ &= sin\,(23.5\,deg)\,sin\,(78.484\,deg\,)\,(0.0139\,deg/yr) \\ &= 0.0054\,deg/yr \end{aligned} \tag{2.49}$$

2.7 Drag Models

Two drag models are needed for GP-B. The first is applicable to the orbit injection and trim phase of the mission and the second represents the environment during the science data collection. During orbit trim the spacecraft experiences drag forces typical of any vehicle in a polar orbit at a 650 km orbit. However, once the experiment starts a drag compensation system is employed to ensure that the spacecraft follows a purely gravitational orbit. Thus, to model the *long term* spacecraft motions, we should only consider the *residual* drag effects.

2.7.1 Orbit Injection Drag Model

Drag effects during the orbit trim are modeled as a dissipative force directed opposite to the velocity of the vehicle [*Yekutiel, 1989*]. The specific force due to drag is assumed to be the sum of a steady term, (d_0), whose parameters depend on the solar cycle and a random term, (d_r), with time constant $\beta = 10$ s, and steady state variance $\alpha = (0.1\ d_0)^2$, as shown below [*Yekutiel, 1989*].

$$\begin{aligned} \mathbf{a}_{drag} &= -\,(d_0 + d_r)\,\mathbf{i}_v \\ d_0 &= \frac{1}{2}\frac{\rho A}{m} C_D\, v^2 \\ \dot{d}_r &= -\beta\, d_r + w_r\,, \qquad w_r \sim N(0, 0.1\, d_0\sqrt{2\beta}) \end{aligned} \tag{2.50}$$

A, m, C_D , and v are the spacecraft cross sectional area, mass, drag coefficient and velocity. ρ is the average atmospheric density and $\mathbf{i}_v$ is a unit vector in the direction of the spacecraft velocity. The approximate value of d_0 for the GP-B spacecraft during a year with average solar activity, is 1.5×10^{-7} m/s^2.

2.7.2 Long Term Drag Model

The drag compensation system flown on Triad in 1976, successfully reduced the accelerations of the proof-mass, and hence the orbit, down to the level of 5×10^{-12} g's [*DeBra, 1973*]. The logic of the GP-B system will be quite similar to the earlier one; however, proportional helium thrusters rather than cold gas will be used for actuation. In the GP-B system it is expected that the spacecraft self gravitation and charging of the proof mass will limit the performance to approximately 10^{-10} g or 10^{-9} m/s^2.

To investigate the effect on long term orbit motions, the residual disturbances are modeled as follows. The variance of the disturbing force is $\sigma_D{}^2 = (10^{-9}\ \mathrm{m/s^2})^2$. Assuming that the disturbance can be described by a white noise process up to the bandwidth of the drag free translational controller ($f = 0.1$ Hz), its spectral density is given by $Q = \sigma_D{}^2/2f$. Taking each component of the disturbing force - radial (w_r), along track (w_θ), and out-of-plane (w_h), as independent, and substituting in Eq. 2.12 gives the following rates of change:

$$\begin{aligned}
\frac{d\, i'_D}{dt} &= -\frac{\cos u}{n\, a}\, w_h(t) \\
\frac{d\,\Omega_D}{dt} &= \frac{\sin u}{n\, a}\, w_h(t) \\
\frac{d\, a_D}{dt} &= -\frac{2}{n}\, w_\theta(t) \\
\frac{d\,\xi_D}{dt} &= \frac{1}{n\, a}\{ \sin u\; w_r(t) + 2 \cos u\; w_\theta(t)\} \\
\frac{d\,\eta_D}{dt} &= \frac{1}{n\, a}\{ \cos u\; w_r(t) + 2 \sin u\; w_\theta(t)\}
\end{aligned} \tag{2.51}$$

To first order, the variance of each of the elements due to the random drag disturbance is given by,

$$\begin{aligned}
E\left[i'_D(t)^2\right] &= \frac{\sigma_D^2/a^2}{4 f n^2}\, t & \qquad E\left[\Omega_D(t)^2\right] &= \frac{\sigma_D^2/a^2}{4 f n^2}\, t \\
E\left[\xi_D(t)^2\right] &= \frac{5\,\sigma_D^2/a^2}{4 f n^2}\, t & \qquad E\left[\eta_D(t)^2\right] &= \frac{5\,\sigma_D^2/a^2}{4 f n^2}\, t \\
E\left[a_D(t)^2\right] &= \frac{4\,\sigma_D^2}{f n^2}\, t
\end{aligned} \tag{2.52}$$

At the end of the 18 month mission the standard deviations of the coinclination and node are 9 x 10^{-8}deg; the eccentricity vector components, 8 x 10^{-9}, and the semimajor axis, 0.04 m. These changes are clearly negligible in comparison to the gravitational disturbances discussed in the previous sections.

Work is currently being conducted to refine the drag-free translational control requirements based on improved gyro models [*Kasdin and Keiser, 1990*].

2.8 Short Term Orbit Motions

A computer simulation was developed to model the short term orbit dynamics during the orbit adjustment phase of the GP-B mission. This program was then used to investigate the performance of the closed loop control system. The spacecraft orbit is propagated using the instantaneous orbit elements in the variational equations given in Eq 2.12. Perturbing forces due to Earth harmonics up to degree and order 4 are included, as well as the uncompensated drag model given by Eq. 2.50. A fourth order Runga-Kutta integration procedure with a time step of 10 sec is implemented. This program is used to simulate time periods of 15 days or less.

Figure 2.15 shows the motion of the instantaneous eccentricity vector over a three day period. Figure 2.16 illustrates the evolution of the instantaneous coinclination and node over the same interval. The initial conditions were set so that the coinclination and node are as close to zero as possible and the eccentricity is centered on the frozen value for only the J_3 odd harmonic, of (0, 0.00106). For simplicity in the simulation, this value was used rather than (0, 0.00134) which is the frozen value when all odd harmonics up to J_{35} are considered. This simplification does not alter the nature of the results. These results will be discussed further in Chapters 3 and 4.

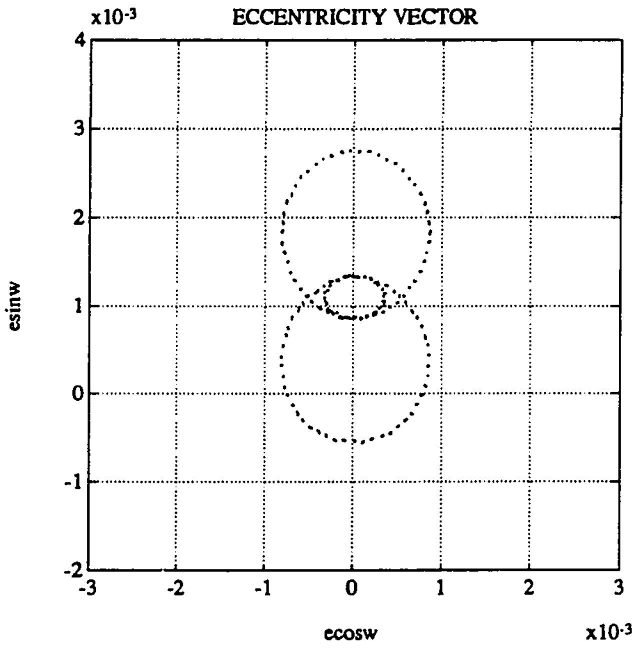

Figure 2.15 Short Term Eccentricity Vector Motion.

Results of short term dynamic simulation. Includes drag model and Earth harmonics (l,m) ={(2,0) (2,1) (2,2) (3,0) (3,1) (3,2) (3,3) (4,0) (4,1) (4,2) (4,3) (4,4)) }. Shows snapshots of the instantaneous eccentricity vector at 5 minute intervals over a three day period.

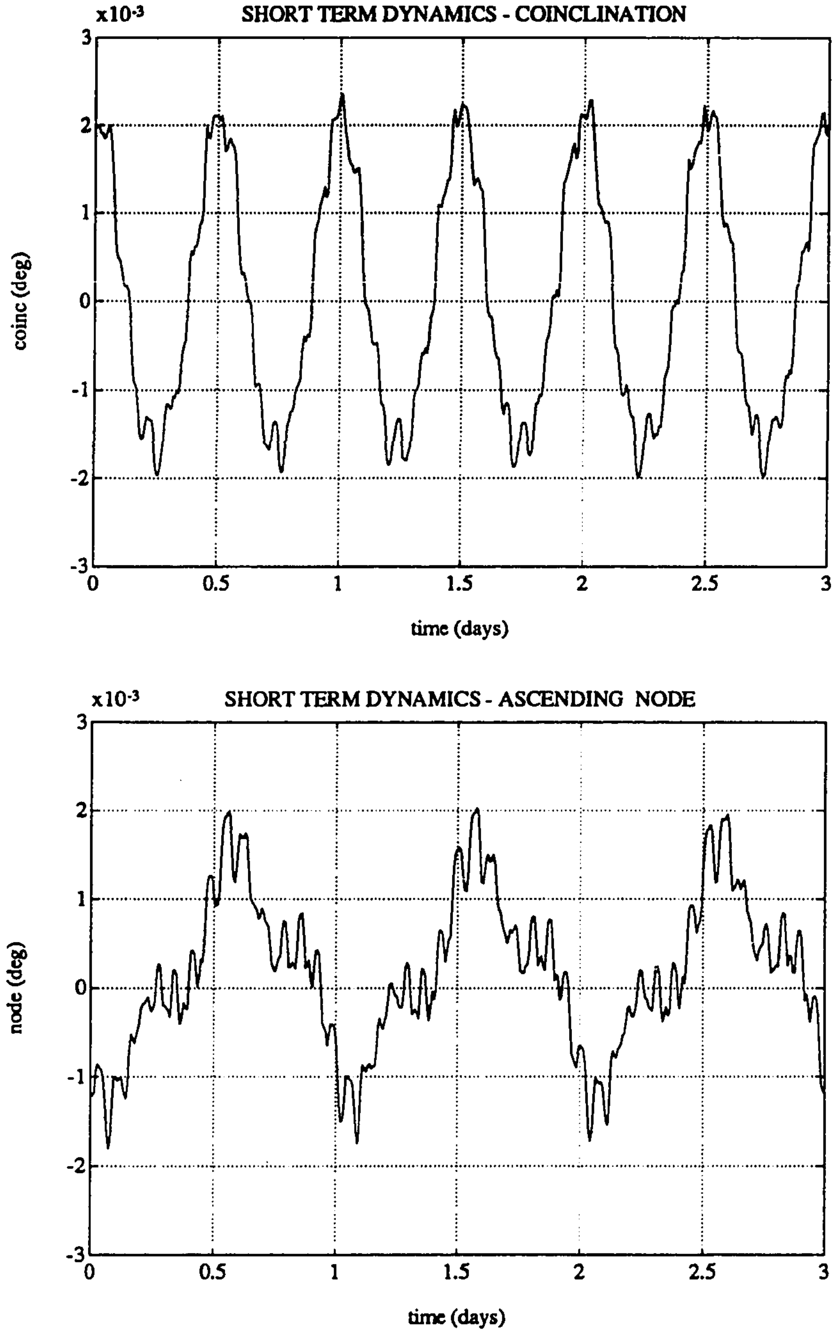

Figure 2.16 Short Term Out-of-plane Dynamics.

Results of short term dynamic simulation. Includes drag model and Earth harmonics (l,m) ={(2,0) (2,1) (2,2) (3,0) (3,1) (3,2) (3,3) (4,0) (4,1) (4,2) (4,3) (4,4)) }. Shows time history of the instantaneous coinclination and node over a 3 day period.

2.9 Long Term Orbit Motions

Simulation results for the *long term* motions of the spacecraft due to the combined perturbations described in Sections 2.4-2.7 will now be presented. By long term we refer to effects which are secular or have periods of more than ten days The short term motions described in the previous section were not modeled in the long term simulation, but can be superimposed onto the long term results. The expressions for the *orbit averaged* rates of change of the orbit elements were programmed and integrated numerically. Table 2.9 lists the perturbations which were considered in the previous sections, and identifies which ones were modeled in the long term simulation.

The target injection orbit was selected so as to minimize the separation between the orbit plane and the direction to Rigel, and to reduce the mean eccentricity. The following sections show the orbit evolution and compare the resulting variations in the elements to the requirements described in Section 2.2. The effects of orbit injection errors are also considered. Because of the very low eccentricity of the nominal GP-B orbit and the elimination of surface forces by the translational control system, there is no significant coupling between the in-plane and out-of-plane orbit dynamics.

2.9.1 Out-of-plane Simulation Results

The main contributors to the long term motion of the orbit plane are J_2, solar and lunar gravity gradient and tidal effects, and the precession of the Earth's pole. In the simulation, the nodal drift due to J_2 is modeled according to Eq. 2.19. The expressions in Eq. 2.43 for the Sun and Moon effects are used, with the motions of the Sun and Moon modeled based on almanac data [*Naval Observatory, 1985*]. The tides and precession effects are programmed as described in Sections 2.5.3 and 2.6. The orbit average coinclination and node drift rates are integrated numerically over the mission.

Table 2.9 Summary of Long Term Simulation Models.
A '' indicates that the effect is negligible and was not modeled in the simulation.*

	Long Term Simulation Models	
Effects	**Out-of-plane**	**In-Plane**
Earth Oblateness J_2	Nodal drift proportional to coinclination.	Rotation of the eccentricity vector.
Low Order Tesserals	*	*
Odd Harmonics	*	Offset of the frozen eccentricity vector.
Near Resonant Terms	*	*
Sun Gravity Gradient	Secular and twice yearly coinc and node drifts.	*
Moon Gravity Gradient	Secular & twice monthly coinc and node drifts.	*
Second Order Lunar	*	*
Solid Earth Tides	Secular & twice periodic coinc and node drifts.	*
Precession of the Equinoxes	Constant coinc drift.	*
Residual Random Drag	*	*

Simulations were run for 18 month missions beginning on March 21 for the years 1997 and 2000. Table 2.10 summarizes the results by giving the target coinclination and node, and the resulting deviations from the nominal orbit. Both the mean and peak values of the coinclination and node are given. The target conditions were selected to minimize the variation in the node over the 18 month mission, because this has the most significant influence in reducing the Newtonian drifts described in Section 2.2.2.

Table 2.10 Target Values of i' and Ω for Orbit Injection.
Initial values and 18 month mean and maximum deviations from the nominal.

Start Date	target i'_0 (deg)	mean i' (deg)	maximum $\lvert i' \rvert$ (deg)	target Ω_0 (deg)	mean Ω (deg)	maximum $\lvert \Omega \rvert$ (deg)
Mar. 21, 1997	0.00375	-0.0005	0.0057	-0.0128	-0.0008	0.0187
Mar. 21, 2000	0.00640	-0.0004	0.0071	0.0260	-0.0011	0.0261

The maximum node deviation for the 1997 start date is less than 0.02 deg, and for the year 2000 it is less than 0.03 deg. Figure 2.17 illustrates the Newtonian gyro drifts due to the suspension forces for the nominal 1997 and 2000 simulations as modeled by Eq. 2.6. In both cases the maximum drift is less than the desired 0.1 marcsec/yr error margin (for at least a 12 month mission).

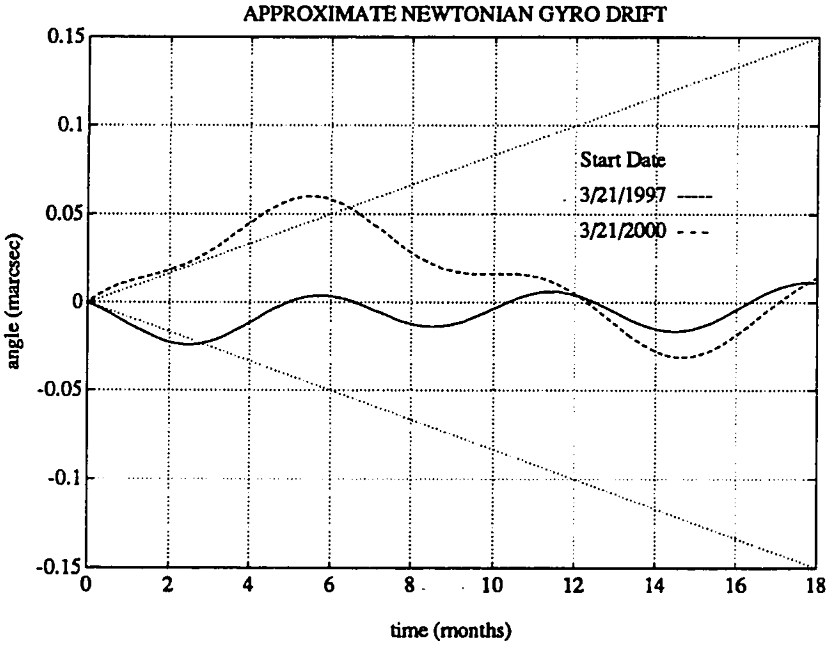

Figure 2.17 Newtonian Gyro Drifts for Nominal Orbit Injection.

The solid line shows the drift for nominal conditions in 1997 and the dashed line shows nominal results for the year 2000. The dotted lines indicate the desired drift boundaries of ±0.1 marcsec/yr.

In order to specify the performance required from the orbit trim system, we must evaluate the effect of orbit injection errors on the long term orbit motion and on the expected gyro drift. Errors in the initial location of the ascending node translate directly into a mean and maximum node error, and have relatively little effect on the coinclination. An initial error of 0.01 deg in the node produces an additional gyro drift of about 0.04 marcsec after 6 months, 0.09 marsec after 1 year, and 0.13 marsec after 1.5 yrs. Thus, one can judge from Figure 2.17 that such an error in the node injection can be tolerated in both 1997 and 2000, since the gyro drift remains within 0.1 marcsec for the first twelve months, and within 0.15 marcsec during the full 18 month mission.

Inclination errors have a more subtle effect, due to the J_2 induced drift rate which is proportional to the coinclination. Table 2.11 summarizes the simulation results for initial *coinclination* errors of $\pm 10^{-3}$ deg and $\pm 2 \times 10^{-4}$ deg for each of the launch dates. The evolution of the coinclination and node are plotted in Figures 2.18 and 2.19. for the target conditions and these initial injection errors.

Table 2.11 Mean and Maximum i' and Ω Due to Inclination Orbit Injection Errors. *Inclination errors of ± 0.001 and ± 0.0002 for Mar. 1997 and 2000 start dates.*

Start Date	error $\Delta i'_0$ (deg)	mean i' (deg)	maximum $\lvert i' \rvert$ (deg)	mean Ω (deg)	maximum $\lvert \Omega \rvert$ (deg)
Mar. 21, 1997	-0.0002	-0.0006	0.0059	+0.0076	0.0308
	+0.0002	-0.0002	0.0055	-0.0060	0.0263
	-0.0010	-0.0014	0.0067	+0.0348	0.0794
	+0.0010	+0.0006	0.0057	-0.0332	0.0711
Mar. 21, 2000	-0.0002	-0.0006	0.0073	+0.0079	0.0381
	+0.0002	-0.0002	0.0069	-0.0056	0.0359
	-0.0010	-0.0014	0.0081	+0.0350	0.0884
	+0.0010	+0.0006	0.0074	-0.0327	0.0751

In the coinclination plots one can identify the twice yearly variation due to the solar effect as well as the small twice monthly oscillations caused by the Moon. Notice that in 1997 there is almost no secular drift in the coinclination. In this year the sum of the drift rates produced by the Sun, Moon, J_2, and the precession of the equinoxes is almost zero; whereas in the year 2000 there is a net secular drift of about -4×10^{-3} deg/yr in the coinclination. This produces a larger deviation in the node for this year compared to 1997, and causes greater drifts when orbit injection errors occur.

Figures 2.20 and 2.21 show the Newtonian gyro drifts corresponding to the simulations with inclination injection errors for the 1997 and 2000 start dates, respectively. In both cases, injection errors of ± 0.001 deg (125 m) cause drifts of more than 0.4 marcsec after 18 months. Errors of ± 0.0002 deg (25 m) produce acceptably small gyro drifts, within 0.1 marcsec over the 18 months for the 1997 launch and slightly greater in the year 2000. Clearly this imposes a much tighter injection requirement than the node error. If we allow for a ± 0.0002 deg inclination error, a 0.002 deg node error is still permissible. These results should only be used as a guideline in determining the orbit injection requirements because of the great uncertainty in the actual values of the gyro coefficients and their variability.

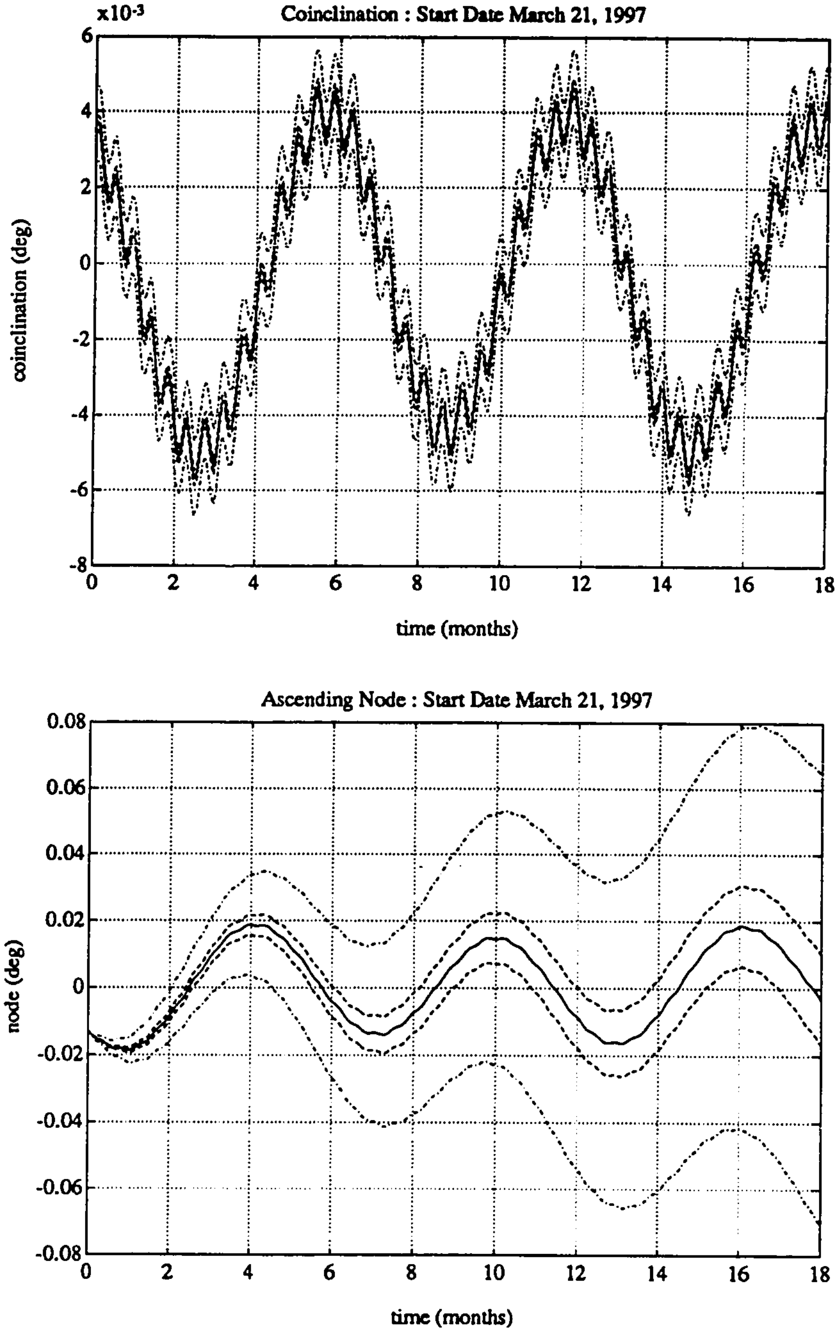

Figure 2.18 Long Term Motion of the Coinclination and Node - March 21, 1997.
Solid line shows target orbit evolution. Dashed lines show results for initial coinclination errors of $\pm 2x10^{-4}$ *deg. Dash-Dot lines show results for initial coinclination errors of* $\pm 10^{-3}$ *deg.*

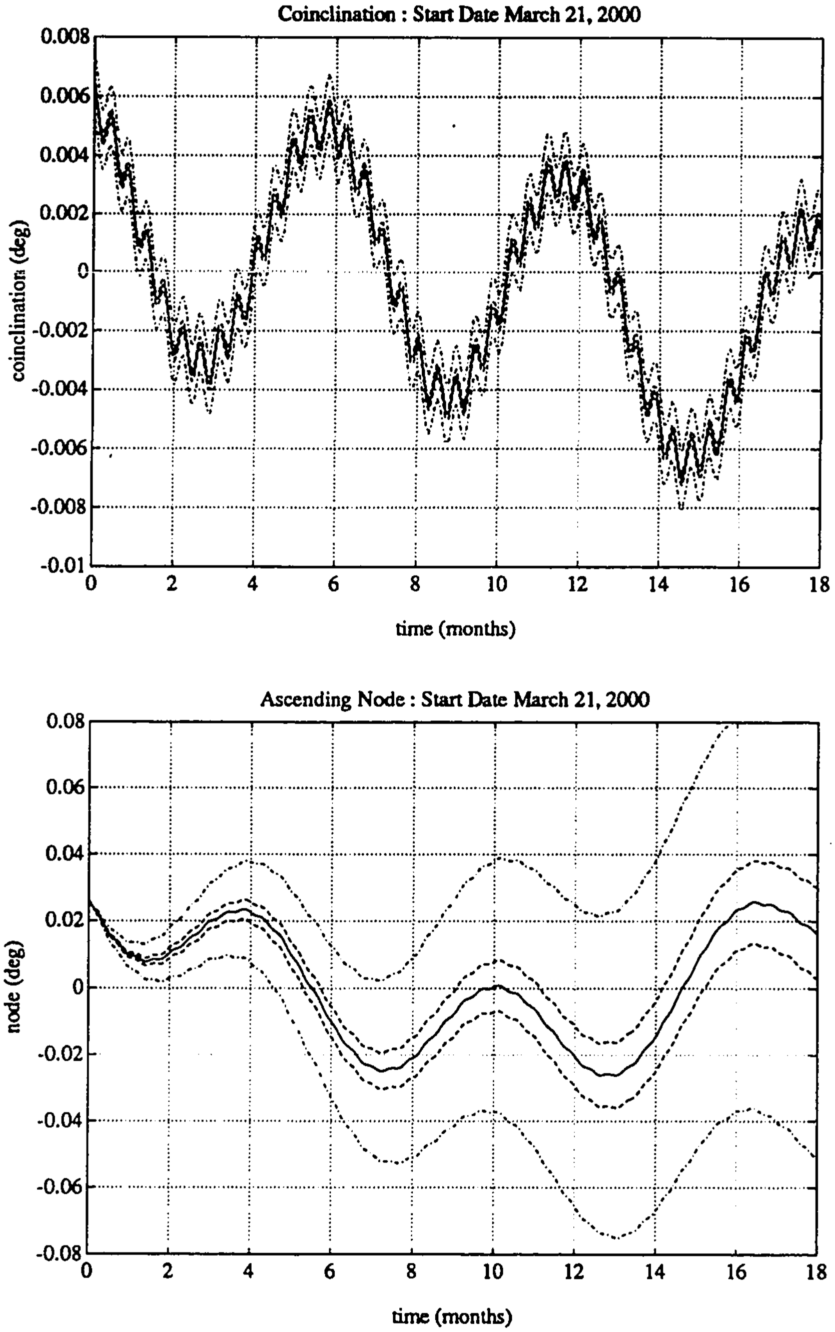

Figure 2.19 Long Term Motion of the Coinclination and Node - March 21, 2000.

Solid line shows target orbit evolution. Dashed lines show results for initial coinclination errors of $\pm 2 \times 10^{-4}$ *deg. Dash-Dot lines show results for initial coinclination errors of* $\pm 10^{-3}$ *deg.*

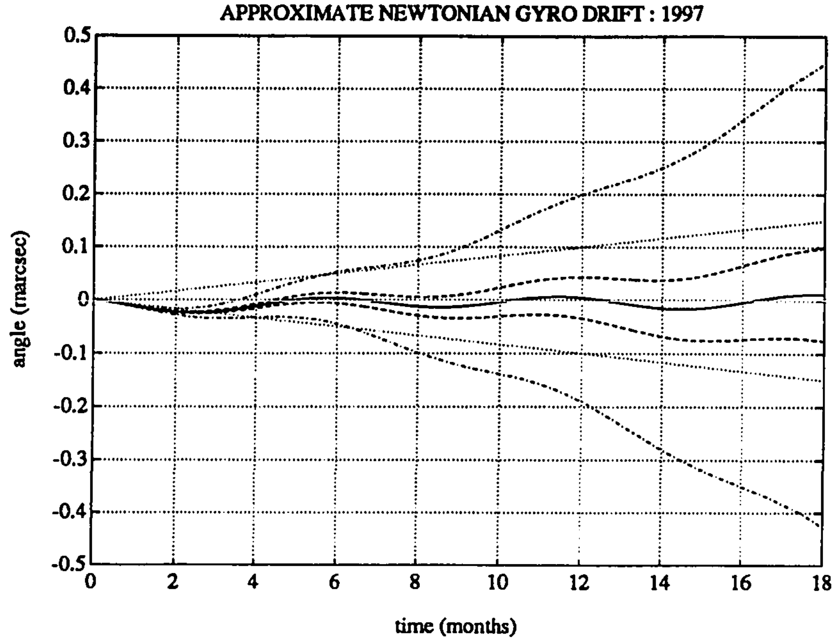

Figure 2.20 Newtonian Gyro Drift - March 21, 1997.

Solid line shows target injection. Dashed lines show inclination injection errors of $\pm 2 \times 10^{-4}$ *deg. Dash-Dot lines show inclination injection errors of* $\pm 10^{-3}$ *deg. Dotted lines indicate* ± 0.1 *marsec/yr bounds.*

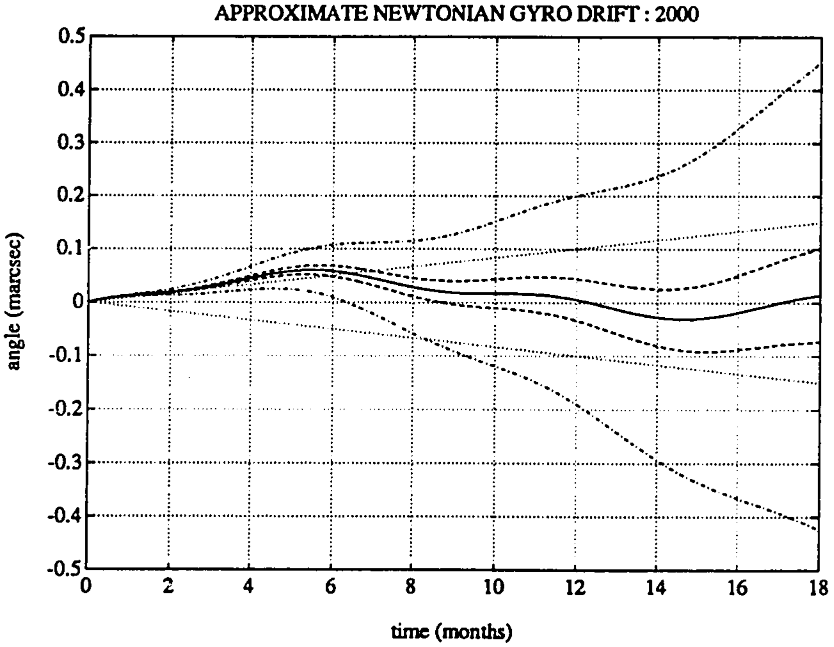

Figure 2.21 Newtonian Gyro Drift - March 21, 2000.

Solid line shows target injection., Dashed lines show inclination injection errors of $\pm 2x10^{-4}$ *deg. Dash-Dot lines show inclination injection errors of =* $\pm 10^{-3}$ *deg. Dotted lines indicate* ± 0.1 *marsec/yr bounds.*

2.9.2 In-Plane Simulation Results

Long term motion within the orbit plane is governed primarily by the Earth oblateness and the odd zonal terms. The near resonant tesseral Earth harmonics and the second order lunar effects were found to cause only neglibly small variations. As mentioned in Section 2.2.6, the J_2 term causes the eccentricity vector to rotate in the plane with a period of about 101 days. The constant rate in the east component of the eccentricity produced by the odd zonals changes the center of this rotation from $\xi=0$, $\eta=0$ to $\xi=0$, $\eta=0.00134$. This value of eccentricity, $e=0.00134$, with perigee directed toward the north, is stable for a 650 km polar orbit. For this reason it is known as the frozen eccentricity [*Small, 1986*]. The average eccentricity for GP-B will be minimized by targeting this stable value. Any other starting values of ξ and η will eventually cycle to larger values. Figure 2.22 shows the trajectory of the eccentricity vector for initial conditions near the frozen value. To ensure that the orbit averaged eccentricity always remains less than 0.002, the initial vector distance from $(\xi_o,\eta_{\cdot 0})$ to (0,0.00134) must be less than 0.0006.

2.10 Orbit Modeling and Requirements Summary

In this chapter the orbit of the GP-B spacecraft has been modeled considering the perturbing effects of the the noncentral Earth gravity, the Sun and Moon, residual drag, and the precession of the the Earth's pole. Short term variations in the instantaneous elements during orbit injection were investigated via computer simulation. The short term dynamic model will be used in Chapters 3-4 to evaluate the performance of the navigation and orbit trim systems.

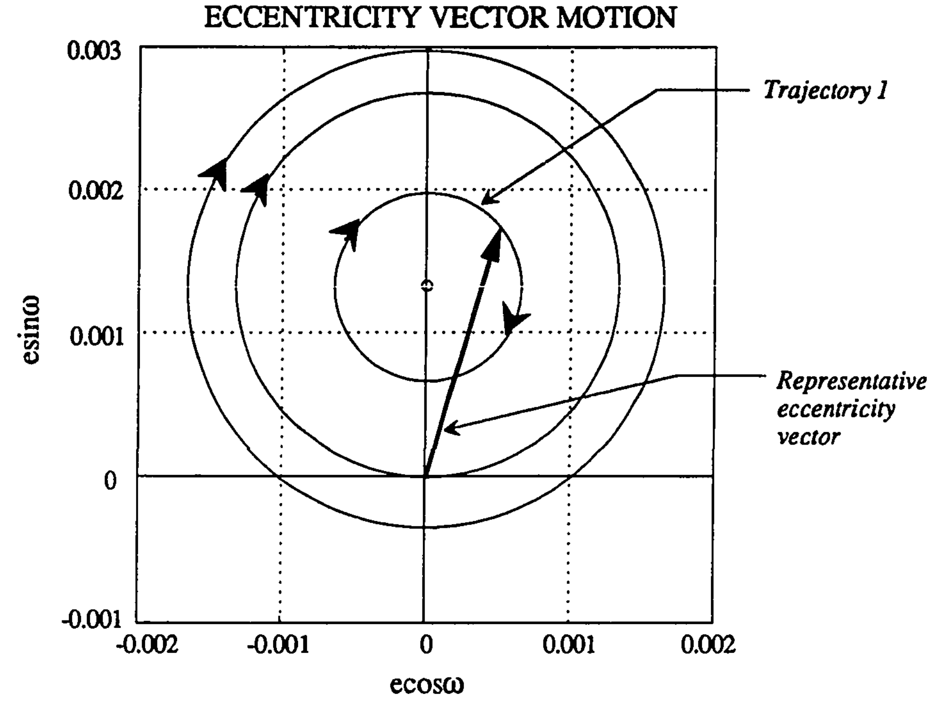

Figure 2.22 Long Term Motion of the Orbit Average Eccentricity Vector.
Evolution of the eccentricity vector is shown for four sets of initial conditions. The innermost trajectory is very close to the frozen eccentricity vector of (0.0, 0.00134). Trajectory 1 shows the boundary for the acceptable eccentricity vector errors. Note that if the initial eccentricity is zero it will grow to exceed the permissible value.

Long term orbit averaged motions were simulated in order to define a target injection orbit and to review restrictions on how accurately it must be achieved. The target values of the most critical elements- coinclination and ascending node- depend on the experiment start date. Table 2.12 summarizes the results of this long term study. The *nominal* mission-average values of the orbit elements, the target injection values for candidate start dates in March, 1997 and March, 2000, and acceptable injection errors are given. Out-of-plane requirements are highlighted to emphasize their greater importance. If these conditions are met, the Newtonian drift of the gyro will be less than about 0.1 marcsec and the orbit altitude will not vary by more than 15 km.

The target injection values determined here are ***averaged*** elements which define the launch vehicle guidance objective. Short term variations described in Section 2.8 should be superimposed onto the average target values depending on the longitude of the satellite subpoint to determine instantaneous target element values. It is unlikely that the upper stage of any booster will be able to meet the stringent requirements specified above; thus there is a critical need for a precise orbit trim system onboard the GP-B spacecraft. In the next section we turn to the task of determining the orbit onboard the spacecraft.

Table 2.12 GP-B Orbit Requirements Summary.

Elements	Nominal Value	Target Injection Value 1997	Injection Error Magnitude 1997	Target Injection Value 2000	Injection Error Magnitude 2000
a *(km)*	7028.14	7028.14	≤ 5.00	7028.14	≤ 5.00
ξ	0.0000	0.0000	≤ 0.0005	0.0000	≤ 0.0005
η	0.0000	0.0013	≤ 0.0005	0.0013	≤ 0.0005
i' ***(deg)***	**0.0000**	**0.00375**	**≤ 0.0002** (≤ 25 m)	**0.00640**	**≤ 0.0002** (≤ 25 m)
Ω ***(deg)*** *(from Rigel)*	**0.0000**	**-0.0128**	**≤ 0.002** (≤ 250 m)	**0.0260**	**≤ 0.002** (≤ 250 m)

CHAPTER 3. NAVIGATION

3.1. Introduction

The key element in the closed loop orbit trim system is the *direct* availability of navigation data onboard the spacecraft via the Global Positioning System (GPS). The primary purpose of the navigation system considered here is to collect information from the GPS satellites and provide estimates of the orbit to the control system. In addition it must give an orbit fix to the Delta II upper stage, assign time tags and orbit estimates to the collected science data, and transmit raw GPS measurements to the ground for processing of the geodesy data.

The navigation system consists of a set of GPS antennas, a receiver, and a navigation processor. The navigation processor propagates the orbit estimates in two parts- the reference position and velocity state, and the deviation from this reference. An extended Kalman filter is used to incorporate new measurements from GPS and improve the orbit estimate.

The next section of this chapter outlines the navigation requirements for each of the phases of the GP-B mission. Following that is a discussion of the different coordinate frames used in defining and determining the GP-B orbit. GPS and its uses on the GP-B spacecraft are introduced. Then, the navigation processor algorithm is described in detail and computer simulation results are presented which give an indication of the system performance.

3.2 Navigation Requirements

For the closed loop orbit trim system to operate properly, the mean errors in the estimates of the elements, over an orbit, should be about a factor of 10 smaller than the required injection accuracies. Based on the orbit modeling results, the mean coinclination and node estimate errors should thus be less than 2×10^{-5} deg and 3×10^{-4} deg, respectively, the eccentricity vector component errors 5×10^{-5}, and the semimajor axis errors approximately 500 m. In terms of position and velocity requirements this translates to about 25 m and 0.025 m/s. The standard deviation of the estimate errors should be somewhat smaller than the required injection accuracies, perhaps by a factor of two. These numbers serve only as guidelines. The test of the navigation performance is how well a simulation of the closed loop system performs using the estimates provided.

During the science data collection, navigation information is required to time tag the measurements and to compute the orbital aberration. The aberration is known to be proportional to the velocity of the spacecraft perpendicular to the line of sight to the star. The current data reduction scheme assumes knowledge of this velocity to an accuracy of about 0.01 m/s, 1-σ [*Qin, 1989*]. In addition, position and velocity information may be required by the onboard roll control and pointing systems; however, these requirements have not yet been evaluated.

The most stringent requirements on the navigation system are imposed by the geodesy coexperiment. The intensive data postprocessing needed to improve the model of the Earth's gravitational field requires measurements of GPS carrier phase on both L1 and L2, to a minimum of 6 satellites. The preferred data rate is 0.1 Hz with measurement precision of under one centimeter [*Tapley, et al.* 1990]. This imposes severe requirements on the GPS receiver and antennas as will be discussed in the following section. The data transmission rate needed to forward the raw GPS measurements to the ground has been estimated to be on the order of 150 bps out of a total telemetry stream of 2500 bps.

3.3 Coordinate Systems

Three fundamental coordinate frames come into play in the GP-B navigation system. An Earth centered inertial (ECI) frame is used to define the target and actual spacecraft orbit; the GPS system provides satellite ephemeris information in an Earth centered Earth fixed coordinate frame known as WGS-84; and finally a locally level frame attached to the orbiting spacecraft, or Hill frame, is used by the navigation filter and controller algorithms. The Hill frame is defined by the navigation processor internally based on the computed reference orbit as will be described in Section 3.5.1.

The ability to transform positons and velocities between the ECI and WGS-84 frames must reside either in the GPS receiver software or an external navigation processor. This transformation must account not only for the rotation rate of the Earth, but also its precession, nutation, and wobble. The algorithm for converting ECI estimates to WGS-84 already exists as part of the GPS control segment process for generating the satellite ephemerides. The details of this transformation have not been included in this study, but should be addressed in the near future.

3.4 Global Positioning System

GPS is a passive satellite based navigation system consisting of a constellation of 24 satellites at an altitude of about 20,000 km. Figure 3.1 indicates the planned spacing of the satellites within each of the six orbit planes [*Green, et al., 1989*]. To navigate with GPS a user must be equipped with an antenna, a receiver, and a measurement processor capable of interpreting the GPS observables. The user determines the range to each of four or more satellites in view based on the transit time of the GPS signal. Position and velocity are computed using this ranging data plus satellite ephemeris information also provided on the ranging signal. The following sections describe the GPS measurements and each of the hardware components needed onboard the GP-B spacecraft.

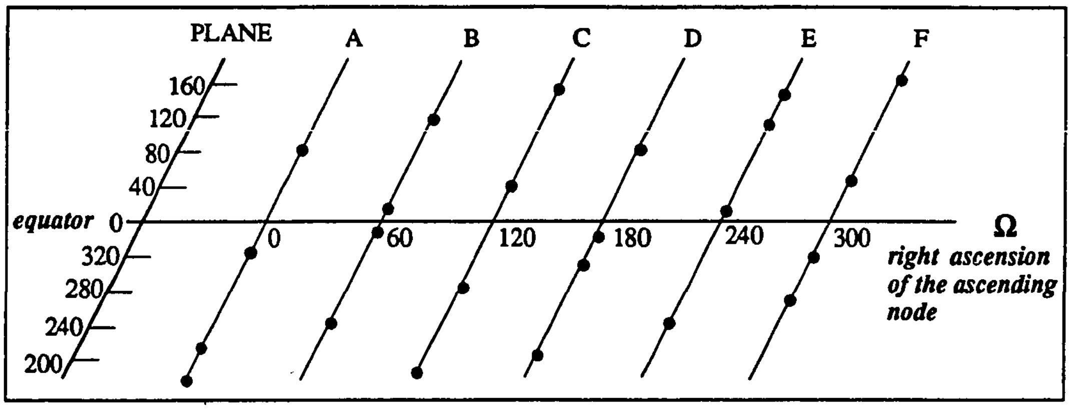

Figure 3.1 GPS 24 Satellite Constellation.

Known as the 21 Primary (+ 3 active spares) Satellite Constellation. Inclination of 55 deg, semimajor axis of 26609 km, orbit plane node and satellite phase are shown.[Green, et al., 1989]

3.4.1 GPS Signal

The complex signals broadcast by the GPS satellites have been designed to meet the following requirements listed in Table 3.1 [*Wells, 1987*]. Each GPS satellite transmits two L-Band carrier signals at 1575.42 MHz (L1) and 1227.60 MHz (L2). Both carriers are phase shift key modulated by a pseudo random noise (PRN) code with a chip rate of 10.23 MHz, known as the precise code (P code). The entire P code is 37 weeks long with each satellite assigned a unique one week segment of the code. In addition, each satellite also has its own 1.023 MHz PRN sequence known as the C/A code which modulates the L1 carrier in quadrature with the P code. The C/A code is easier to acquire than the P code because of its shorter length of 1 msec and higher power. A 50 Hz navigation message is also broadcast on both the L1 and L2 carriers. This data allows the user to determine the position and velocity of the GPS satellites in the WGS-84 coordinate system and to model the satellite clock errors and ionospheric delays. Figure 3.2 illustrates the how the GPS signal components are combined [*Langley, 1990*].

Table 3.1 GPS Signal Requirements [*Wells, 1987*].

Requirement	Solution
• Unlimited users	- passive ranging
• Simultaneous ranging from many satellites	- unique identifying codes
• Unambiguous ranging	- PRN code modulation
• Real time position & velocity determination	- satellite ephemeris broadcast
• High accuracy velocity	- microwave carrier frequency
• High accuracy position	- high frequency code modulation dual frequency ionospheric correction
• Good interference rejection	- direct spread spectrum, PRN codes
• Military security	- classified Y-code selective availability

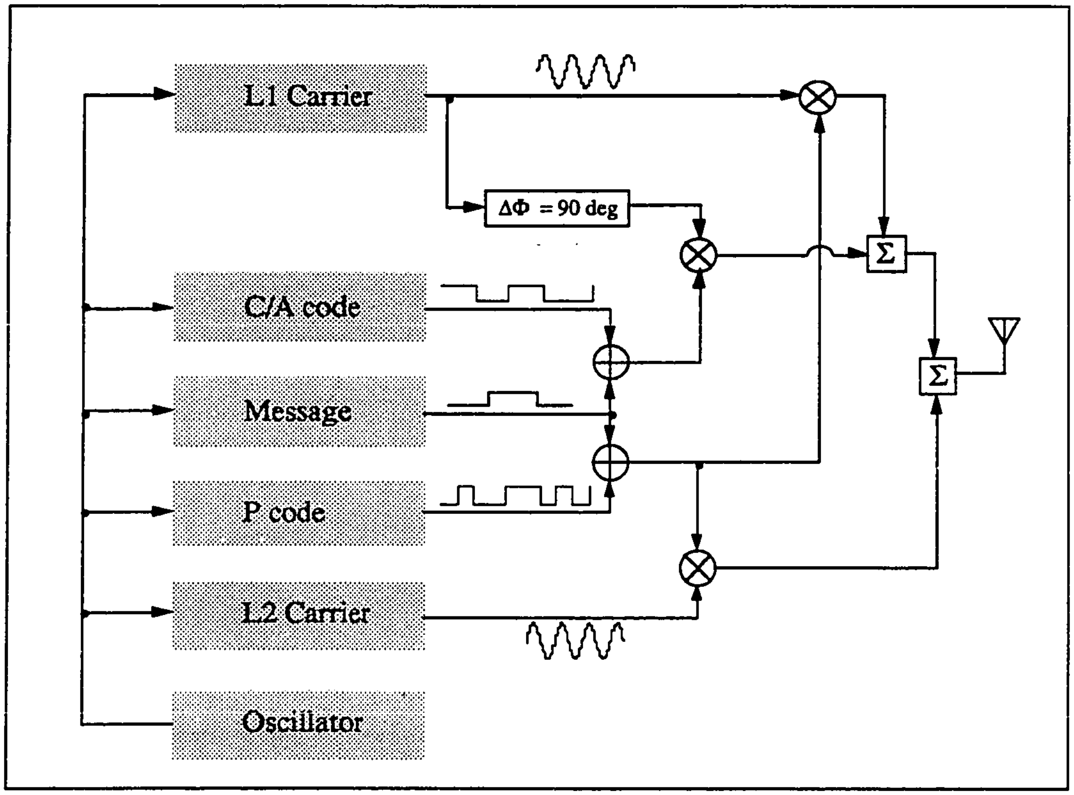

Figure 3.2 GPS Signal Components [*Langley, 1990*].

Waveforms are for illustration and are not to scale.

Navigation performance for users of the P code is generally better than C/A code because finer resolution can be achieved with a higher frequency signal and access to the code on both carrier frequencies. However, most civilian GPS receivers track only the C/A code, because the Air Force has reserved the right to substitute a classified code known as the Y code for the unclassified P code, without prior warning. Only military users would have access to this code, and, if it is turned on, unauthorized P code receivers would not be able to acquire any satellites. An additional security device, known as selective availability (SA) will intentionally degrade GPS performance for most civilian users. This will be discussed further in Section 3.3.4.

3.4.2 Antennas

Modern GPS antennas, known as microstrip elements, are compact, simple in construction, reliable, and have gain patterns which are highly resistant to indirect signal interference, known as multipath. The antenna consists of the sensing element and preamplifier. The phase center, or apparent signal reception point, depends upon the observation angle. The motion of the antenna phase center does not significantly influence navigation performance; however, to achieve the centimeter level measurement precision required by the geodesy coexperiment, it must be stable and calibrated to about 0.1 cm.

Figure 3.3 illustrates potential locations of the GPS antennas on the GP-B spacecraft. Since the overall design has not been finalized, they may still be moved around substantially. There will probably be a total of 4 antennas to provide a continuous view of all satellites within 90 deg of the spacecraft zenith. Several of the antennas may be located on the solar panels for improved viewing and at least one should be mounted on the spacecraft body in case of panel warping or vibration. Signal blockage or reflection from vehicle surfaces, communication signal interference, and thruster plume impingement on the antenna elements must be studied in detail once a preliminary layout has been completed. An additional consideration is the viewing geometry while the spacecraft is attached to the second stage of the Delta II. At least one antenna must have a clear view of the sky to permit satellites to be acquired, and a GPS update to be provided to the booster.

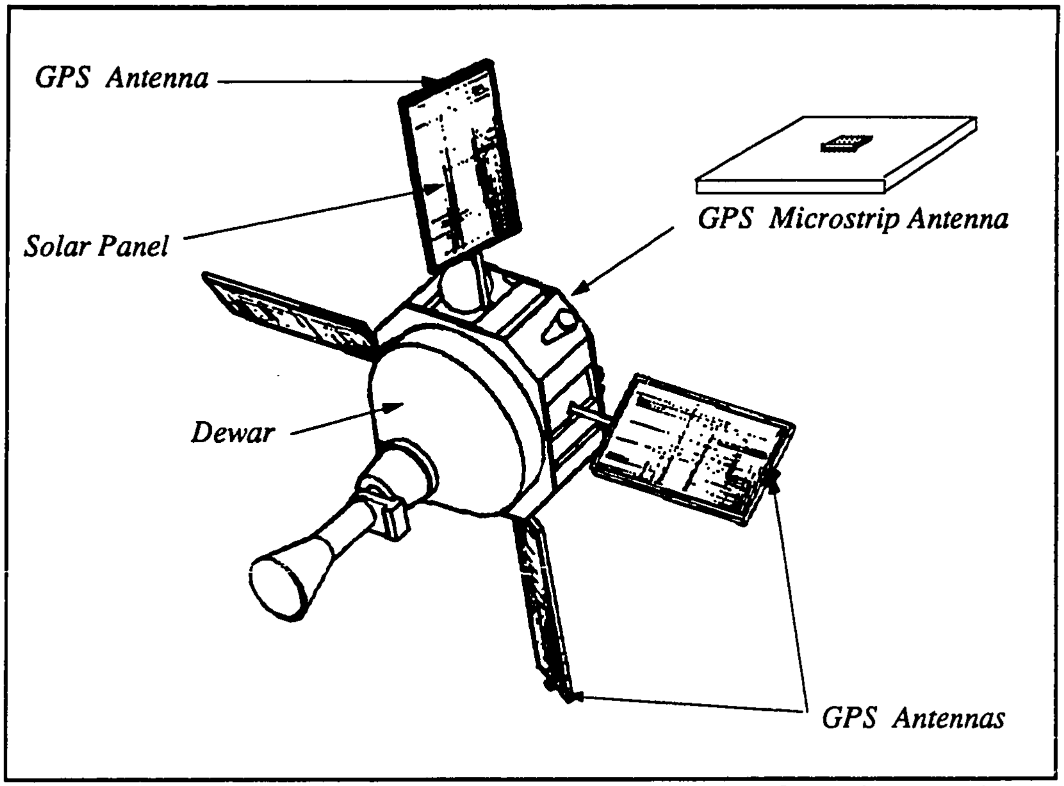

Figure 3.3 Potential GPS Antenna Locations on the GP-B Spacecraft.

3.4.3 Receiver

The design of a generic digital GPS receiver is shown in Figure 3.4. A quartz crystal oscillator with a frequency of 10.23 MHz serves as the timing reference for all signals generated in the receiver. The incoming GPS signal is downconverted to an intermediate frequency and immediately digitally sampled. Each channel consists of a code loop and a carrier tracking loop. The code loop works by correlating the incoming P or C/A code with an internally generated version of the code. The code phase can be used to find the range to the satellite modulo the chip width, which is about 30 m for P code and 300 m for C/A.

In addition to code phase measurements, modern receivers are also capable of determining the carrier phase, or accumulated carrier phase. This very precise measurement can be used to determine the change in the range or average range rate to an accuracy of about 0.01 m/s under benign dynamic conditions. This turns out to be a key feature for GPS based orbit determination.

A third type of tracking element in the receiver strips off and interprets the navigation message transmitted on both carrier signals. This provides a model of the satellite clock error, an ionospheric error model, an almanac for all satellites in the constellation, and an accurate ephemeris for the particular vehicle. The ephemeris information is used to compute the position and velocity of the GPS satellite in an Earth centered Earth fixed coordinate grid, known as WGS-84. To use GPS for determining a spacecraft orbit, a coordinate transformation must be done to convert to an Earth centered inertial reference frame as described in the previous section.

There are several tradeoffs which need to be carried out to determine what type of receiver should be flown on the GP-B spacecraft. The number of channels must be selected to permit continuous tracking of 6 to possibly 12 satellites in view. P code is desirable from the point of view of geodesy but the threat of access limitations favors C/A code. Dual frequency carrier tracking would provide additional measurements for geodesy and ionospheric corrections, but is not really required for the orbit trim or relativity mission. Access to the selective availability key may be required to achieve the necessary navigation accuracy and reliability. Table 3.2 lists the various options and their costs and benefits.

In this study we will evaluate two receiver configurations. The low accuracy, lower cost option is a standard single frequency C/A code receiver with no SA correction. The higher accuracy option is a dual frequency carrier tracking C/A code receiver with SA key access. At this time there does not appear any need for P code.

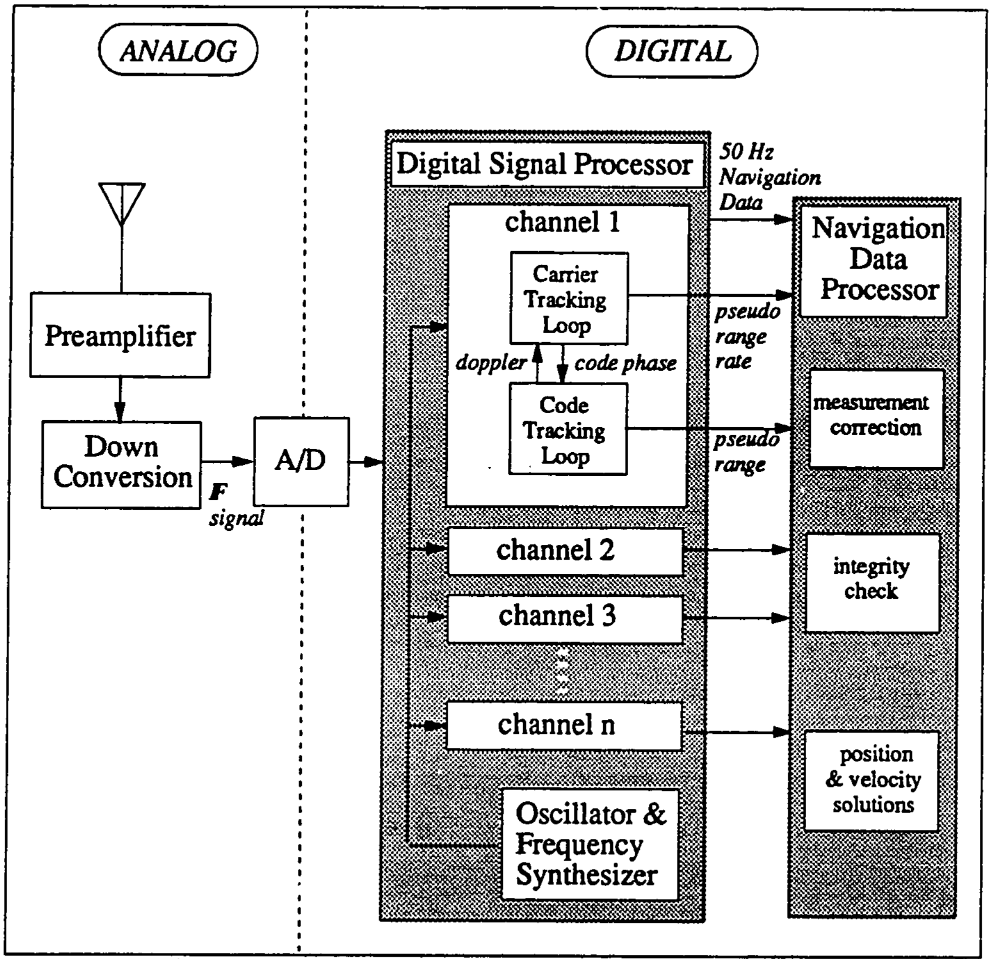
ANALOG
DIGITAL
Preamplifier
Down Conversion
F signal
A/D
Digital Signal Processor
channel 1
Carrier Tracking Loop
doppler
code phase
Code Tracking Loop
channel 2
channel 3
channel n
Oscillator & Frequency Synthesizer
50 Hz Navigation Data
pseudo range rate
pseudo range
Navigation Data Processor
measurement correction
integrity check
position & velocity solutions

Figure 3.4 Generic Digital Receiver Architecture.

Code tracking loops correlate internal code with low IF received signal. Once code lock has been achieved, time shift is used to aid carrier loop. Carrier tracking loop maintains lock on the L band carrier and provides Doppler aiding to code loop.

Table 3.2 GPS Receiver Tradeoffs

Option	Benefits	Liabilities
Dual Frequency	Improved geodesy Ionospheric corrections	More channels required for same number of satellites
C/A Code	Guaranteed access	Limited accuracy
P Code	Improved accuracy	Possible loss of access More complex / expensive
SA Key	Remove selective availability effects	Requires DoD approval, Makes receiver classified

3.4.4 Measurements

Based on the code phase delay and the accumulated carrier phase, the GPS receiver generates measurements of the range and range rate from each of the GPS satellites to the user, corrupted by the user clock error. These measurements, referred to as pseudo range (ρ) and pseudo range rate ($\dot{\rho}$), together with the GPS satellite positions ($\mathbf{r}_{GPS}$) and velocities ($\mathbf{v}_{GPS}$) are then used to compute the host vehicle position ($\mathbf{r}$), velocity ($\mathbf{v}$), clock bias (b), and drift (f).

The pseudo range and pseudo range rate measurements are modeled as follows:

$$\begin{aligned} \rho_i &= |\Delta \mathbf{r}_i| + b + \varepsilon_{\rho i} \\ &= \mathbf{e}_i^{\mathrm{T}} \mathbf{r}_{GPS\,i} - \mathbf{e}_i^{\mathrm{T}} \mathbf{r} + b + \varepsilon_{\rho i} \end{aligned} \tag{3.1}$$

$$\begin{aligned} \dot{\rho}_i &= \frac{\Delta \mathbf{r}_i^{\mathrm{T}}\, \Delta \mathbf{v}_i}{|\Delta \mathbf{r}_i|} + f + \varepsilon_{\dot{\rho} i} \\ &= \mathbf{e}_i^{\mathrm{T}} \mathbf{v}_{GPS\,i} - \mathbf{e}_i^{\mathrm{T}} \mathbf{v} + f + \varepsilon_{\dot{\rho} i} \end{aligned} \tag{3.2}$$

Where $\Delta \mathbf{r}_i = \mathbf{r}_{GPS\,i} - \mathbf{r}$, $\Delta \mathbf{v}_i = \mathbf{v}_{GPS\,i} - \mathbf{v}$, and $\mathbf{e}_i = \frac{\Delta \mathbf{r}_i}{|\Delta \mathbf{r}_i|}$ is a unit vector pointed from the user to satellite i. Random errors in the pseudo range, $\varepsilon_{\rho i}$, and pseudo range rate, $\varepsilon_{\dot{\rho} i}$, are caused by the system, the environment, or the user receiver. GPS errors are usually expressed as a distance or velocity which is computed by multiplying the time delay by the speed of light, $c = 2.997 \times 10^8$ m/s.

The measurement errors produced by the GPS itself are GPS satellite ephemeris and clock errors, and selective availability (SA). Errors in the ability of the control segment to predict the satellite ephemerides causes different range errors depending on the location of the user. These errors have been observed to be under one meter in range for the Block I satellites; however the GPS Joint Program Office (JPO) unofficial 1-σ range error is 4.3 m [*Navtech, 1987*]. The error in the GPS clock model was expected to be on the order of 3.5 m [*Navtech, 1987*], but has been observed to be below one meter as well. An optimistic, but realistic estimate of these contributions is 4.0 m 1-σ range, and 0.005 m/s 1-σ range rate.

Selective availability is an intentional degradation of the GPS signal by the DoD for security reasons. The claim is that it would limit the real time accuracy achievable by an unauthorized user to 100 m 2D RMS [*Kremer, et al., 1990*]. SA is implemented by dithering the frequency of the signals leaving the GPS satellite; thus it affects both code and carrier signals. The ranging errors have a slowly varying component with a time constant on the order of 200 s. The magnitude of the errors has been found experimentally to be as much as much as 60 m 1-σ, in range, and 0.2 m/s 1-σ in range rate [*Chou, 1990; Kremer, et al. 1990*]. More typically it is less than 20 m. Figure 3.5 illustrates range errors for data collected simultaneously from two satellites by Chou at Stanford University on June 25, 1990. Satellite 16 exhibits the dominant time signature of a signal disturbed by SA, whereas satellite 20 shows the much smaller, random "white" errors present on an unafflicted satellite.

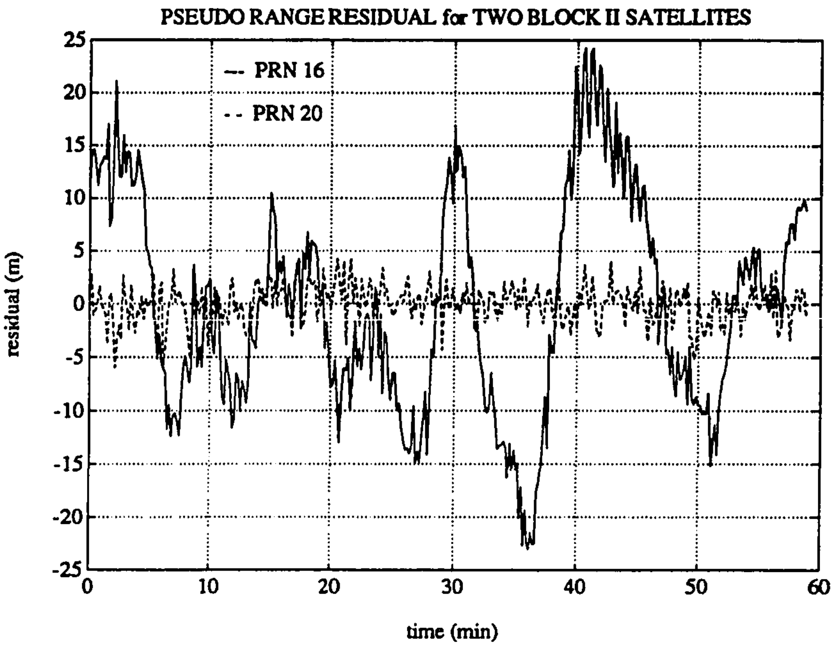

Figure 3.5 GPS Range Errors

The graph shows range errors for two satellites collected on 6/25/90. The solid line is satellite PRN 16, which we believe had SA turned on, and the dotted line is satellite PRN 20, which had its SA option turned off. Civilian users are not notified of the SA status of the satellites.

Chou identified the parameters of a second order Markov process which characterize the observed SA effects. The SA induced range error (ε_{SA}) is modeled as follows:

$$\frac{d^2\varepsilon_{SA}}{dt^2} + 2\,\beta\frac{d\varepsilon_{SA}}{dt} + \beta^2\varepsilon_{SA} = w_{SA}\ , \qquad w_{SA} \sim N(0{,}4\beta^2\sigma^2) \tag{3.3}$$

where he determined $\beta \approx 0.011$ sec^{-1} and $\sigma \approx 14.3$ m. The correlation time, which is related to the paramter β, is 190 sec. These numbers typically vary by about 10%.

Authorized users may obtain access to an SA key, which is embedded in the GPS receiver, and permits them to undo the signal variations caused by SA. It is likely that GP-B could justify this type of authorization.

The user receiver causes GPS errors mainly associated with thermal noise and its internal clock drift. Receiver noise is typically white with standard deviations of 1 m for C/A code measurements, and 0.5 cm/s for carrier measurements. The clock drift depends on the type of oscillator. In most cases this drift will be quite large and must be determined in the solution for the user location. Two or three variables- clock bias, drift, and possibly change in the drift rate, are usually added to the solution set.

As the GPS signal travels from the satellite to the user receiver it is affected by the environment. Delays are introduced by the ionosphere and troposphere. Indirect signals reflecting off nearby surfaces may cause signal interference known as multipath. Tropospheric delay is not a problem for GP-B as long as the elevation mask angle is set to zero degrees or higher, because at an altitude of 650 km, the spacecraft is well above the 80 km upper limit of the troposphere.

The ionosphere occupies the region from about 350 km to 1000 km, but the ion density drops off quickly above about 500 km. Signals passing through the ionosphere are retarded by an amount proportional to their frequency and the number of free electrons encountered. Thus, dual frequency receivers are able to use the two measurements to calibrate the signal delay due to this error source down to under about 1 m. Single frequency users employ a model of the ionospheric delay which eliminates about 75% of the error. For GP-B, dual frequency calibration should reduce the error to under 0.5 m, whereas modeling would leave an error of about 2 m. The range rate error due to variation in the ionospheric delay is assumed to be 0.5 cm/s for both single and dual frequency. Again the elevation mask angle should be set no lower than zero degrees to avoid looking at signals passing through the densest part of the ionosphere.

Errors induced by multipath are highly dependent on the type of receiver and environment surrounding the antenna. P code receivers tend to be more resistant to multipath for two reasons. The nature of the code allows the receiver to identify indirect signals which are delayed by more than 1.5 chip widths, that is 45 m for P code and 450 m for C/A [*Hagermann, 1973*]. Signal reflections from spacecraft solar panels or other structures may cause some errors for GP-B, but because it is highly geometry dependent the exact values cannot yet be determined. Placing the antennas on the tips of the solar panels may help to alleviate this potential problem. We have assumed a preliminary error budget of 2 m range and 0.5 cm/s range rate for multipath.

The total error budget for the high accuracy receiver considered in this study, is 5 m 1-σ, for the range, and 0.01 m/s 1-σ, for the range rate. These errors are assumed to be uncorrelated between measurement epochs which occur at 10 second intervals. The low accuracy receiver error is dominated by SA effects. Its range and range rate errors are modeled by a second order Markov process as given in Eq. 3.3. The precise digital model used in the simulation will be presented in Section 3.6.1.1. Typical range errors are 20-30 m, and range rate errors are 0.1-0.2 m/s.

3.5. Navigation Processor

The main function of the navigation processor is to extract the GP-B orbit information from the GPS data, and to provide an estimate of the current deviation from the target orbit to the control system. Additional housekeeping tasks such as antenna management, GPS signal integrity checking, and data processing for transmission to the ground, must also be performed. Orbit estimation for the closed loop control is accomplished by propagating a simplified dynamic model, and incorporating outside information from GPS. The dynamic model is divided into two parts- the reference state, and the deviation state.

Figure 3.6 shows a schematic of the navigation system. In the following sections each of the functions is described with primary emphasis put on orbit estimation.

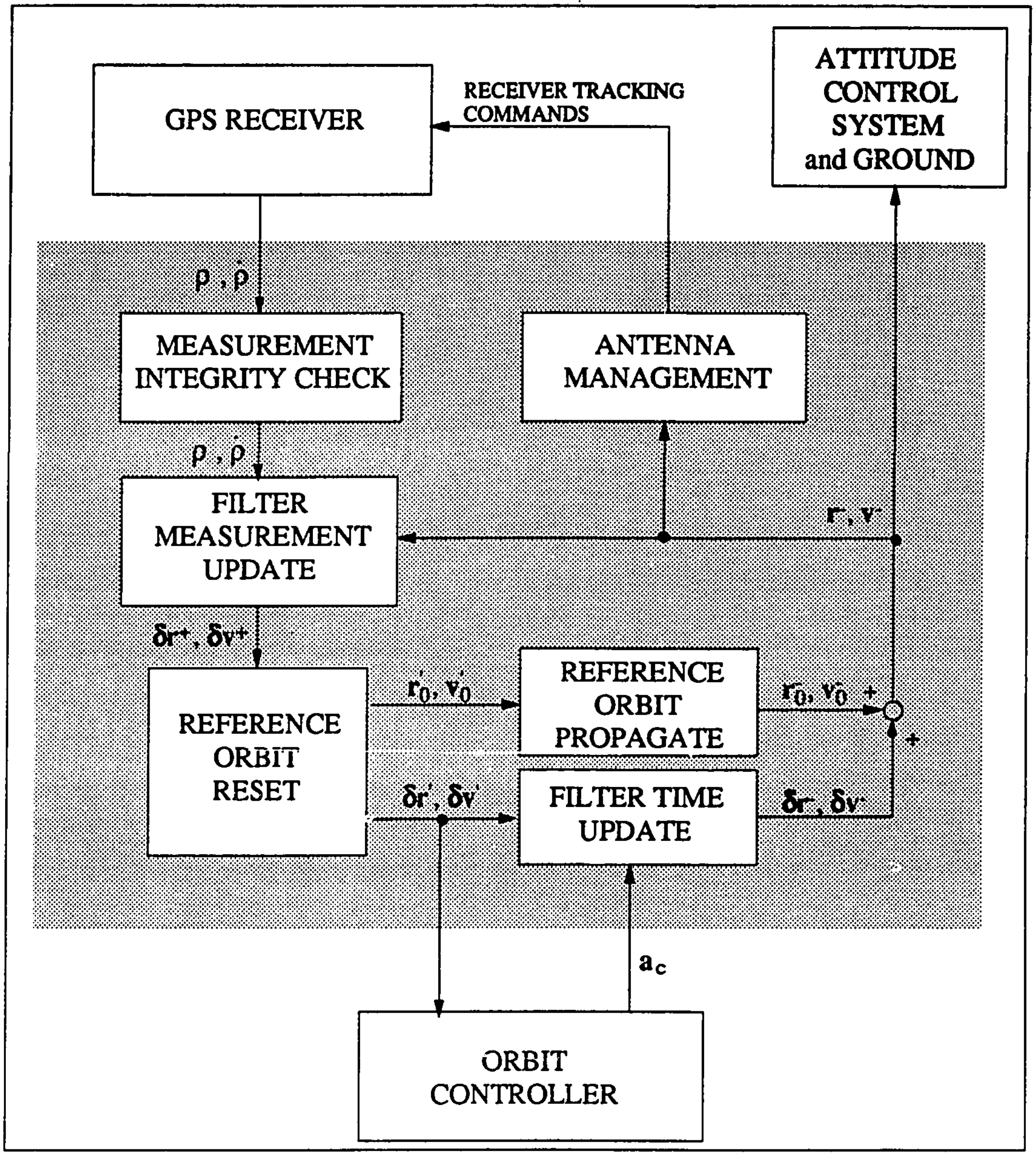

GPS RECEIVER
RECEIVER TRACKING COMMANDS
ATTITUDE CONTROL SYSTEM and GROUND
$\rho, \dot{\rho}$
MEASUREMENT INTEGRITY CHECK
ANTENNA MANAGEMENT
$\rho, \dot{\rho}$
FILTER MEASUREMENT UPDATE
r^-, v^-
$\delta r^+, \delta v^+$
REFERENCE ORBIT RESET
r_0', v_0'
REFERENCE ORBIT PROPAGATE
r_0, v_0
+
+
$\delta r', \delta v'$
FILTER TIME UPDATE
$\delta r^-, \delta v^-$
a_c
ORBIT CONTROLLER

Figure 3.6 Navigation Processor Diagram.

Shaded region represents the components and functions of the navigation processor. Inputs are GPS measurements and commanded control accelerations. Output to the orbit controller is the estimated deviation from the reference orbit. Spacecraft position and velocity state is output to the attitude control system and ground.

3.5.1 Reference State

The navigation reference state is based on the closed form model of short term orbit variations due to J_2 which was described by Eq. 2.21-2.23. The reference mean orbit is assumed to be precisely polar ($i'_0 = 0$ deg), with its node aligned to the guide star Rigel ($\Omega_0 = 78.474$ deg). The reference mean position within the orbit plane is propagated according to $u_R(\, t+T\,) = u_R(t) + n_R\, T$.

This mean orbit motion defines a Hill reference frame ($\mathbf{i}^H{}_1, \mathbf{i}^H{}_2, \mathbf{i}^H{}_3$), with mean orbit rate of n_R, as was illustrated in Figure 2.2. The Hill frame is related to the inertial frame ($\mathbf{i}^I{}_1, \mathbf{i}^I{}_2, \mathbf{i}^I{}_3$), by a body fixed rotation of Ω_0 about $\mathbf{i}^I{}_3$, followed by a 90 deg rotation about the node, and u_R about $\mathbf{i}^H{}_3$.

The eccentricity of the reference orbit is taken to be equal the target value, that is $\xi_R = 0.0000$, $\eta_R = 0.001336$. At any time, t, the reference state is then given by

$$\mathbf{r}_R = \begin{bmatrix} \left(r_0 + \delta r_R \right) \mathbf{i}^H{}_1 \\ r_0\, \delta u_R \quad \mathbf{i}^H{}_2 \\ 0 \qquad \mathbf{i}^H{}_3 \end{bmatrix} \qquad \mathbf{v}_R = \begin{bmatrix} \left(\delta \dot{r}_R - n_R\, r_0\, \delta u_R \right) & \mathbf{i}^H{}_1 \\ \left\{ n_R \left(r_0 + \delta r_R \right) + r_0\, \delta \dot{u}_R \right\} & \mathbf{i}^H{}_2 \\ 0 & \mathbf{i}^H{}_3 \end{bmatrix} \tag{3.4}$$

where n_R, δr_R, δu_R, $\delta \dot{r}_R$, and $\delta \dot{u}_R$ were defined in Eq. 2.23.

After each GPS measurement update, the mean radius and argument of latitude of the reference orbit are reset to reflect the best estimate of the current spacecraft position. The details of the orbit reset will be described in Section 3.5.2.2. There are two reasons for doing this reset. The first is that an extended Kalman filter works better if the deviations from the point about which it is linearized are small. The second is that since there is a rather wide range of acceptable values for the semimajor axis; thus, there is no reason to expend control effort trying to precisely achieve a 650 km altitude. In fact, the injection accuracy of the Delta upper stage already puts the orbit within the required semimajor axis limits.

3.5.2 Deviation State

The current estimate of the spacecraft state is given by

$$\hat{\mathbf{r}} = \mathbf{r}_R + \widehat{\delta\mathbf{r}}, \quad \hat{\mathbf{v}} = \mathbf{v}_R + \widehat{\delta\mathbf{v}} \tag{3.5}$$

where $\widehat{\delta\mathbf{r}}$ and $\widehat{\delta\mathbf{v}}$ are the estimated relative position and velocity, or deviation state.

The deviation state is assumed to be governed by Hill's equations, linearized about the mean orbit. The discrete dynamic model decouples into three parts, the in-plane motion, the out-of-plane motion, and the receiver clock dynamics, as follows:

$$\begin{bmatrix} x_{Hk+1} \\ \dot{x}_{Hk+1} \\ y_{Hk+1} \\ \dot{y}_{Hk+1} \end{bmatrix} = \Phi_{\text{IN-PLANE}} \begin{bmatrix} x_{Hk} \\ \dot{x}_{Hk} \\ y_{Hk} \\ \dot{y}_{Hk} \end{bmatrix} + \Gamma_{\text{IN-PLANE}} \begin{bmatrix} a_{c\,x} \\ a_{c\,y} \end{bmatrix} + \mathrm{w}_{\text{IN-PLANE}}$$

$$\begin{bmatrix} z_{Hk+1} \\ \dot{z}_{Hk+1} \end{bmatrix} = \Phi_{\text{OUT-of-PLANE}} \begin{bmatrix} z_{Hk} \\ z_{Hk} \end{bmatrix} + \Gamma_{\text{OUT-of-PLANE}} \begin{bmatrix} a_{c\,z} \end{bmatrix} + \mathrm{w}_{\text{OUT-of-PLANE}} \tag{3.6}$$

$$\begin{bmatrix} b_{k+1} \\ f_{k+1} \end{bmatrix} = \Phi_{\text{CLOCK}} \begin{bmatrix} b_k \\ f_k \end{bmatrix} + \mathrm{w}_{\text{CLOCK}}$$

where

$$\Phi_{\text{IN PLANE}} = \begin{bmatrix} 4 - 3\cos n_R t & \sin n_R t & 0 & 2(1 - \cos n_R t) \\ 3 \sin n_R t & \cos n_R t & 0 & 2 \sin n_R t \\ -6(n_R t - \sin n_R t) & -2(1 - \cos n_R t) & 1 & 4 \sin n_R t - 3\, n_R t \\ -6(1 - \cos n_R t) & -2 \sin n_R t & 0 & 4 \cos n_R t - 3 \end{bmatrix}$$

$$\Phi_{\text{OUT-of-PLANE}} = \begin{bmatrix} \cos n_R t & \sin n_R t \\ -\sin n_R t & \cos n_R t \end{bmatrix} \quad \Phi_{\text{CLOCK}} = \begin{bmatrix} 1 & n_R t \\ 0 & 1 \end{bmatrix}$$

$$\Gamma_{\text{IN-PLANE}} = \frac{1}{n_R^2}\begin{bmatrix} 1 - \cos n_R t & 2(n_R t - \sin n_R t) \\ \sin n_R t & 2(1 - \cos n_R t) \\ -2(n_R t - \sin n_R t) & 4\,(1 - \cos n_R t) - \frac{3}{2} n_R^2 t^2 \\ -2(1 - \cos n_R t) & 4 \sin n_R t - 3\, n_R t \end{bmatrix} \qquad \Gamma_{\text{OUT-of-PLANE}} = \frac{1}{n_R^2}\begin{bmatrix} 1 - \cos n_R t \\ \sin n_R t \end{bmatrix}$$

$w_{\text{IN-PLANE}}$, $w_{\text{OUT-of-PLANE}}$, and w_{CLOCK} represent the discrete disturbance vectors, and t is the time interval between measurements. In the filter, the disturbances will be assumed to be zero mean, gaussian, white sequences. In fact, the disturbances encompass all the unmodeled dynamics and are highly correlated. As a result, the process noise in the filter will have to be set artificially high to prevent filter divergence in the presence of these model violations.

3.5.2.1 Kalman Filter

An extended Kalman Filter implemented in square root form is used to propagate the deviation state and GPS receiver clock error. The deviation state estimate, denoted by $\hat{x}$, consists of the in-plane components, $x_H, \dot{x}_H, y_H$, and $\dot{y}_H$, the out-of-plane components, z_H, and $\dot{z}_H$, and the clock variables, b and f. Based on the dynamic models presented in the expressions above, the state estimate is propagated according to the following:

$$\hat{x}_{k+1}^{-} = \begin{bmatrix} \Phi_{\text{IN-PLANE}} & & \\ & \Phi_{\text{OUT-of-PLANE}} & \\ & & \Phi_{\text{CLOCK}} \end{bmatrix} \hat{x}_k^{+} + \begin{bmatrix} \Gamma_{\text{IN-PLANE}} & 0 \\ 0 & \Gamma_{\text{OUT-of-PLANE}} \\ 0 & 0 \end{bmatrix} \left[\begin{array}{c} a_{c\,x} \\ a_{c\,y} \\ \hdashline a_{c\,z} \end{array} \right] \tag{3.7}$$

The (-) and (+) signs indicate estimates before and after a measurement update, respectively. The measurement covariance is also propagated based on the transition matrix, and the process noise covariance, Q. The discrete process noise covariance (W) is computed from

$$W = \int_0^t \Phi(t)\, G\, Q\, G^T\, \Phi^T(t)\, dt \tag{3.8}$$

where G is the disturbance input distribution matrix, and the Q matrix is based on the expected disturbance acceleration levels. Typically, this process noise must be set artificially large if the unmodeled dynamics are correllated rather than white to make the filter converge properly.

The measurement update is given by

$$\hat{x}_k^+ = \hat{x}_k^- + K_k \begin{bmatrix} \rho_i - \hat{\rho}_i \\ \dot{\rho}_i - \hat{\dot{\rho}}_i \end{bmatrix}_k \tag{3.9}$$

The predicted values of the measurements $\hat{\rho}_i$ *and* $\hat{\dot{\rho}}_i$, are computed based on the current estimated state from Eq. 3.5, and the satellite position and velocity, as follows:

$$\begin{aligned} \hat{\rho}_i &= |\Delta \hat{\mathbf{r}}_i| + \hat{b} = \hat{\mathbf{e}}_i^T\, \mathbf{r}_{GPS\,i} - \hat{\mathbf{e}}_i^T\, \hat{\mathbf{r}} + \hat{b} \\ \hat{\dot{\rho}}_i &= \frac{\Delta \hat{\mathbf{r}}_i^T\, \Delta \hat{\mathbf{v}}_i}{|\Delta \hat{\mathbf{r}}_i|} + \hat{f} = \hat{\mathbf{e}}_i^T\, \mathbf{v}_{GPS\,i} - \hat{\mathbf{e}}_i^T \hat{\mathbf{v}} + \hat{f} \end{aligned} \tag{3.10}$$

The gain vector, K_k is a function of the current error state covariance, the measurement noises, σ_ρ and $\sigma_{\dot{\rho}}$, and the measurement gradient vectors, $\mathbf{H}_\rho$ and $\mathbf{H}_{\dot{\rho}}$.

$$\begin{aligned} \mathbf{H}_\rho &= \left[-\frac{\Delta \hat{\mathbf{r}}^{H^T}}{|\Delta \hat{\mathbf{r}}|}, 0^T, 1, 0 \right] \\ \mathbf{H}_{\dot{\rho}} &= \left[\left(-\frac{\Delta \hat{\mathbf{v}}^H}{|\Delta \hat{\mathbf{r}}|} + \frac{\Delta \hat{\mathbf{r}}^{H^T} \Delta \hat{\mathbf{v}}}{|\Delta \hat{\mathbf{r}}|^3}\, \Delta \hat{\mathbf{r}}^{H^T} \right), -\frac{\Delta \hat{\mathbf{r}}^{H^T}}{|\Delta \hat{\mathbf{r}}|}, 0, 1 \right] \end{aligned} \tag{3.11}$$

3.5.2.2 Reference Orbit Reset

As explained before, after each measurement update the reference orbit is reset according to the following rules to improve the accuracy of the linearized model and prevent unnecessary expenditure of control authority.

$$r_0^+ = r_0^- + \widehat{x}_H^+ \qquad u_R^+ = u_R^- + \frac{\widehat{y}_H^+}{\left| \mathbf{r}_R + \delta\hat{\mathbf{r}}^+ \right|} \tag{3.12}$$

The deviations from this new mean orbit are computed and propagated in time by the Kalman Filter. In theory, one should also recompute the system matrices based on the new radius and orbit rate; however, this is computationally burdensome and does not have any noticeable effect on the results. Thus, the linearized model governing the deviation state is evaluated only once based on the target injection values.

Alternative methods for resetting the reference orbit were also considered, such as matching the *velocity* of the reference orbit rather than the position, to the current estimate, or some appropriately weighted combination of both position and velocity. No significant improvements in orbit trim time or estimation accuracy were observed, thus we opted for the conceptually more straightforward approach.

The best estimate of the spacecraft orbit can be determined by the following three steps. First compute the position and velocity in the Hill frame by summing the reference state and the deviation state; then transform to the inertial frame based on the current mean position; and finally compute the orbit elements from the inertial position and velocity. The instantaneous orbit elements can be transmitted to the ground to evaluate the performance of the closed loop system. The deviation state is sent directly to the controller and serves as the basis for computing the orbit trim commands.

3.5.3 Integrity Checking

An additional task assigned to the navigation processor is the verification of the integrity of the GPS measurements. Although in general the system is extremely reliable, there is the potential for a satellite failure to go undetected by the control segment for up to one hour. A satellite failure in this context includes events such as onboard clock failures, faulty ephemeris or clock model uploads, and extremely severe selective availability errors.

Because of the redundancy available in the full operational constellation, it is usually possible for a GPS user to detect such failures autonomously. Several techniques based on batch processing of the pseudo ranges from all satellites in view were developed by Parkinson and Axelrad [*1987, 1988*]. These methods evaluate the measurement residuals to isolate a potentially faulty satellite. The estimated maximum range error can then also be used to predict the approximate positioning uncertainty.

Such an approach could be implemented on GP-B to ensure reliable navigation estimates; however, given the need for an onboard navigation filter, a more straightforward check would be to discard any GPS measurement yielding a measurement residual greater than four times the expected standard deviation.

The loss of a few measurements or possible incorporation of faulty data is not critical for near Earth space navigation for two reasons. First, as will be shown in the simulation results, there are usually about 9, and almost always more than 7 satellites available at any time. Thus, the dependence on any one satellite measurement accuracy is diminished. Second, the GP-B satellite is in a orbit with period of about 97 min. With a mask angle of zero degrees, any one GPS satellite is *typically* only in view for 20-40 min. For these reasons, an integrity checking algorithm was not implemented in the closed loop orbit trim study.

For our particular closed loop navigation and control system, the effect of navigation errors is even further reduced by the low level of thrust involved in the orbit adjustment. Since maneuvers are carried out over several days, errors caused by poor estimates over a short period of time do not have a significant impact on the final orbit accuracy.

On the other hand, integrity verification is crucial if GPS information is to be used to reset or calibrate the Delta inertial navigation system. This system has a high thrust single burn capability which must be done correctly the first time. Implementation of some form of integrity verification for the boost phase must be done either on the Delta vehicle or in the GP-B receiver. This issue must be considered in the near future.

3.5.4 Antenna Management

The antenna management function involves determining which GPS satellites are in view of which onboard antennas and how to assign tracking channels appropriately. Ideally, a satellite should be tracked by the same antenna as long as possible. This minimizes the risk of loss of carrier lock which would decrease the ranging accuracy. As the GP-B satellite rolls with a 10 minute period, any satellite may pass through the whole field of view of a single antenna in as little as a few minutes.

An algorithm must be developed which takes as input the GPS satellite ephemerides, the spacecraft position estimate, and spacecraft attitude information, and as output sends a sequence of commands to the GPS receiver(s) designed to optimize the amount of GPS information obtained. The implementation of this scheme must be combined with a model of the spacecraft roll dynamics.

An additional topic which was not discussed in the preceeding sections, is the translation of the GPS measurements received by different antennas to the spacecraft center of mass (c.m.). In computing the position and velocity of this point, the processor must account for both the location of the antenna on the body and the spacecraft attitude, before using the measurements to update the navigation state. Until now it has been tacitly assumed that measurements are taken at the point of interest.

Once the science data collection begins the attitude of the GP-B spacecraft will be extremely well known. The pointing control system will keep the telescope axis of the vehicle aligned with the guide star to within 100 marcsec [*Parkinson and Kasdin, 1989*] and the roll control system maintains the roll phase locked in time to 50 arsec [*Parkinson and Crerie, 1990*]. Thus, the inertial position offsets of each antenna from the c.m. can be precomputed to better than 1 mm. This information will be important for postprocessing of the geodesy data.

The attitude information available during orbit trim maneuvers has not yet been determined. Following release from the launch vehicle, the GP-B symmetry axis will probably be pointed roughly at the guide star Rigel. Some form of coarse attitude information must be provided to the navigation filter. However, since the sequence of events has not been established, it is not clear at this time if the spacecraft will be rolling, or whether the pointing and roll control systems will be turned on. This will have some impact on the implementation of the GPS antenna management function.

Given the approximate spacecraft attitude, the magnitude and direction of a vector from the c.m. to each antenna can be determined in inertial coordinates. This vector is then added to the position estimate for the c.m. in computing the GPS measurement estimates in the Kalman Filter. Attitude rate information is used in a similar way to account for the velocity of the antennas relative to the c.m.

The details of this implementation have been omitted in this study but are critical in an overall system simulation, and practical orbit trim system design. Attitude and roll rate tagging of the raw GPS measurements for geodesy is imperative if centimeter level accuracy is to be achieved.

3.6 Navigation System Performance

The performance of the navigation system was evaluated by computer simulation. The first subsection provides the details of the simulation. Then results of a simulation of GPS satellite coverage are shown. Sections 3.6.3-4 present simulation results for the high accuracy and low accuracy receiver options respectively. The final section describes the navigation filter performance during closed loop system operation.

3.6.1 Simulation Description

Figure 3.7 illustrates the components of the navigation system simulation and their interactions. There are three main parts- the truth model, the navigation processor model, and the data storage and processing unit. When closed loop control is introduced, a fourth unit is added to compute the commanded controls.

3.6.1.1 Simulation Truth Model

The truth model consists of a dynamic model of the spacecraft orbit and the GPS system. The spacecraft orbit is propagated using the instantaneous orbit elements in the variational equations given in Eq 2.11. Perturbing forces due to Earth harmonics up to degree and order four are included.

Drag effects during the orbit trim are modeled as described in Section 2.7.1.

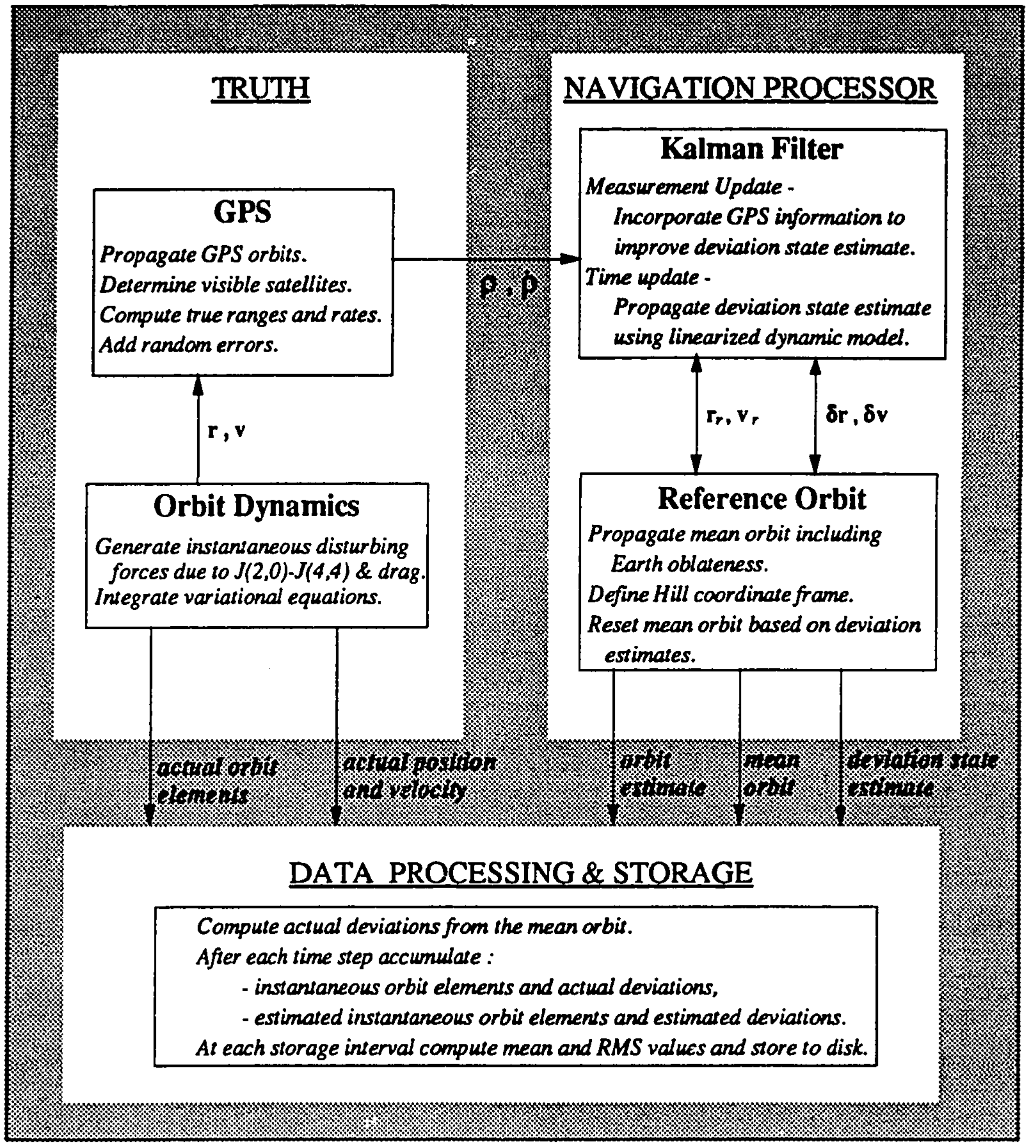
TRUTH
GPS
Propagate GPS orbits.
Determine visible satellites.
Compute true ranges and rates.
Add random errors.
r, v
Orbit Dynamics
Generate instantaneous disturbing forces due to J(2,0)-J(4,4) & drag.
Integrate variational equations.
ρ, ρ̇
NAVIGATION PROCESSOR
Kalman Filter
Measurement Update -
Incorporate GPS information to improve deviation state estimate.
Time update -
Propagate deviation state estimate using linearized dynamic model.
r_r, v_r
δr, δv
Reference Orbit
Propagate mean orbit including Earth oblateness.
Define Hill coordinate frame.
Reset mean orbit based on deviation estimates.
actual orbit elements
actual position and velocity
orbit estimate
mean orbit
deviation state estimate
DATA PROCESSING & STORAGE
Compute actual deviations from the mean orbit.
After each time step accumulate :
- instantaneous orbit elements and actual deviations,
- estimated instantaneous orbit elements and estimated deviations.
At each storage interval compute mean and RMS values and store to disk.

Figure 3.7 Navigation System Simulation Block Diagram.

The variational equations for the orbit elements are integrated numerically using a fourth order Runge-Kutta algorithm with a time step of 10 sec. Numerical roundoff errors are avoided by using extended precision variables and ensuring that all angle variables remain within 0-2π rad.

The orbit of each satellite in the GPS constellation described in Section 3.3 is modeled as circular with the given orbit elements. GPS measurements are constructed for each satellite within the field of view of the spacecraft at each 10 sec epoch. The pseudo range and pseudo range rate are generated by computing the true range and range rate, and adding the appropriate error for the type of receiver configuration considered. For the high accuracy receiver, the errors are zero mean gaussian random variables with standard deviations of 5 m for the range and 0.01 m/s for the range rate.

The lower accuracy GPS errors are modeled so as to include the correlated nature of SA as described in Section 3.4.4. The discrete version of the second order Markov process given in Eq. 3.4 is

$$\begin{bmatrix} \varepsilon_{SA\ i} \\ \dot{\varepsilon}_{SA\ i} \end{bmatrix}_{k+1} = \Phi_{SA} \begin{bmatrix} \varepsilon_{SA\ i} \\ \dot{\varepsilon}_{SA\ i} \end{bmatrix}_{k} + \begin{bmatrix} w_{\varepsilon_{SA}} \\ w_{\dot{\varepsilon}_{SA}} \end{bmatrix} \tag{3.13}$$

where, for $\sigma = 14.3$ m, $\beta = -.011\ \mathrm{s}^{-1}$, and a sampling time of 10 s [*Chou*, 1990],

$$\Phi_{SA} = \begin{bmatrix} 0.9941 & 8.9325 \\ -0.0011 & 0.7923 \end{bmatrix}, \quad \begin{aligned} w_{\varepsilon_{SA}} &\sim N\,(0, 0.58\ m) \\ w_{\dot{\varepsilon}_{SA}} &\sim N\,(0, 0.097\ m/s) \end{aligned}$$

Figure 3.8 illustrates typical simulated SA errors for a single satellite.

Additional zero mean gaussian errors of standard deviation 5 m and 0.01 m/s are added to the low accuracy pseudo range and range rate respectively, to represent receiver thermal noise and other uncorrelated error sources.

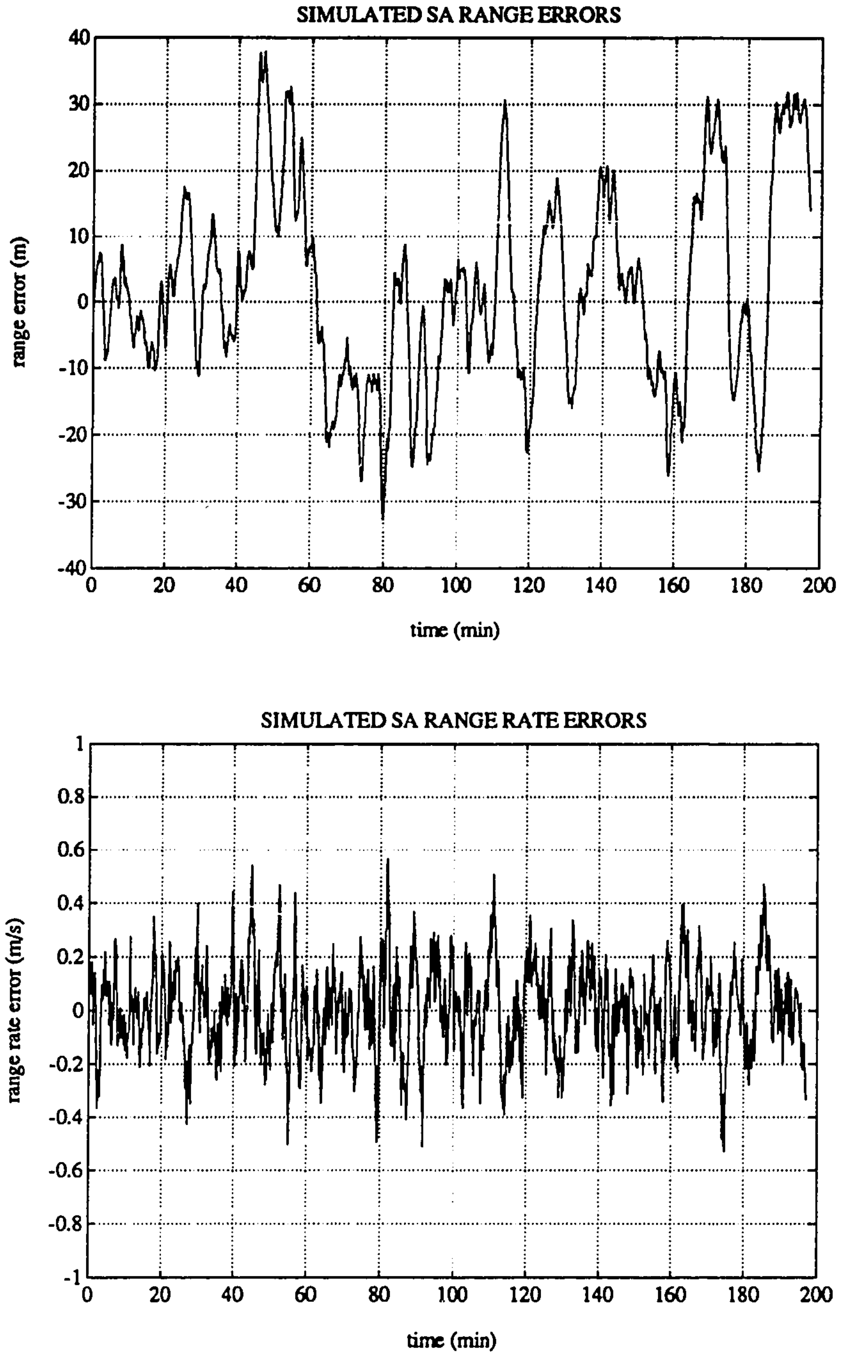

Figure 3.8 Simulated SA Errors for Low Accuracy Receiver.

The graphs show typical simulated pseudo range and range rate errors caused by SA.

3.6.1.2 Navigation Processor Model

The navigation processor is implemented based on the description in Section 3.4. The extended Kalman filter used to estimate the position and velocity deviations, and the two GPS receiver clock states is implemented in square root form. This formulation is less prone to numerical difficulties than the classical form. At each measurement epoch, it incorporates the measurements provided by the GPS unit to update its state estimate. The estimate of the deviation state in the Hill frame is then used to reset the mean reference orbit. Instantaneous orbit elements are computed based on the sum of the reference and deviation states.

Note that the dynamic model used by the navigation processor is much simpler than that of the truth model. Thus, one should expect the unmodeled dynamics to have a significant effect on the estimator performance. In fact, this turns out to be the case as will be seen in the later sections.

In addition, in the navigation filter the GPS measurements are assumed to be uncorrellated with zero mean, even though the errors generated by the truth model are correlated. The filter assumed standard deviations of the measurement errors for the high accuracy receiver are set at 5 m and 0.01 m/s, and 30 m and 0.2 m/s for the lower accuracy receiver.

3.6.1.3 Data Storage and Processing

A separate software unit was used to store and process the simulation data for later plotting and review. After each 10 sec measurement interval, the simulation provides the *true* instantaneous orbit elements and deviation state, and their estimates. The *mean* values of the actual elements, as well as both the mean and the RMS values of the estimation errors over the storage interval are stored on disk. For simulation run times of two orbits or less, the data is averaged and stored every minute. For simulation run times of one day or more, the data is averaged and stored every 10 minutes.

3.6.1.4 Initialization

Three data files are used to initialize the simulation parameters. The first sets up the time steps, storage intervals, and stop times. The other two select the actual orbit parameters and the navigation system parameters.

The actual orbit is initialized to one of three sets of conditions: an orbit approximately equal to the target, a good injection orbit representative of the upgraded Delta II upper stage system, and a poor injection orbit more typical of the current launch vehicle capability with no GPS update. The offsets of the instantaneous orbit elements from the target values which were used for the good injection and poor injection cases are listed below in Table 3.3. These are used only as representative examples. To properly verify the operation of the system, a Monte Carlo type study with a large number of runs using different initial conditions would have to be carried out and the results evaluated statistically.

The GPS measurement errors and Kalman filter parameters are initialized to either the accurate GPS receiver (σ_ρ= 5 m, $\sigma_{\dot\rho}$ = 0.01 m/s) or the lower quality GPS receiver (σ_ρ= 30 m, $\sigma_{\dot\rho}$ = 0.2 m/s). In both cases the continuous process noise variance for each of the filter states was set to 10^{-4} m^2/s^4. The initial estimates are set equal to the target orbit and the initial covariance is set arbitrarily large. In the simulation results, the first point is omitted from the plots and the computed statistics.

Table 3.3 Simulation Actual Orbit Initialization Errors. *Lists the values used for the simulations. The numbers are representative of possible injection orbit errors.*

	$\Delta\xi$	$\Delta\eta$	$\Delta i'$ (deg)	$\Delta\Omega$ (deg)	Δa (m)
Good Injection	-5×10^{-4}	-5×10^{-4}	-5×10^{-3}	-5×10^{-3}	-500
Poor Injection	$+1 \times 10^{-3}$	$+1 \times 10^{-3}$	$+1 \times 10^{-2}$	$+1 \times 10^{-2}$	+500

3.6.2 Coverage

Figure 3.9 illustrates the typical GPS satellite availability for GP-B. The spacecraft is assumed to have a 180 deg view angle centered about the zenith. The results shown are for one arbitrary orbital period and one 24 hr period. For this one day segment there are always between 6 and 12 satellites visible, with 8 or more in view about 95% of the time. Although the exact pattern of available satellites will shift each day, the general result stays about the same. Thus, there will always be sufficient satellites for GP-B to navigate reliably even in the event of a single satellite outage, and probably enough redundancy to permit the implemtation of an autonomous integrity verification scheme to discard potentially faulty measurements.

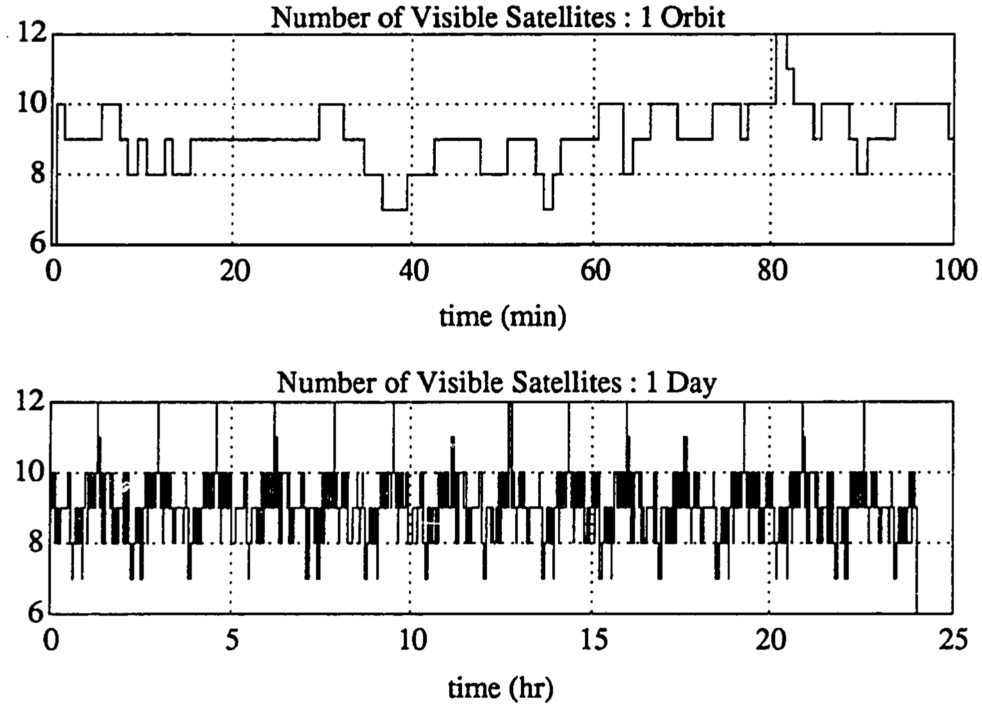

Figure 3.9 GPS Satellite Coverage for GP-B.

The bottom graph shows the number of visible satellites(elevation > 0 deg) over a one day period. The top one shows an expanded view of the coverage pattern for a single orbit.

3.6.3 High Accuracy Results

The simulation was run with the higher accuracy GPS receiver (range error of 5 m, 1-σ, range rate error of 0.01 m, 1-σ). Figures. 3.10-11 show the orbit element estimation errors, and the errors in the estimates of the deviations from the reference orbit in Hill's coordinates, respectively. The errors shown are averaged over the data storage interval of 1 minute. In this first case (NAV1), the GP-B spacecraft orbit was initialized as closely as possible to the target orbit. The mean errors over one orbit are well below 10% of the injection error requirements specified in Table 2.11. Table 3.4 lists the RMS and mean errors for each of the orbit elements and components of the state. In particular, the coinclination estimate which is the most critical parameter for orbit injection, has a mean error of only 0.1 x 10^{-5} deg (< 0.2 m) over the second orbit, and an RMS error of 3.2 x 10^{-5} deg (4 m).

The estimation error statistics for two runs (NAV2, NAV3) with the same GPS receiver, but in orbits more typical of the injection accuracy capability of the Delta II, are also listed in Table 3.4. The initial conditions used are given in Table 3.3. Notice that there is an increase in the magnitude of the in-plane estimation errors particularly in the argument of latitude and semimajor axis, as the orbit deviates from the target. This is also reflected in the errors for the in-plane positions, x_H and y_H, which show an increase in the RMS errors, from 1.2 m to 12.1 m, 1-σ, in the radial direction, and 0.5 m to 9.8 m, 1-σ, in the along track direction. The time history of these errors is also more systematic than the best orbit case. This result is typical of an extended Kalman filter operating farther from its linearization point.

Table 3.4 summarizes the two orbit, high accuracy GPS receiver simulation statistics. All of the results meet the navigation requirements proposed for the orbit trim phase of the mission, and the target orbit results satisfy the science mission requirements as well. As will be shown in Chapter 4, fairly large estimation errors are quite tolerable when the orbit is far from the target. As long as the estimates are not larger than the orbit errors, the controller is able to compute the right commands to correct the orbit errors, and thereby bring it into a range where the navigation performance is improved. The low level of thrust used to adjust the orbit provides the opportunity for the errors to average over many orbits.

The high accuracy of the velocity measurements (less than 2 cm/s RMS error for estimates made every 10 sec), is due to the low noise level of the GPS carrier phase measurements (10 cm/s, 1-σ). This is the key element for obtaining highly accurate orbit estimates. By comparison, the performance of the lower accuracy receiver is severely hampered, most noticeably in the Hill velocity estimates by the lack of a good range rate measurement.

3.6.4 Low Accuracy Results

Figures 3.12-3.13 illustrate the estimation errors averaged over one minute intervals for a GPS receiver which does not have access to the SA key corrections. As in Figures 3.10-11, the orbit is initialized as closely as possible to the target orbit (NAV4). The RMS estimation error statistics for this run, as well as for two runs with the good (NAV5) and poor (NAV6) injection conditions are summarized in Table 3.5. The RMS errors with this receiver are found to be about an order of magnitude worse than the high accuracy receiver.

Although the mean and RMS values of the orbit estimates shown in the figures do not quite meet the recommended navigation performance criteria, they are of the right order of magnitude. The surprising feature of these results is not that they are worse than the high accuracy case, but rather that they are quite good, in spite of the large, time correlated errors produced by SA, which were not modeled explicitly in the navigation filter.

SA errors have a far less detrimental effect on orbit determination for near Earth spacecraft than on Earth bound vehicles for several reasons. The most obvious is the larger number of satellites which are visible at any time. Greater redundancy decreases the dependence on measurements from a particular satellite. Rapidly changing geometry is perhaps an even more important reason. For GP-B, or any similar near Earth spacecraft, any one GPS satellite is typically in view for 20-40 minutes. During this time the user/satellite geometry changes quite substantially, causing any bias error in the range measurement to be projected onto different components of the vehicle position vector. An Earth bound user on the other hand, may track the same satellite for several hours. Thus a bias in one satellite may pull the solution off the correct value for a significant period of time.

It will be demonstrated in Chapter 4, that *both the high and lower quality receivers work equally well in adjusting the spacecraft orbit.* However, it may be desirable for other reasons to use the better receiver onboard. For example, to improve orbit determination for ground verification.

3.6.5 Closed Loop Navigation Results

The last two figures in this chapter (Figures 3.14-15) illustrate the RMS estimation errors for the high accuracy (NAV7), and low accuracy (NAV8), GPS receivers when they are employed as part of a closed loop orbit trim system. The initial conditions in the runs were set to the good injection orbit, and the duration is 9 days. For the first two days no control is turned on. The time optimal control algorithm, which will be described in the following chapter, was then turned on for five days and turned off again for the last two.

The RMS coinclination and node errors in the good case (NAV7) are less than 0.4×10^{-4} deg (7 m) - well below the level of the injection accuracy requirements. The in-plane elements are also well within the acceptable limits. Notice in Figure 3.14 that the RMS error in these elements decreases as the controller drives the actual orbit closer to the target orbit requirements.

The performance of the lower accuracy receiver is shown in Figure 15 (NAV8). As we saw earlier in the two-orbit simulations, the RMS errors are about an order of magnitude worse than NAV7. Although the RMS coinclination error is only slightly less than the desired injection accuracy of 2.0×10^{-4} deg, we found that the controller performed well. Again an improvement in the in-plane elements can be observed as the orbit approaches the target.

Based on the results of this chapter, we expect that both types of receivers will serve well in the closed loop system. *For orbit trim purposes GP-B does not appear to require a GPS receiver which has the ability to remove the effects of selective availability.* However, other mission objectives, such as the Delta II navigation update or ground verification of the vehicle orbit, may favor the selection of an SA keyed unit. Further modeling and simulation of the detailed operation of the GPS receiver and navigation algorithms are required. We ***can*** expect that a navigation system such as the one described will fulfill the requirements of a closed loop orbit trim system. We now turn to the control system design and algorithm development.

Table 3.4 High Accuracy GPS Navigation Results. Summary of simulation results.

Simulation time is 2 orbits. GPS measurement errors are 5 m and 0.01 m/s, 1-σ. RMS of estimation errors taken at 10 sec intervals, over the entire simulation run are listed in Table 3.4a, and mean errors over the second orbit are listed in Table 3.4b. Results are shown for 3 different initial conditions - orbit approximately equal to the target, a good injection, and a poor injection orbit.

	Table 3.4a **RMS** Estimation Errors - *Good GPS*		
	NAV1 *Approximate Target Orbit*	NAV2 *Good Injection Orbit*	NAV3 *Poor Injection Orbit*
Orbit Elements			
ξ	1.6×10^{-6}	2.1×10^{-6}	2.5×10^{-6}
η	1.5×10^{-6}	1.6×10^{-6}	2.0×10^{-6}
i' (deg)	3.2×10^{-5}	3.1×10^{-5}	3.1×10^{-5}
Ω (deg)	2.9×10^{-5}	3.0×10^{-5}	3.1×10^{-5}
u (deg)	0.4×10^{-5}	3.7×10^{-5}	8.0×10^{-5}
a (m)	11.1	14.5	21.5
Deviation State			
x position (m)	1.17	5.55	11.9
y position (m)	0.52	4.51	9.8
z position (m)	0.45	0.67	1.2
x velocity (m/s)	12×10^{-3}	13×10^{-3}	14×10^{-3}
y velocity (m/s)	6×10^{-3}	7×10^{-3}	8×10^{-3}
z velocity (m/s)	6×10^{-3}	6×10^{-3}	6×10^{-3}

	Table 3.4b **Mean** Estimation Errors - *Good GPS*		
	NAV1 *Approximate Target Orbit*	NAV2 *Good Injection Orbit*	NAV3 *Poor Injection Orbit*
Orbit Elements			
ξ	-0.0×10^{-6}	-0.6×10^{-6}	1.1×10^{-6}
η	0.0×10^{-6}	0.3×10^{-6}	-0.6×10^{-6}
i' (deg)	0.1×10^{-5}	0.1×10^{-5}	0.0×10^{-5}
Ω (deg)	-0.2×10^{-5}	-0.2×10^{-5}	0.5×10^{-5}
u (deg)	0.0×10^{-5}	-0.2×10^{-5}	-1.2×10^{-5}
a (m)	0.7	-0.8	-1.5
Deviation State			
x position (m)	0.3	-0.5	-1.0
y position (m)	0.0	-0.3	-1.5
z position (m)	0.1	-0.4	0.7
x velocity (m/s)	0.2×10^{-3}	-1.6×10^{-3}	10.0×10^{-3}
y velocity (m/s)	0.0×10^{-3}	0.2×10^{-3}	0.3×10^{-3}
z velocity (m/s)	-0.0×10^{-3}	-1.0×10^{-3}	1.2×10^{-3}

Table 3.5 Lower Accuracy GPS Navigation Results. Summary of simulation results.

Simulation time is 2 orbits. GPS measurement errors are modeled to include SA effects in the range 200-40 m and 0.1-0.2 m/s. RMS of estimation errors taken at 10 sec intervals over the entire simulation run are listed in Table 3.5a, and mean errors over the second orbit are listed in Table 3.5b. Results are shown for 3 different initial conditions - orbit approximately equal to the target, a good injection, and a poor injection orbit.

	Table 3.5a **RMS** Estimation Errors - *Poor GPS*		
	NAV4 *Approximate Target Orbit*	NAV5 *Good Injection Orbit*	NAV6 *Poor Injection Orbit*
Orbit Elements			
ξ	21×10^{-6}	25×10^{-6}	34×10^{-6}
η	21×10^{-6}	23×10^{-6}	33×10^{-6}
i' (deg)	38×10^{-5}	41×10^{-5}	43×10^{-5}
Ω (deg)	37×10^{-5}	38×10^{-5}	38×10^{-5}
u (deg)	8×10^{-5}	9×10^{-5}	13×10^{-5}
a (m)	158	182	182
Deviation State			
x position (m)	15.6	22.2	18.1
y position (m)	9.8	10.8	15.5
z position (m)	7.7	9.0	7.0
x velocity (m/s)	142×10^{-3}	163×10^{-3}	213×10^{-3}
y velocity (m/s)	83×10^{-3}	97×10^{-3}	146×10^{-3}
z velocity (m/s)	69×10^{-3}	73×10^{-3}	75×10^{-3}

	Table 3.5b **Mean** Estimation Errors - *Poor GPS*		
	NAV4 *Approximate Target Orbit*	NAV5 *Good Injection Orbit*	NAV6 *Poor Injection Orbit*
Orbit Elements			
ξ	0.0×10^{-6}	-15.0×10^{-6}	25×10^{-6}
η	-0.8×10^{-6}	9.0×10^{-6}	-23×10^{-6}
i' (deg)	-2.5×10^{-5}	4.2×10^{-5}	3.5×10^{-5}
Ω (deg)	1.6×10^{-5}	-0.7×10^{-5}	0.2×10^{-5}
u (deg)	-0.3×10^{-5}	0.2×10^{-5}	-3.4×10^{-5}
a (m)	19	30	25
Deviation State			
x position (m)	5.7	10.1	3.4
y position (m)	-0.3	0.3	-4.1
z position (m)	2.0	-0.0	1.2
x velocity (m/s)	6×10^{-3}	14×10^{-3}	3×10^{-3}
y velocity (m/s)	4×10^{-3}	5×10^{-3}	10×10^{-3}
z velocity (m/s)	2×10^{-3}	2×10^{-3}	-4×10^{-3}

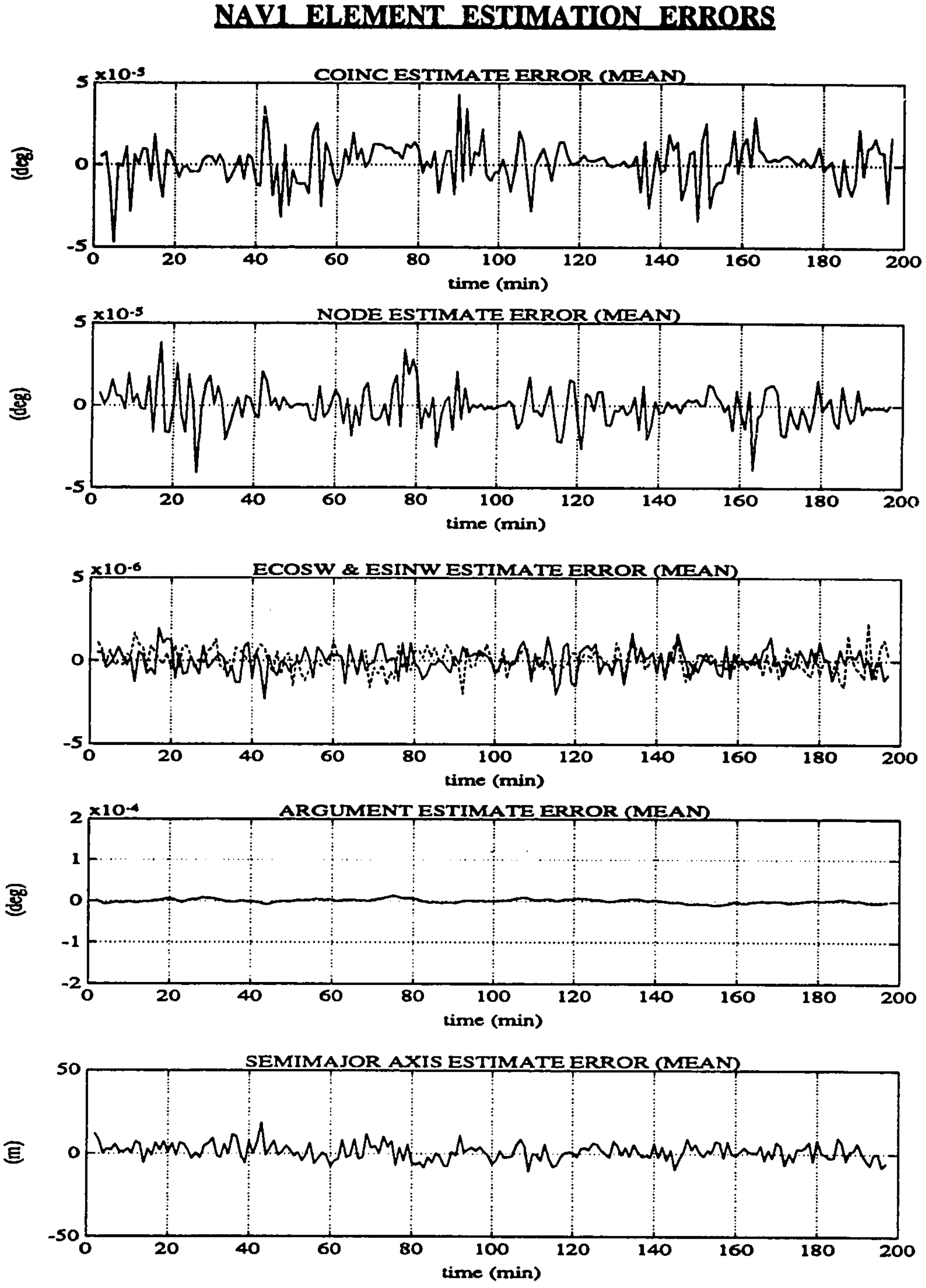

Figure 3.10 NAV1 Orbit Estimate Errors - Good GPS

Errors in estimates of instantaneous orbit elements averaged over 1 minute intervals. GPS errors 5 m & 0.01 m/s, 1-σ, and initial conditions on orbit set to the target values.

NAV1 DEVIATION STATE ESTIMATION ERRORS

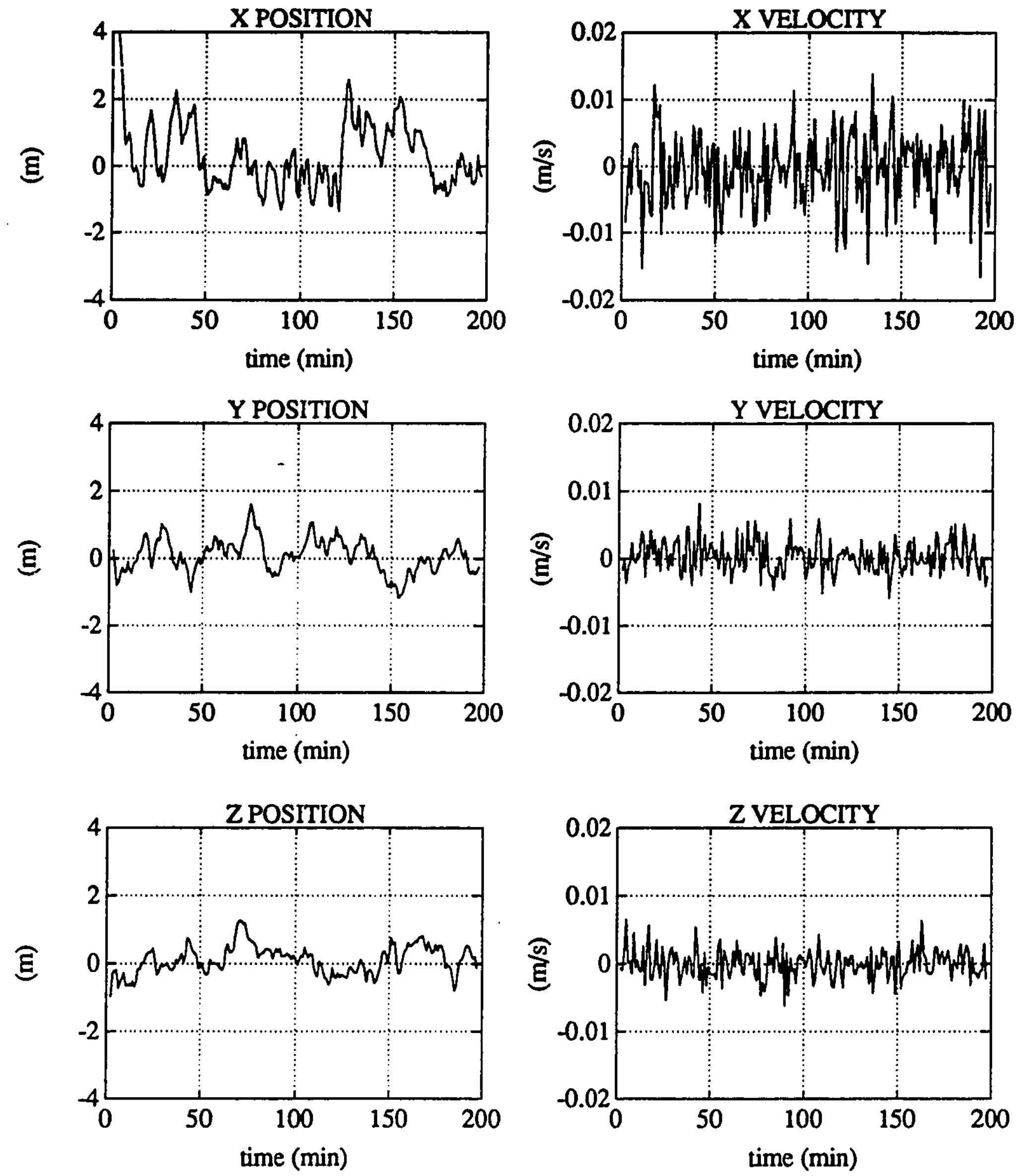

Figure 3.11 NAV1 Deviation State Estimate Errors - Good GPS

Errors in estimates of deviation from reference orbit in Hill coordinates averaged over 1 minute intervals. GPS errors 5 m & 0.01 m/s, 1-σ, and initial conditions on orbit set to the target values.

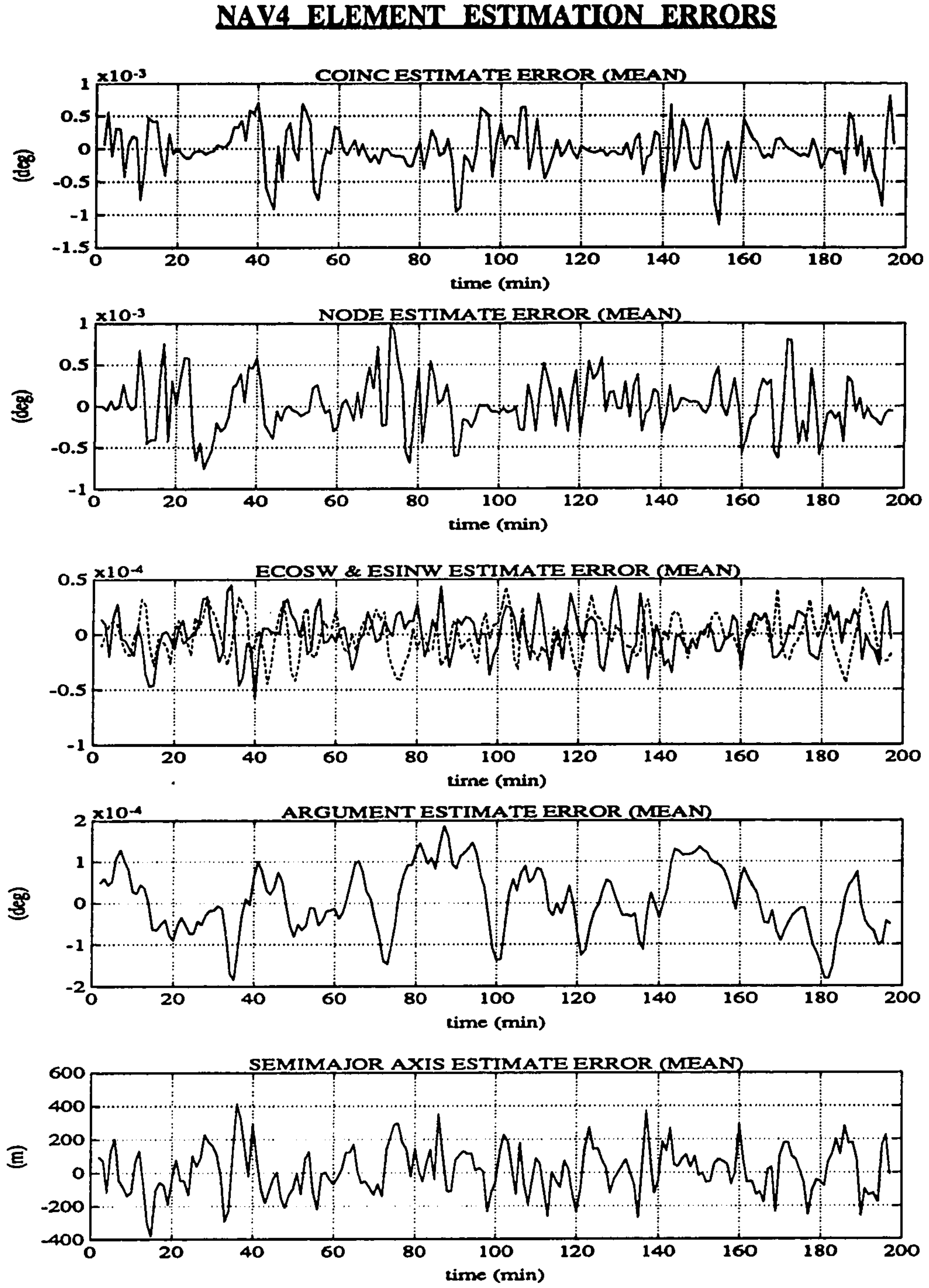
NAV4 ELEMENT ESTIMATION ERRORS

COINC ESTIMATE ERROR (MEAN)

NODE ESTIMATE ERROR (MEAN)

ECOSW & ESINW ESTIMATE ERROR (MEAN)

ARGUMENT ESTIMATE ERROR (MEAN)

SEMIMAJOR AXIS ESTIMATE ERROR (MEAN)

Figure 3.12 NAV4 Orbit Estimate Errors - Poor GPS

Errors in estimates of instantaneous orbit elements averaged over 1 minute intervals. Low accuracy GPS receiver (without SA key) and initial conditions on orbit set to the target values.

NAV4 DEVIATION STATE ESTIMATION ERRORS

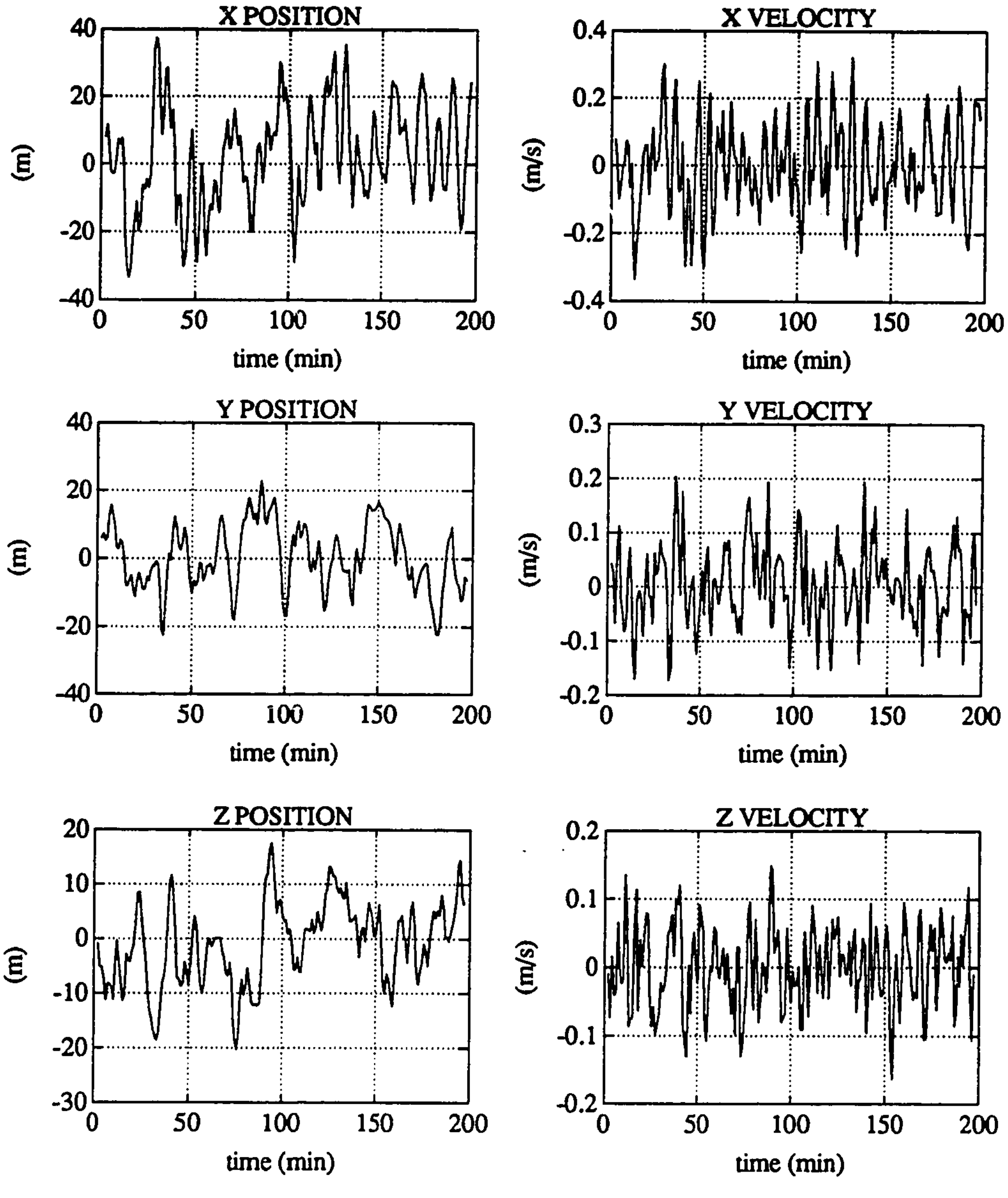

Figure 3.13 NAV4 Deviation State Estimate Errors - Poor GPS

Errors in estimates of deviation from reference orbit in Hill coordinates averaged over 1 minute intervals. Low accuracy GPS receiver (without SA key) and initial conditions on orbit set to the target values.

NAV7 ELEMENT ESTIMATION ERRORS

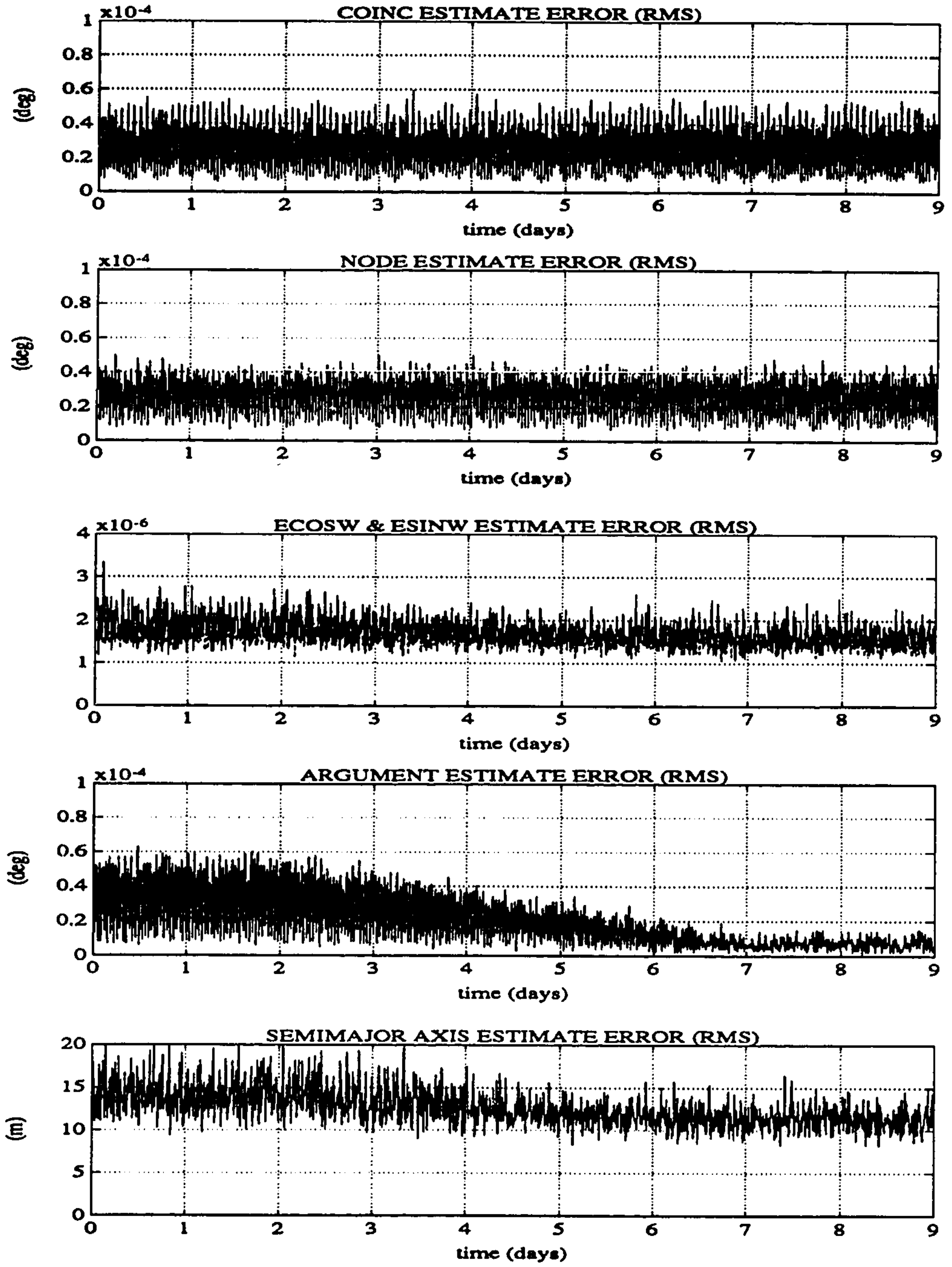

Figure 3.14 **NAV7** **Closed Loop Orbit Estimate Errors - Good GPS**

Good initial injection orbit and GPS errors of 5 m and 0.01 m/s 1-σ. Total run time of 9 days. Time optimal controller on for days 3-7.

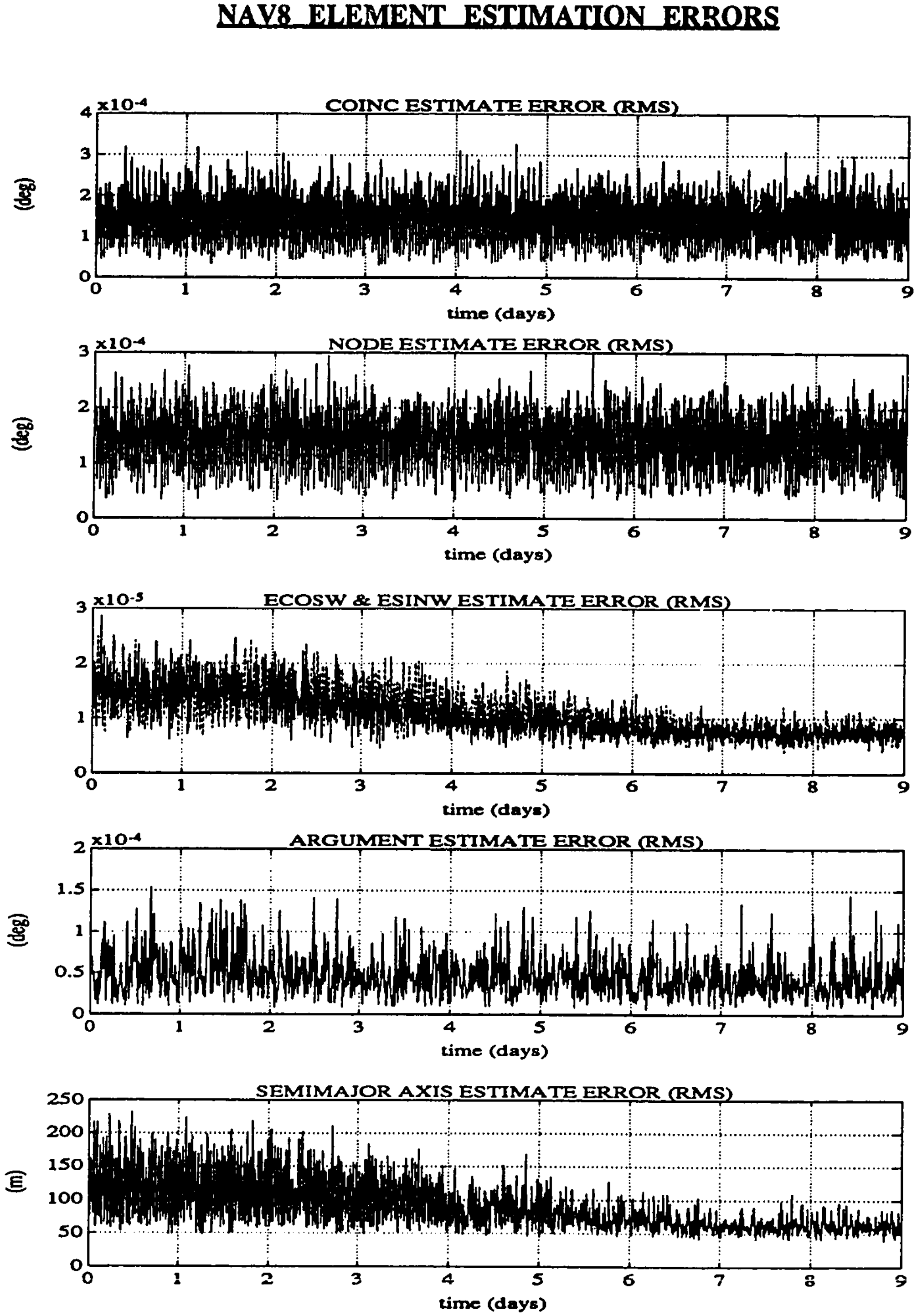

Figure 3.15 NAV8 **Closed Loop Orbit Estimate Errors - Poor GPS**

Good initial injection orbit and low accuracy GPS receiver (without SA key). Total run time of 9 days. Time optimal controller on for days 3-7.

CHAPTER 4. CLOSED LOOP ORBIT TRIM

4.1 Introduction

This chapter describes the guidance or control segment of the closed loop orbit trim system. The onboard controller objective is to issue commands to the helium thrusters so as to adjust the orbit of the GP-B spacecraft to the target specified in Chapter 2. A controller reference orbit is defined to account for out-of-plane motions caused by the Earth's gravitational field, which produce oscillations in the elements with periods on the order of a day. The deviations from the reference orbit are described by Hill's linearized equations. A time optimal, "bang-bang" control algorithm to adjust the orbit to the reference is presented. In addition, a design is considered which combines an LQR approach with the time optimal solution to reduce the number of switches as the actual orbit nears the reference.

The first section reviews the orbit trim requirements. This is followed by a description of the extremely low thrust (10 μg) helium actuators used for orbit control. The controller reference orbit is defined, and the control algorithms and simulated performance are presented.

4.2 Orbit Trim Requirements

The primary requirement on the closed loop orbit trim system is that the daily mean coinclination and node meet the targets specified in Chapter 2 within the allowable error margins. That is, for a 1997 start date, the mean value of the coinclination must be $(3.75 \pm 0.2) \times 10^{-3}$ deg, and the ascending node measured relative to Rigel must be $(-12.8 \pm 2.0) \times 10^{-3}$ deg. In general we will specify that the daily mean coinclination error should be less than 2×10^{-4} deg and the daily mean node error less than 2 x 10^{-3} deg. The performance simulation results which will be described in Section 4.5 indicate that these requirements can be met by the proposed orbit trim system.

A secondary objective of the orbit trim system is to adjust the eccentricity of the orbit to its frozen value. This is done to minimize the overall eccentricity during the course of the mission. The *desired* values of the orbit averaged eccentricity vector components are $\xi = (0 \pm 0.5) \times 10^{-3}$ and $\eta = (1.3 \pm 0.5) \times 10^{-3}$. It is quite possible that these requirements *can* be met by the Delta II. In section 4.5, we investigate a control scheme which can adjust the eccentricity to far better than these values if so required. It should be emphasized that the correction of the in-plane elements is far less critical than the orbit plane adjustments.

4.3 Control Actuator

Part of the challenge in designing an orbit trim system for GP-B was to employ the extremely low authority onboard helium thrusters for translational control. These thrusters are fueled by the cryogenic boiloff of superfluid helium from the experiment dewar. During the science data collection part of the mission, the helium thrusters perform as actuators for both the attitude and drag-free translational control systems.

The original design and testing of the helium thrusters was done in the 1970s by Bull and Chen [*Bull, 1972; Chen, 1973*]. Currently research is being conducted by Wiktor, Jafry, and Lee on thruster design, configuration, control, and performance for the GP-B spacecraft [*Wiktor, 1989, 1990*]. Wiktor analyzed various thruster configurations and dewar heating rates to find the maximum thrust available in the direction of the minimum control authority. It generally lies in the range of 1-10 mN. The *actual* thrust available will probably depend on the rate of dewar heating, which is primarily a function of the skin temperature of the dewar.

For the purposes of the orbit trim system, we have assumed a maximum thrust authority of 10 mN in each of the Hill frame directions. For the current spacecraft mass estimate of 2000 kg this corresponds to a specific force of 0.5 μg's. That is

$$|a_{cx}| < 5 \times 10^{-6}\, m/s^2\,, \quad |a_{cy}| < 5 \times 10^{-6}\, m/s^2\,, \quad |a_{cz}| < 5 \times 10^{-6}\, m/s^2 \quad (4.1)$$

Perhaps a more accurate way of limiting the control authority is to specify the *total* available. The control algorithm would then have to find the optimal steering angle to adjust the in-plane and out-of-plane elements simultaneously. One advantage of the approach we have taken is that the guidance law becomes merely a set of switching functions which can easily be evaluated in real time. For steering angle control, a set of desired trajectories must be determined *a priori*, and neighboring path controls computed onboard.

4.4 Controller Reference Orbit

A reference orbit for the controller is defined to account for the variations of the out-of-plane elements caused by gravitational forces with characteristic periods on the order of a day. In particular we model the twice daily oscillation in the coinclination due to $J_{2,2}$, and both once daily and three times daily variations in the node due to $J_{4,1}$, and $J_{4,3}$ respectively.

There are two reasons for doing this. The first is that the gravitational forces due to these dominant terms are far greater than the maximum control authority available from the onboard helium thrusters. This means that we ***could not*** eliminate these orbit plane motions through the use of the helium thrusters even if we wanted to. Thus by accounting for them in the reference, the controller does not attempt to counteract them at all.

The second reason is that once a satisfactory orbit trim has been completed, the control system will be turned off, and the drag compensation system will take over the translational control of the spacecraft. Thus to have the drag-free orbit be as close to the target as possible, we should account for the variations it will experience due to all the noncentral terms in the Earth's gravitational field plus the Sun, the Moon, and other planets. As a compromise between accuracy and simplicity, we only account for the effects of the *dominant* Earth terms, and expect that the orbit will change character somewhat after the controller has been turned off.

We saw in Section 2.4.1 that the short term coinclination variation was dominated by a twice daily oscillation produced by the $J_{2,2}$ term, where the rate is given by

$$\frac{d\,i'_{2,2}}{dt} = n\left(\frac{R_E}{a}\right)^2 2\ J_{2,2} \sum_{p=0}^{2} F_{2,2,p}\left(\frac{\pi}{2}\right) \left[-\sin\left(\psi_{2,2,p} - \varphi_{2,2}\right)\right] \tag{4.2}$$

and the reference coinclination is thus approximated by

$$\begin{aligned} i'_R(t) &= -\frac{3}{2} n\left(\frac{R_E}{a}\right)^2 J_{2,2} \cos 2\left(\lambda_R - \omega_E t - \varphi_{2,2}\right) + i'_T \\ &= 0.00189 \cos\left(2\omega_E t - 0.12\right) + i'_T \ \ deg \end{aligned} \tag{4.3}$$

which is illustrated in Figure 4.1. i'_T is the mean target coinclination specified based on the start date such as in Table 2.11.

The variation in the node is somewhat more complicated as was shown in Figure 2.5. Here there is a clear once daily oscillation, but other higher frequency terms are not negligible. As a compromise we have elected to model both the once daily and three times daily terms.

$$\begin{aligned} \frac{d\,\Omega_R}{dt} = -\ n\left(\frac{R_E}{a}\right)^4 & \left[F'_{4,1,2}\left(\frac{\pi}{2}\right) J_{4,1} \sin\left(\lambda_R - \omega_E t - \varphi_{4,1}\right)\right. \\ & \left. +\ F'_{4,3,2}\left(\frac{\pi}{2}\right) J_{4,3} \sin 3\left(\lambda_R - \omega_E t - \varphi_{4,3}\right)\right] \end{aligned} \tag{4.4}$$

Then after integrating and substituting values for the derivatives of the coinclination functions, the orbit, the right ascension of Rigel, and the geopotential coefficients, Ω_R is modeled by

$$\Omega_R(t) = 0.00108 \cos(\omega_E t + 2.50) + 0.00079 \cos(3\,\omega_E t + 1.97) + \Omega_T \; deg \quad (4.5)$$

which is illustrated in Figure4.2. Ω_T is the target node for the particular start date specified in Table 2.11. In the simulations this was set to zero.

The in-plane elements of the controller reference orbit (a, ξ, η and u) are set equal to the navigation reference values, and the reference position and velocity in the Hill frame are determined. The reference out-of-plane position, z_R, and velocity, $\dot{z}_R$, are subtracted from the deviation states estimated by the navigation system to find the out-of-plane state to be corrected.

4.5 Out-of-plane Time Optimal Control

This section describes the performance of a bang-bang control algorithm for the out-of-plane motions of the GP-B spacecraft. The objective is to achieve the target orbit in minimum time with the constraint that the maximum control authority is limited to 5×10^{-6} m/s^2. Simulation results are shown for typical injection conditions expected from the Delta II upper stage. In all cases the orbit trim requirements are satisfied. The duration of the trim maneuvers depends on the size of the injection errors and the limitations on control authority. The correction time is approximately proportional to the magnitude of the specific force.

The values of the estimated out-of-plane position and velocity relative to the controller reference orbit are used to determine what commands to issue to the helium thrusters.

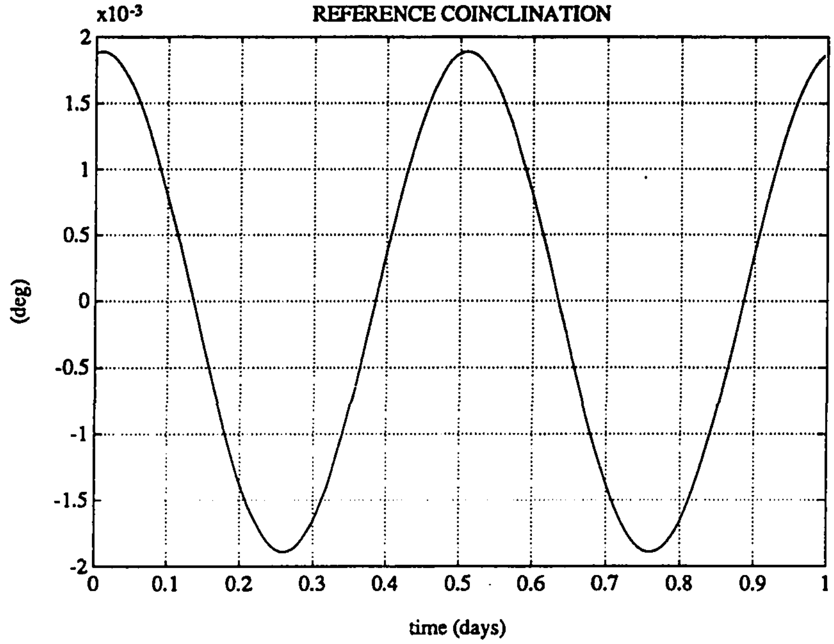

Figure 4.1 Reference Orbit Coinclination.

Mean should be set to target coinclination for the start date. Here it is set to zero.

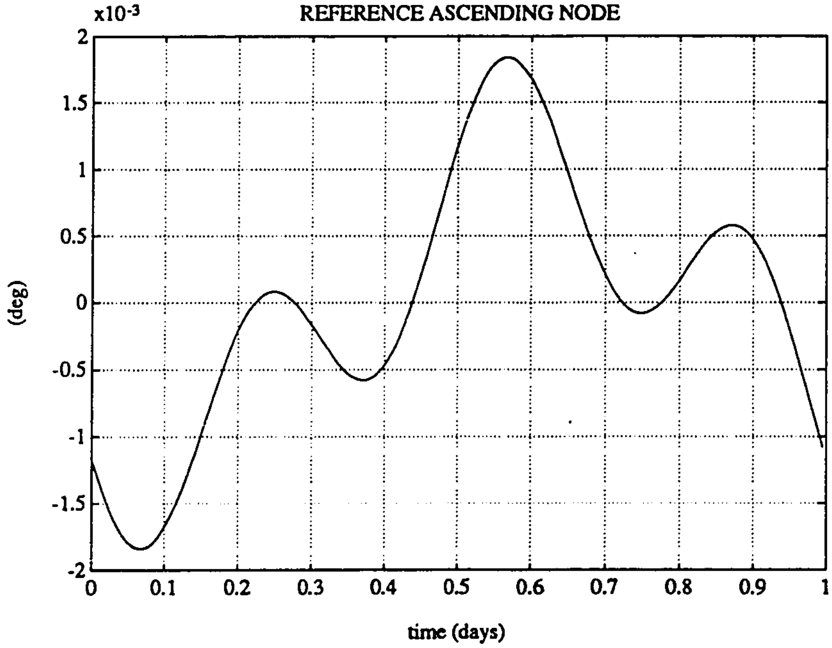

Figure 4.2 Reference Orbit Ascending Node.

Mean should be set to target ascending node for the start date. Here it is set to zero.

4.5.1 Algorithm

The out-of-plane orbit control problem is formulated as follows- compute a control $a_{cz}(t)$ to bring the position and velocity deviations from the reference plane, z and $\dot{z}$ to 0 in mimum time, subject to the dynamical and magnitude constraints given by

$$\begin{aligned} \ddot{z}_H + n^2 z_H &= a_{c\,z} \\ a_{c\,z} &= a_{max}\ u_z, \quad |u_z| \leq 1 \end{aligned} \tag{4.6}$$

The cost function is simply equal to the time. The well known solution to this problem is to command full authority control, that is $u_z = \pm 1$ at all times with the sign determined by the scalloped switching curve illustrated in Figure 4.3 [*c.f. Athans and Falb, 1966 or Bryson and Ho, 1975*]. This figure shows the phase plane along whose axes are plotted $n^2 z/a_{max}$ and $n\dot{z}/a_{max}$. The states are scaled so that the axes are unitless.

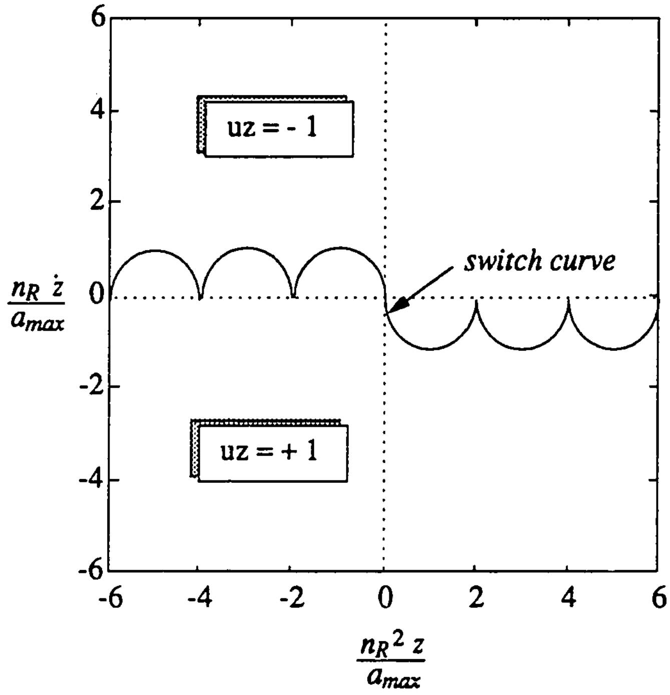

Figure 4.3 Switch Curve for Out-of-plane Control.

Phase plane for out-of-plane position and velocity. Location of the state within the phase plane determines the optimal control.

Figure 4.4 shows optimal trajectories in the phase plane for several arbitrary starting conditions. In the absence of control or disturbance forces, the deviation state would just move in a circle centered at the origin of the phase plane.. If the optimal control is issued, the trajectories will consist of circular arcs centered at $n^2 z / a_{max} = -1$ for points above the switching curve (i.e. $u_z = -1$) and $n^2 z / a_{max} = +1$ for points below ($u_z = +1$). The switching function is defined by

$$\frac{n_R \, \dot{z}_{switch}}{a_{max}} = \sqrt{1 - \left[2 \left(\left| \frac{n_R^2 \, z}{a_{max}} \right| mod \, 2 \right) - 1 \right]^2} \tag{4.7}$$

In theory, the time it takes to get to the origin can be calculated by summing the angles swept out by the circular arcs along the trajectory. The actual time to the origin will be different from this ideal situation because of errors in the state estimates, unmodeled dynamics, commanded acceleration errors, and phase delay associated with a digital control implementation. The performance of this algorithm was evaluated by computer simulation.

4.5.2 Closed Loop Performance

The time optimal out-of-plane control algorithm was added to the dynamics and navigation simulation described in Section 3.6.1. An additional control block takes the deviation state estimates from the navigation filter and computes control commands according to the algorithm described above. These are applied to both the true dynamic model and the estimator dynamic model.

In the simulations, the target values of the mean coinclination and node were both arbitrarily set to zero. For a more detailed study, different numbers would be used depending on the start date. In addition, the target value of the northward eccentricity

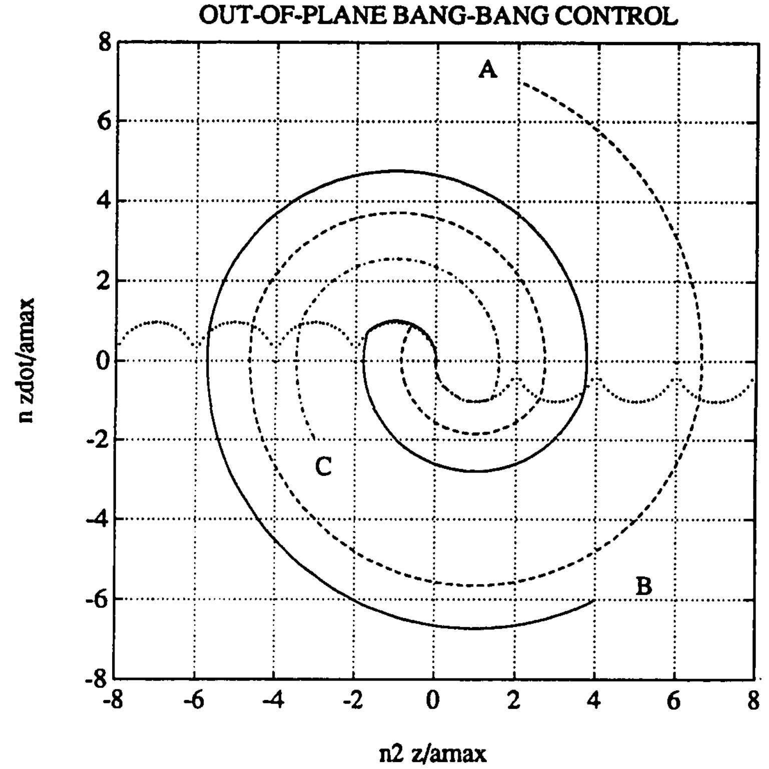

Figure 4.4 Optimal Out-of-plane Trajectories in the Z Phase Plane.

Curves A, B, and C represent the optimal trajectories for a harmonic oscillator with three different starting conditions. Each 180 deg circular arc takes half an orbit to complete (about 49 minutes).

was set to 0.0011 rather than the true frozen value of 0.0013 computed based on the odd harmonics up to degree 35. This value corresponds to the offset produced by J_3 alone, which is the only odd zonal harmonic term included in the simulation.

Figure 4.5 illustrates the simulation results for a good initial injection condition (CON1). A high accuracy GPS receiver is assumed, corresponding to the estimation results shown in Figure 3.14. For the first two days no control is applied. Notice the oscillations in the coinclination and node produced by the $J_{2,2}$, $J_{3,1}$, and $J_{4,3}$ terms. The controller is then turned on for five days. The orbit elements clearly move toward the desired zero values. After five days the controller is turned off. At this point the science data collection could begin, or a ground evaluation of the orbit may be performed to see if further adjustments are required. After the controller is turned off, there is a slight shift of both the coinclination and node due to simplifications in the controller reference orbit. However, the final mean errors are well within the orbit trim requirements. Table 4.1 lists the mean values for each of these three simulation phases.

Figure 4.6 shows similar results for a poor initial injection and a good GPS receiver. In this case the controller is on for 10 days, and again we include two days before and two days after the control period where no control commands are issued. The mean values of the elements are listed in Table 4.1.

An interesting feature to note in all of the plots is the that even when the control is turned on, the variation in the elements caused by the gravitational terms is not eliminated. Although the reference coinclination and node vary smoothly, the helium actuator does not have the control authority to suppress these oscillations. Figure 4.7 shows a three day simulation with the same starting condition as CON2 but a maximum control force of 10^{-4} m/s^2. In this case the elements are forced to precisely track the reference orbit. The fact that the actual thruster does not drive the orbit to the reference does not have an adverse impact on the performance since the deviations would reappear after the trim is completed anyway.

Table 4.1 also lists results for the same initial conditions as the first two runs, but with the *low accuracy* GPS receiver statistics (CON3, CON4). Plots of the simulation results are not shown *since they are indistinguishable from the higher accuracy runs.*

Larger estimation errors do occur for these runs; however, they do not adversely affect the orbit trim performance. Based on these results, from the standpoint of the closed loop orbit trim system there is no need for the Selective Availability key to be built into the GPS receiver carried onboard GP-B.

Table 4.1 Summary of Out-of-plane Closed Loop Simulation Results.
Lists the mean values of the coinclination and node for the first two days of each simulation before control is turned on, the mean values for the last day of controller operation, and the mean over the last two days after the controller has been turned off.

	Mean Values of Orbit Elements		
	First 2 Days Control Off	Last Day of Control On	Last 2 Days Control Off
CON1 - *Good GPS* *(Control On 5 days)*			
i' (deg)	-49.3×10^{-4}	-0.5×10^{-4}	-1.5×10^{-4}
Ω (deg)	-50.4×10^{-4}	0.0×10^{-4}	1.3×10^{-4}
CON2 - *Good GPS* *(Control On 10 days)*			
i' (deg)	100.1×10^{-4}	-0.4×10^{-4}	-2.0×10^{-4}
Ω (deg)	106.5×10^{-4}	-0.2×10^{-4}	-1.3×10^{-4}
CON3 - *Poor GPS* *(Control On 5 days)*			
i' (deg)	-49.3×10^{-4}	-0.5×10^{-4}	-1.4×10^{-4}
Ω (deg)	-50.4×10^{-4}	-0.1×10^{-4}	1.5×10^{-4}
CON4 - *Poor GPS* *(Control On 10 days)*			
i' (deg)	100.1×10^{-4}	0.2×10^{-4}	-0.8×10^{-4}
Ω (deg)	106.5×10^{-4}	0.2×10^{-4}	1.2×10^{-4}

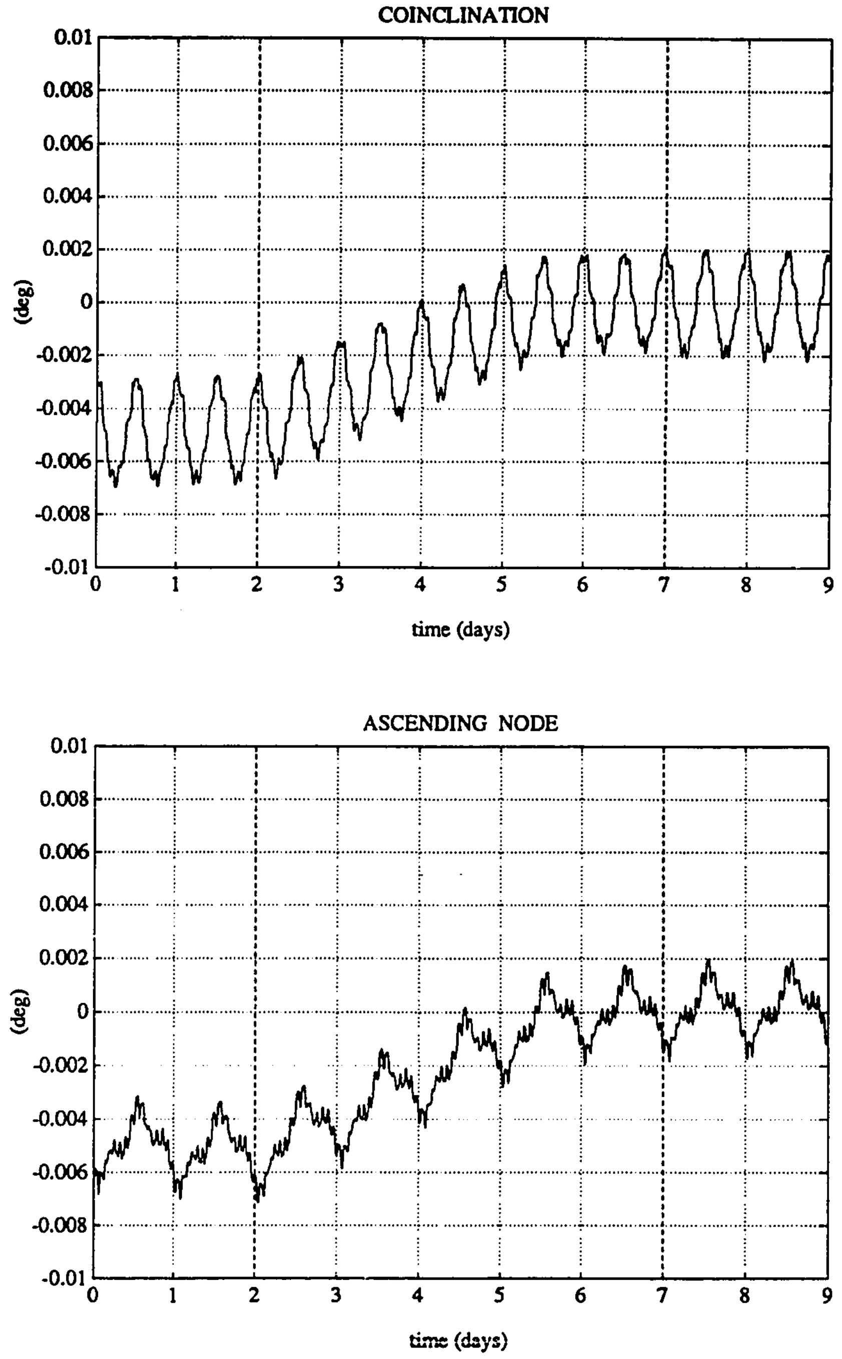

Figure 4.5 Out-of-plane Bang-Bang Control Results 9 Days - (CON1).

Good GPS receiver, good injection conditions. Mean values of the coinclination and node are shown. Control off days 1-2. Control on days 3-7. Control off days 8-9. Dashed lines indicate control ON/OFF switches.

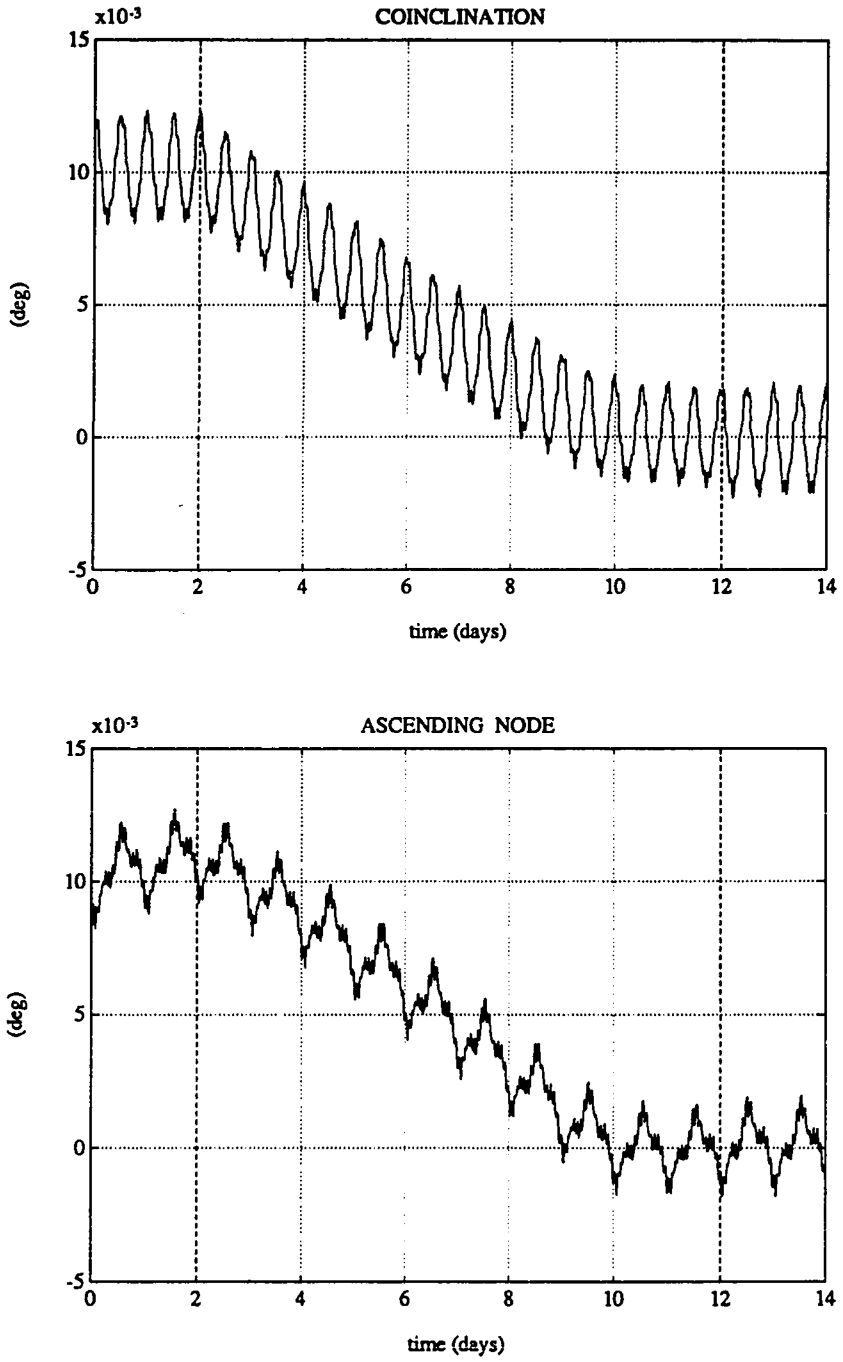

Figure 4.6 Out-of-plane Bang-Bang Control Results 14 Days - (CON2).

Good GPS receiver, poor injection conditions. Mean values of the coinclination and node are shown. Control off days 1-2. Control on days 3-12. Control off days 13-14. Dashed lines indicate control ON/OFF switches.

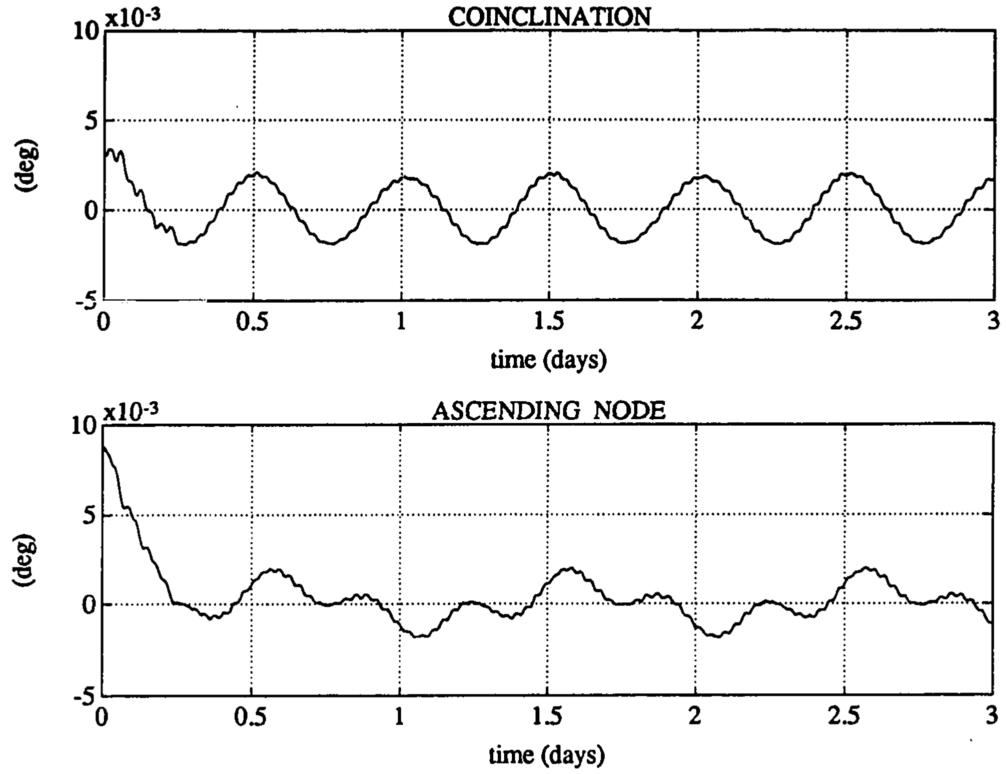

Figure 4.7 Higher Thrust Control Results 3 Days - (CON5).

Good GPS receiver, poor injection conditions. Mean values of the coinclination and node are shown. Control specific force of 10^{-4} *m/s*^{2} *is used. Control is on for 3 days. Notice that it tracks the reference orbit without deviations due to higher terms.*

A fundamental limitation on how well the orbit trim system can perform is the accuracy of the controller reference model. Dynamics not modeled in the closed loop system will lead to errors in the injection parameters; however, we have found them to be acceptably small. One other source of errors may be due to phase lag or chatter in the bang-bang controller implementation. In the following section we investigate a method for eliminating this potential problem and perhaps further improving the closed loop orbit trim performance.

4.5.3 LQR Control

As the orbit nears the target the bang-bang control system will have a tendency to switch rapidly back and forth or chatter. This is due to several effects including estimation errors, phase lag caused by the digital control implementation, and dynamic mismodeling. One way to alleviate this problem is to implement a proportional control scheme as the deviation state nears zero. It is a bad idea to use this proportional scheme all the time because it would then take the system longer to achieve the objective.

LQR gains were derived such that the control would reach saturation for an offset of 2 x 10^{-4} deg in coinclination or node, corresponding to a position error of 25 m or velocity error of 0.025 m/s. That is for errors larger than these values, the commanded control is ± a_{max} with the sign determined by the sign of the gains times the estimated states. Thus the control is given by,

$$\begin{aligned} u_{LQR} &= -\left(0.0015\, n_R^2\, z_H + 0.1620\, n_R\, \dot{z}_H\right) \\ a_{cz} &= a_{max}\, min\left(u_{LQR},\, sign(u_{LQR})\right) \end{aligned} \tag{4.8}$$

Figure 4.8 shows simulation results in which the LQR control law has been implemented (CON 6). The starting conditions and GPS receiver are the same as in CON 1. There is no significant difference in the results from the pure on/off case. This implies that the residual errors produced by our closed loop controller are primarily the result of the simplifications in the target dynamic model and the inability of the control actuators to overcome the higher order terms in the Earth's gravitational field, rather than chatter problems typically associated with on/off control.

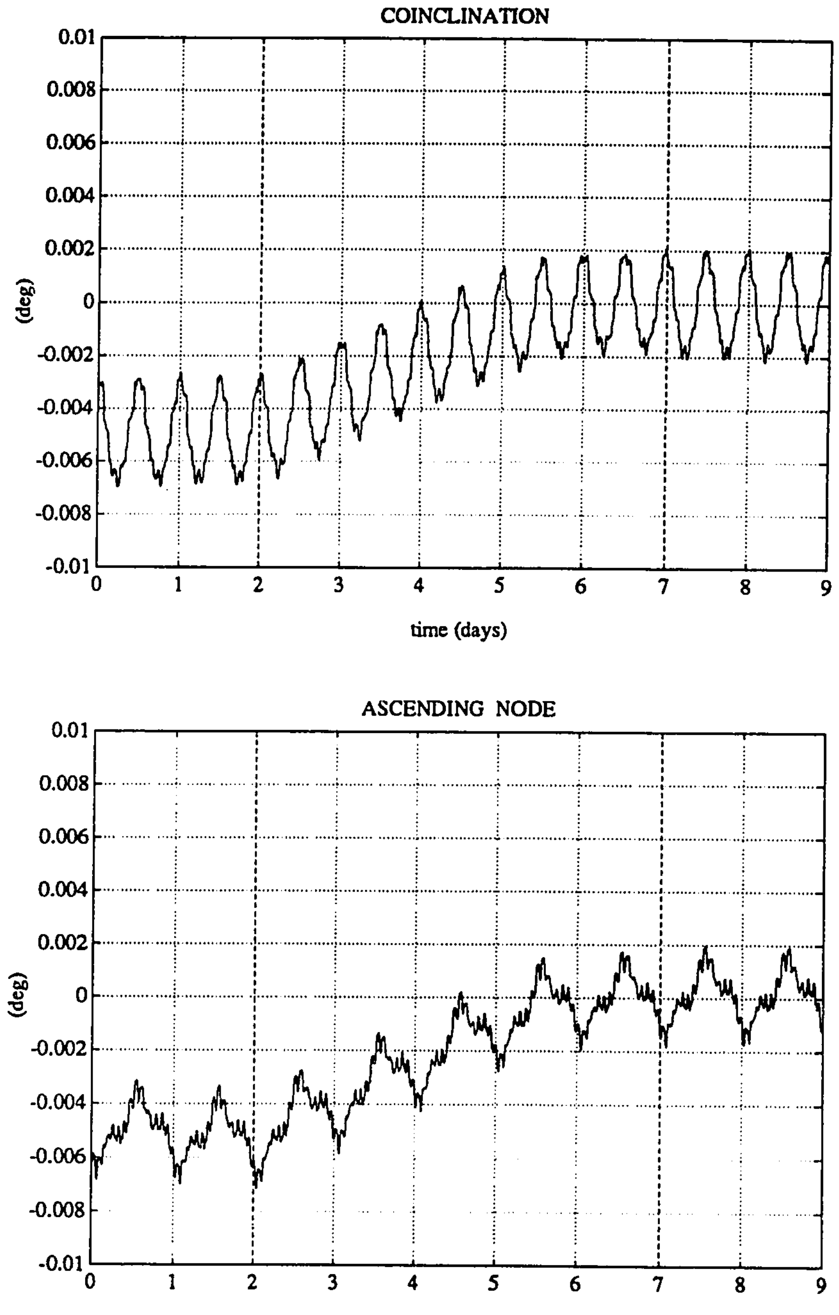

Figure 4.8 LQR Out-of-plane Control Results - 9 Days (CON6)

Initial conditions are good injection and GPS receiver is good. Same run as CON1 but with proportional feedback gains implemented instead of time optimal control.

4.6 In-Plane Time Optimal Control

In this section we investigate a time optimal control law to reduce the in-plane deviations from the target orbit. This is not as critical an effort as the adjustment of the orbit plane, thus it is likely that the orbit trim system will be turned off before the precise in-plane target elements are achieved. First the algorithm is described, and then performance results are presented.

4.6.1 Algorithm

The in-plane orbit dynamics are described by the following pair of coupled linear second order differential equations.

$$\begin{aligned} \ddot{x}_H - 2\, n_R\, \dot{y}_H - 3\, n_R^2\, x_H &= a_{cx} \\ \ddot{y}_H + 2\, n_R\, \dot{x}_H &= a_{cy} \end{aligned} \tag{4.9}$$

We are interested in driving the radial velocity to zero and having it stay there after the control is turned off, i.e.

$$\begin{aligned} &2n_R\, \dot{y}_H(t_f) + 3n_R^2\, x_H(t_f) = 0 \\ &\dot{x}_H(t_f) = 0 \end{aligned} \tag{4.10}$$

If we define q_1 and q_2 as the terms of interest, namely,

$$\begin{aligned} q_1 &\equiv -\frac{(2\ \dot{y}_H + 3\, n_R\, x_H)}{a_{max}} \\ q_2 &\equiv \frac{\dot{x}_H}{a_{max}} \end{aligned} \tag{4.11}$$

take derivatives, and substitute the expressions in Eq. 4.9, we find that the dynamics of q_1 and q_2 are represented by a harmonic oscillator, this time with two control inputs.

$$\begin{bmatrix} \dot{q}_1 \\ \dot{q}_2 \end{bmatrix} = \begin{bmatrix} 0 & n_R \\ -n_R & 0 \end{bmatrix} \begin{bmatrix} q_1 \\ q_2 \end{bmatrix} + \begin{bmatrix} 2\, u_1 \\ u_2 \end{bmatrix} \tag{4.12}$$

where a_{cx} and a_{cy} in Eq. 4.9 can be expressed as,

$$\begin{aligned} a_{cx} &= a_{max}\, u_2 \\ a_{cy} &= -\, a_{max}\, u_1 \end{aligned} \tag{4.13}$$

The in-plane control objective can then be formulated as follows. Compute controls $u_1(t)$ and $u_2(t)$ with magnitude less than or equal to 1, to bring q_1 and q_2 to zero in minimum time. Since the position within the orbit and the altitude are arbitrary, the problem has been reduced to second order. The additional variables correspond to a constant radial position offset and an integral of the along-track velocity.

Once again the solution is to use full control authority at all times, with the sign determined by two sets of switching curves in this case, as illustrated in Figure 4.8 [*Athans and Falb, 1966*]. The centers of the innermost scallops are located at $(nq_1, nq_2) = (\pm 1, \pm 2)$.

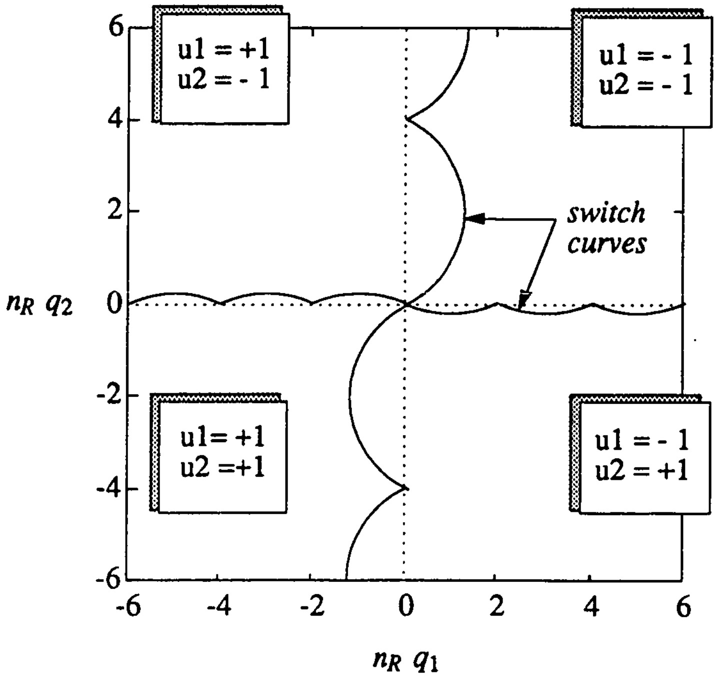

Figure 4.9 In-plane Time Optimal Switch Curves

Phase plane for in-plane states, q_1 and q_2. Location of the state in the phase plane determines the signs of the two control inputs.

The horizontal switch curve is defined by

$$n_R\, q_{2switch} = sign(q_1)\left\{ 2 - \sqrt{5 - [\,(\,|\,n_R\, q_1\,|\, mod\, 2) - 1]^2}\,\right\} \tag{4.14}$$

The vertical switch curve is defined by

$$n_R\, q_{2switch} = sign(q_1)\left\{ 2 - \sqrt{5 - [\,(\,|\,n_R\, q_1\,|\, mod\, 2) - 1]^2}\,\right\} \tag{4.15}$$

Figure 4.9 illustrates several optimal trajectories in the q_1, q_2 phase plane. The state evolves along a sequence of circular arcs whose center shifts clockwise among the points (+1,+2), (+1,-2), (-1,-2), (-1,+2), each time the switching curve is crossed. When the trajectory reaches the origin, the desired final state has been achieved. If the control is turned off at this point, the radial acceleration will be zero.

To implement the in-plane control algorithm, the q_1 and q_2 are computed based on the Hill state estimates provided by the navigation processor. The appropriate values of u_1, and u_2 are computed based on the location of the state in the phase plane. The actual controller commands, a_{cx}, and a_{cy} are then determined using Eq. 4.13.

4.6.2 Closed Loop Performance

The in-plane control algorithm was implemented in the closed loop computer simulation. In all cases the target mean values of the eccentricity vector components were, $\xi = 0.0000$, and $\eta = 0.0011$. In the first simulation (CON1), the initial conditions were set to the good injection values specified in Table 3.3, and the good GPS errors were used. Figure 4.11 shows the evolution of the instantaneous eccentricity vector over the nine-day run. For the first two days the control was off. It was then turned on for five days, and off again for two more. The figure eight pattern caused by the

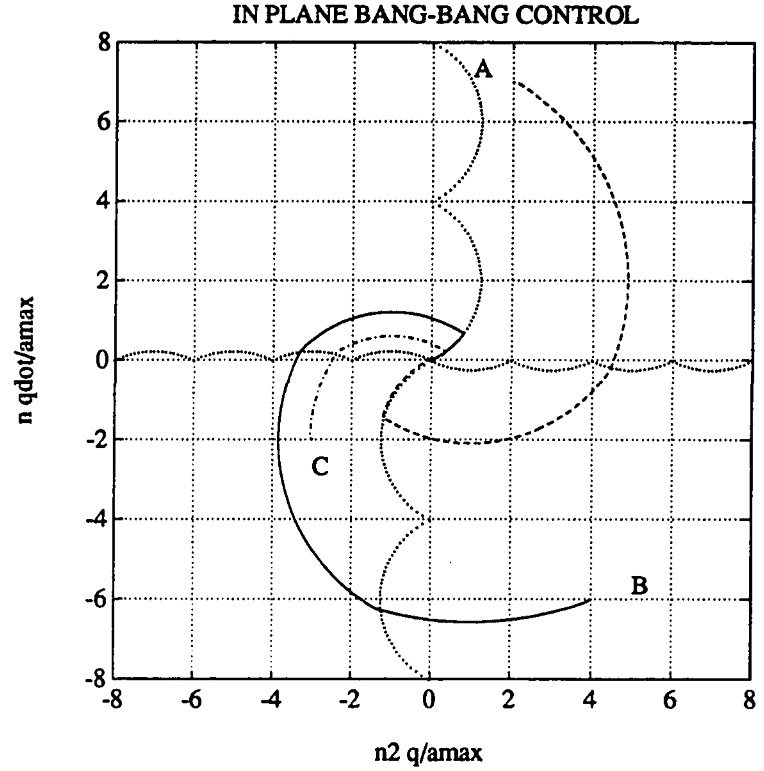

Figure 4.10 Time Optimal Trajectories for In-plane Control.

Curves A, B, and C show optimal trajectories for three arbitrary starting conditions.

Earth oblateness dominates the graph; however one can see the motion of the center of the pattern from its initial location at approximately (0.005, 0.005) toward the desired value of (0.000, 0.0011). Figure 4.12 shows a similar result for the 14 day run starting with the poor injection conditions (CON2).

To focus on the motion of the mean eccentricity, the results were averaged over daily intervals. Figure 4.13 shows the motion of the daily mean eccentricity vector for the two runs just described. During the two days prior to the start of control and the two days following, the mean vector moves along a circular arc centered at the frozen

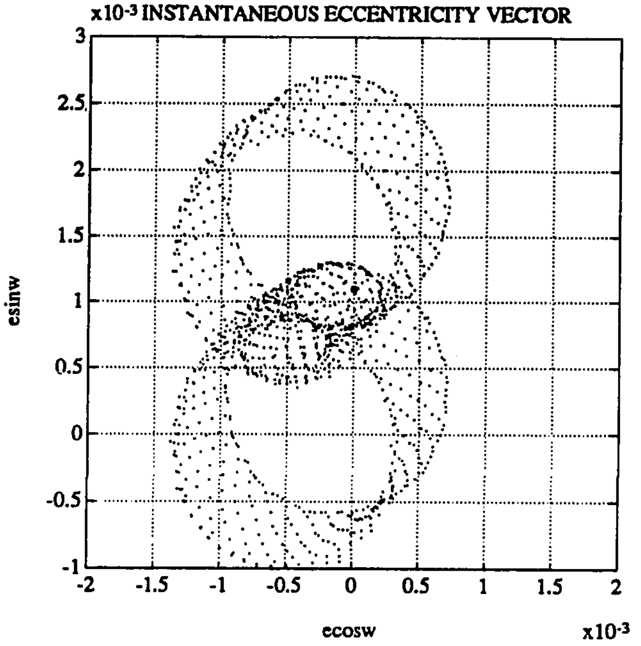

Figure 4.11 In-plane Time Optimal Control Results - 9 Days (CON1).

Good GPS receiver, good injection conditions. Each dot represents the instantaneous eccentricity vector averaged over a 10 minute storage interval. Dark circle indicates target mean value. Control off days 1-2, Control on days 3-7. Control off days 8-9.

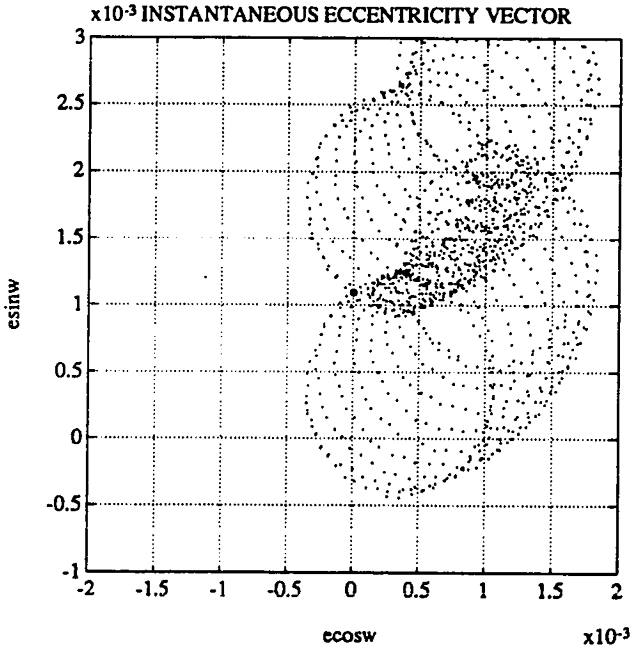

Figure 4.12 In-plane Time Optimal Control Results - 14 Days (CON2).

Good GPS receiver, poor injection conditions. Each dot represents the instantaneous eccentricity vector averaged over a 10 minute storage interval. Dark circle indicates target mean value. Control off days 1-2, Control on days 3-12. Control off days 13-14.

eccentricity. Recall that this rotation of the direction of the perigee has a period of 101 days and is caused by the Earth oblateness as was illustrated in Figure 2.22. The path that the eccentricity ***would have taken*** in the absence of control is indicated by the solid lines. The actual path is shown with "+". Thus the bang-bang control algorithm was quite successful in reducing the deviations from the target within the orbit plane, and the requirements specified in Table 2.11 were easily met.

As in the out-of-plane simulation studies, no significant difference between the closed loop results with the good and poor GPS receivers were found. Thus these results are not shown here.

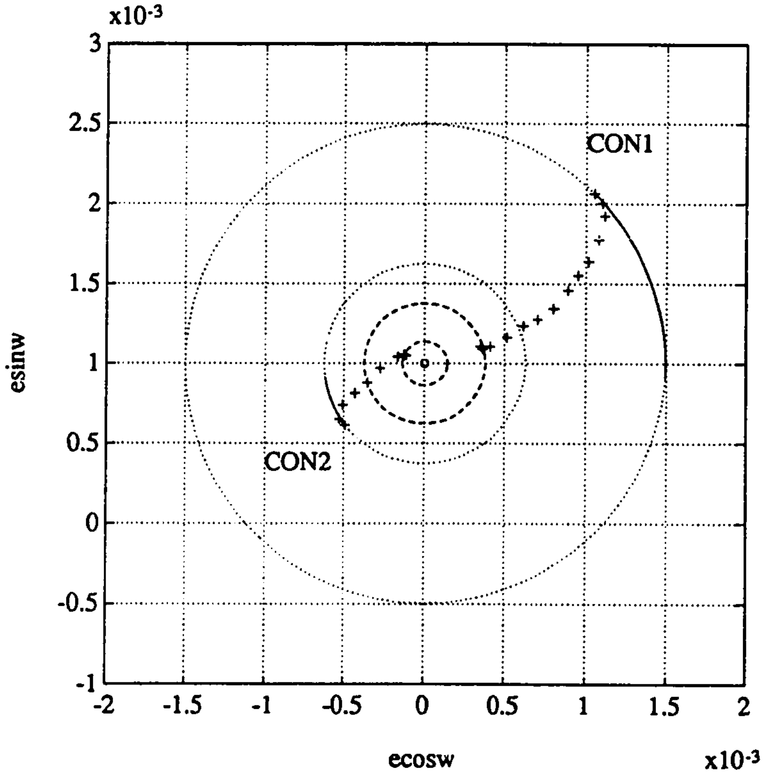

Figure 4.13 In-plane Results Mean Eccentricity.

Daily average values of the eccentricity the vector for runs shown in Fig. 4.10 (CON1) and Fig. 4.11 (CON2). "+" are actual daily mean values. Solid lines show the path which the e vector would have followed if the control was not turned on. Dashed lines indicate the expected long term path of the eccentricity due to the Earth oblateness and odd harmonics.

4.7 Closed Loop Control System Summary

The simulation results indicate that the time optimal closed loop orbit trim system using the onboard helium thrusters can successfully correct typical injection errors produced by the Delta II launch vehicle in under 10 days of operation. Final errors in the mean coinclination and node were less than 2×10^{-4} deg. These errors are due primarily due to approximations made in specifying the target orbit, and the low level of control authority. Similar results were obtained for both the good and bad GPS receivers. From these results it does not appear that a high quality GPS receiver will be necessary for orbit trimming.

Out-of-plane elements were corrected to within the requirements in the same period of time. Other effects which were not modeled here including actual thruster response dynamics, and spacecraft attitude dynamics are not expected to have a significant influence on the results.

CHAPTER 5. SUMMARY AND CONCLUSIONS

5.1 Overview

The closed loop orbit trim system study presented here can be described as both very specific to Gravity Probe B and very generic in its potential applications. In general, it represents the design of an onboard system for performing extremely accurate orbit adjustments without the need for ground support. In the particular application to GP-B, it is a system to correct the orbit injection errors introduced by the Delta II launch vehicle, using the onboard helium thrusters.

This chapter summarizes the system design and results for GP-B in each of the three areas considered, namely orbit modeling, navigation, and orbit trim. It also recommends future efforts necessary for a full implementation on GP-B, and suggests extensions of this work to other applications.

5.2 GP-B Orbit Modeling

The requirements on the GP-B orbit were clearly defined; the most important of which is that the orbit plane not deviate by more than about ±500 m from the direction to the guide star, Rigel. Deviations from this orientation produce Newtonian drifts in the gyros due to gravity gradient torques which do not average to zero over an orbit. The orbit plane should also be polar to within ± 50 m in order to separate the geodetic and frame-dragging drifts, and preclude rotation of the orbit plane due to J_2. The requirement on the altitude of the orbit is fairly lax (± 5 km), and is driven primarily by the ability of the drag compensation system to overcome the atmospheric disturbances. The target altitude may also be adjusted to avoid low order resonances. Maximum eccentricity should be kept small to avoid large altitude variations.

To satisfy these long term orbit requirements, target values for the orbit elements were derived based on simulations of the motion over the 18 month mission. The effects of the higher Earth harmonics, the Sun and Moon, the tides, and the precession of the equinoxes were included. The target values for coinclination and node depend on the launch year because of the variation in the lunar orbit plane. The allowable injection error in coinclination is $\pm 2 \times 10^{-4}$ deg (25 m), and in node $\pm 2 \times 10^{-3}$ deg (250 m). This is far beyond the capability of the Delta II launch vehicle. The target eccentricity vector points northward and has a magnitude of 0.00133. This frozen value is produced by the interaction of the Earth oblateness and odd zonal terms.

Low order terms in the Earth's gravitational field cause periodic variations which dominate the short term motion. The in-plane elements vary once per orbit primarily due to the effects of J_2. The coinclination varies twice daily due to $J_{2,2}$ and the node has a variation composed of a once daily and three times daily oscillation caused by $J_{4,1}$ and $J_{4,3}$.

Further work must be done to refine the orbit modeling begun here. In particular, the effects of near resonance terms should be examined in more detail to insure that the selected altitude of 650 km is in fact, acceptable from this standpoint. Similarly, a more elaborate tidal model should be introduced

The orbit modeling performed here is quite useful for approximating the long term motions and specifying the injection conditions and required accuracies. As GP-B nears its launch date, a higher fidelity model of the orbit evolution will be necessary to precisely determine the target injection values. A number of large, highly accurate orbit simulation programs exist at Goddard, JPL, and several universities. Such a proven resource should be employed to verify and enhance the predictions of the simpler models used here.

5.3. GPS Based Navigation System

The proposed navigation system for GP-B is based on GPS. The key feature of GPS is that it provides orbit information directly to the vehicle, thus eliminating the need for extensive ground support. Two GPS receiver types were investigated, a high accuracy version with access to the SA keys (5 m, 1-σ range, and 0.01 m/s, 1-σ range rate), and a lower accuracy version which would not have this benefit (correlated errors of 20-40 m range and 0.2 m/s range rate). The navigation performance of the more accurate receiver was of course better, but both were sufficient for the closed loop system operation. The conclusion is then that a standard C/A code SPS receiver is acceptable as the navigation sensor for the orbit trim segment of the mission.

The navigation system estimates the state of the vehicle by propagating a reference orbit which includes the short term effects of J_2, and a deviation from this reference. The deviation state is propagated using a Kalman filter and updated based on the GPS measurements. The semimajor axis and argument of latitude of the reference orbit are reset based on the current state estimates, since we are not concerned with the precise altitude or the position of the spacecraft within the orbit plane. The performance of the navigation system necessarily degrades if the actual orbit is far from the reference in either the out-of-plane direction or in eccentricity, since the dynamics of the deviation state have been linearized about the reference.

Further research needed to implement this system onboard GP-B involves four areas: coordinate frame transformations, GP-B attitude dynamics and its effect on signal reception at different antennas, antenna management, and improved models of GPS errors. The transformations needed to convert GPS satellite information into orbit element estimates were mentioned in Section 3.3. These must be worked out in detail to ensure that errors in the uncertainty of this transformation do not exceed the estimation requirements. Attitude dynamics relates to the assumption made here that measurements are taken at the center of mass of the vehicle. In particular, one must evaluate the effect of the tangential velocity of the antennas located on the tips of the solar panels of the rolling spacecraft on the GPS doppler measurements (~ 1 cm/s). One must compensate for this motion in the data reduction in order to achieve the measurement accuracies required for geodesy. This may become a critical area of investigation given current considerations of decreasing the spacecraft roll period from 10 min to 3 min [*Everitt, 1990*].

It is clear that GPS will be used as a navigation aid on a wide variety of spacecraft and other vehicles. The navigation scheme developed here is directly applicable to a near Earth spacecraft such as a space station using onboard navigation for tagging of measurements or as part of a closed loop orbit adjust system. A similar system could be developed for more maneuverable vehicles such as orbital transfer vehicles or the shuttle; however, in this case the reference orbit must be adjusted based on the vehicle trajectory.

5.4. Closed Loop Orbit Trim

The closed loop orbit trim system consists of the GPS based navigation system, and a time optimal control algorithm which issues commands to the onboard helium thrusters. Simulations indicated that typical Delta II orbit injection errors could be corrected within about 10 days of controller operations. The final mean orbit errors satisfy the orbit injection requirements specified in the orbit modeling section. Peformance of the system was virtually identical using either the high or the low accuracy GPS receiver models.

The out-of-plane control algorithm accounts for the oscillations in the coinclination and node produced by the low order Earth harmonics by finding the deviations from a control reference orbit. These deviations are represented by a harmonic oscillator, and are driven to zero by commanding full control authority (5×10^{-6} m/s^2) at all times with the direction determined by a scalloped switching curve. The in-plane control algorithm eliminates the radial velocity and acceleration using bang-bang control commands in the radial and tangential directions. The eccentricity vector is brought to the frozen value within the allowable error bounds.

This type of a closed loop orbit trim system is vital for GP-B. It will be virtually impossible to achieve the necessary orbit injection accuracies using only ground commanded controls.

Further work on the GP-B orbit trim system should involve more accurate modeling of the onboard helium thrusters and their response to commands. In this work, it was assumed that commands could be issued in each of the three axes of the navigation frame. In actuality, commands to individual thrusters must be determined so as to control both translation and attitude motions of the vehicle. The true test of the trim system design will be to incorporate it in an overall GP-B system simulation now under development.

One important aspect of this work has been its general applicability to a host of orbit trim applications. A similar system could easily be implemented on an Earth observation satellite requiring periodic or continuous orbit adjustments. In this case the controller cost function would likely be changed to include a penalty for fuel consumption. Similar closed loop guidance schemes could be used for other low thrust vehicles such as a space tug, and applications to higher thrust and greater maneuverability vehicles could also be developed which would improve efficiency and injection accuracy.

REFERENCES

Allan, R. R. (1967a), "Resonance effects due to the longitude dependence of the gravitational field of a rotating primary-I," *Planet. and Space Sciences*, Vol. 15, pp. 53-76.

Allan, R. R. (1967b), "Satellite resonance with longitude-dependent gravity-II; effects involving the eccentricity," *Planetary and Space Sciences*, Vol. 15, pp. 53-76.

Allan, R. R. (1973), "Satellite resonance with longitude-dependent gravity-III; inclination changes for close satellites," *Planet. and Space Sciences*, Vol. 21, pp. 205-225.

Athans, M. and P. L. Falb (1966), *Optimal Control: An Introduction to the Theory and Its Applications*, McGraw-Hill Inc., New York.

Battin, R. H. (1987), *An Introduction to the Mathematics and Methods of Astrodynamics*, New York, AIAA Inc.

Blitzer, L. (1966), "Satellite resonances and librations associated with tesseral harmonics of the geopotential," J. of Geophysical Research, Vol. 71, No. 14, pp3557-3565.

Breakwell, J. V. (1987), Stanford University Class Notes, *Advanced Space Mechanics AA279B*.

Broucke, R. A. and P. J. Cefola (1972), "On the equinoctial orbit elements," *Celestial Mechanics*, Vol. 5, pp. 303-310.

Bryson, A. E. and Y.C. Ho (1975), *Applied Optimal Control*, Hemisphere Publ. Corp.,Washington, D.C.

Bull, J. S. (1973), "Precise attitude control of the Stanford Relativity Satellite," Ph. D. Dissertation Stanford University, Center for Systems Research, SUDAAR No. 452

Chen, J. H. (1983), "Helium thruster propulsion system for precise attitude control and drag compensation of the Gravity Probe-B satellite," Stanford Ph. D. Dissertation.

Chou, H. T. (1990), "An anti-SA filter for non-differential GPS users," Presented at the ION GPS 90 meeting, Colorado Springs.

Cohen, C. E., G. M. Keiser, and B. W. Parkinson (1990), "Tracking Gravity Probe B gyroscope polhode motion," Reprint from the *Proceedings of the AIAA Guidance, Navigation, and Control Conference*, AIAA Paper 90-3419, Portland.

DeBra, D. B. (1973), "Disturbance compensation system design," APL Technical Digest, **12**, 2, 14-26.

Duhamel, T. G. (1984), "Contributions to the error analysis in the relativity gyroscope experiment," Ph. D. Dissertation Stanford University, Dept. of Aero. & Astro. and Dept. of Physics, SUDAAR No. 540.

Everitt, C. W. F. (1980), "Report on a program to develop a gyro test of General Relativity in a satellite and associated control technology," Internal report known as *the Green Book*, Stanford University.

Everitt, C. W. F. (1990), Private conversation on October 2, 1990.

Feteih, S. (1989), "Dynamically testing of GP B electrostatically levitated spherical gyroscopes," Ph. D. Dissertation Stanford University, Dept. of Aero. & Astro.

Goad, C. C. (1987), "An efficient algorithm for the evaluation of inclination and eccentricity functions," *Manuscripta Geodaetica*, Vol. 12, No. 1, pp. 11-15.

Green, G. B., et al. (1989), "The GPS 21 primary satellite constellation," *Navigation*, Vol. 36, No. 1.

Green, G. B. (1990), private conversation based on meeting with representatives from McDonnell Douglas Inc.

Hagerman, L. L. (1973), "Effects of multipath on coherent and noncoherent PRN ranging receivers," Aerospace Report No. TOR-0073-(3030-30)-03, The Aerospace Corporation.

Institute of Navigation (1980), *Global Positioning System Vol I*, Papers published in Navigation, Reprinted by the ION, Washington, D.C.

Institute of Navigation (1984), *Global Positioning System Vol II*, Papers published in Navigation, Reprinted by the ION, Washington, D.C.

Institute of Navigation (1987), *Global Positioning System Vol III*, Papers published in Navigation, Reprinted by the ION, Washington, D.C.

Jafry, Y. R. (1989), "Progress report 2 on GP-B aeronomy experiment," GP-B internal report, Sep. 6.

Jekeli, C. ed. (1990), *Proceedings of the Second Symposium on GPS Applications in Space*, Environmental Research Papers, No. 1052, GL-TR-90-0032, Geophysics Lab (AFSC), MA.

Kaplan, M. H. (1976), *Modern Spacecraft Dynamics and Control*, J. Wiley & Sons, New York.

Kasdin, N. J. and G. M. Keiser, "Revised Gravity Probe B satellite acceleration specifications," GP-B internal memo, Sept. 1990.

Kaula, W.H. (1966), *Theory of Satellite Geodesy*, Blaisdell, Waltham, MA.

Kechichian, J. A. (1989), "Analytical solution of terminal rendez-vous in near-circular orbit around the oblate Earth," Reprint from the *40th Congress of the IAF*, Malaga, Spain, IAF-89-365.

Kostelecky, J., J. Klokocnik, and Z. Kalina (1986), "Computation of normalized inclination function to high degree for satellites in resonances," *Manuscripta Geodaetica*, Vol. 11, No. 4, pp. 293-304.

Kremer, G. T., et al. (1990), "The effect of selective availability on differential GPS corrections," *Navigation*, Vol. 37, No. 1.

Langley, R. B. (1990), "Why is the GPS signal so complex ?," *GPS World,* May/June 1990, pp. 56-59.

Lerch, F. J., et al. (1981),"Goddard Earth models for oceanographic applications (GEM10b and 10c)," *Marine Geodesy*, 5, 2, pp145-187.

McDonnell Douglas Inc. (1989), "Commercial Delta II Payload Planners Guide", McDonnell Douglas Commercial Delta, Inc. MDC H3224B.

Milliken, R. J. and C. J. Zoller (1980), "Principle of operation of NAVSTAR and system characteristics," in *Global Positioning System Vol. I*, pp.3-14, Inst. of Navigation.

NASA Technical Memorandum 4019 (1988), *An Improved Model of the Earth's Gravitational Field: *GEM-T1**.

Naval Observatory (1985), *The Astronomical Almanac*, U.S. Goverment Printing Office, Washington DC.

Navtech Seminars Inc. (1987), Notes from "Fundamental of GPS and Glonass," Course 152, Alexandria, VA.

Parkinson, B. W., C. W. F. Everitt, and D. B. DeBra (1986), "The Stanford Relativity Gyro Experiment," *Guidance and Control, Advances in the Astronautical Sciences*, Vol. 63, AAS.

Parkinson, B. W., et al. (1987), "The prototype design of the Stanford Relativity Gyro Experiment," *38th Congress of the International Astronautical Federation*, Brighton, IAF-87-458.

Parkinson, B. W., and P. Axelrad (1987), "A basis for the development of operational algorithms for simplified GPS integrity checking," *ION Satellite Division Meeting*, Colorado Springs, CO.

Parkinson, B. W., and P. Axelrad (1988), "Autonomous GPS integrity monitoring using the pseudorange residual," *Navigation*, Vol. 35, No. 2.

Parkinson, B. W., and N. J. Kasdin (1988), "Twenty milliarsec pointing system for the rolling GP-B spacecraft," Guidance and Control 1988, Vol. 66, *Advances in the Astronautical Sciences*.

Parkinson, B. W., and K. T. Fitzgibbon (1989), "Aircraft automatic landing systems using GPS," *Navigation*, Royal Inst. of Nav., Vol. 42, No. 1.

Parkinson, B. W., and J. R. Crerie, "Phase-lock roll control for inertially-pointing spacecraft by correlations of star intensity profiles with a stored reference," *Proceedings of 13th Annual AAS Guidance and Control Conference*, Keystone, CO.

Qin, X., J. V. Breakwell, and B. W. Parkinson (1989), "Science Mission Data Reduction for the Stanford Relativity Gyro Experiment," Reprint from *Proceedings of AAS/AIAA Astrodynamics Specialist Conference*, AAS 89-384, Stowe, VT.

Schaechter, D. B. (1977), "A theoretical analysis of a relativity mission with two counter-orbiting drag-free satellites," Stanford University Dept. of Aero. & Astro., SUDAAR No. 3781.

Small, H. (1963), "Satellite motion around an oblate planet," Reprint from *AIAA/AAS Astrodynamics Conference*, AIAA Paper 63-393, Yale.

Small, H. (1986), Lockheed Internal Doc., Question S-B-15, LMSC-F172421.

Tapley, M., et al. (1989), "Impact of the GP-B Mission on Satellite Navigation and Geodesy," *40th Congress of the International Astronautical Federation*, Malaga, Spain, IAF-89-354.

Vassar, R., et al. (1982a), "Orbit selection for the Stanford Relativity Gyroscope Experiment," *J. of Spacecraft and Rockets*, Vol. 19, No.1, p. 66.

Vassar, R. (1982b), "Error analysis for the Stanford Relativity Gyroscope Experiment," Ph. D. Dissertation Stanford University, Dept. of Aero. & Astro. and Dept. of Physics, SUDAAR No. 531.

Vassar, R. (1986), "Influence of proof mass to gyro spacing on experiment accuracy," LMSC Memorandum #011/F066213.

Wells, D., et al. (1986), *Guide to GPS Positioning,* Canadian GPS Associates, Fredericton, N.B., Canada.

Wertz, J. R. Ed. (1984), *Spacecraft Attitude Determination and Control*, D. Reidel Publishing Co., Boston.

Wiktor, P., J. H. Chen, and D. B. DeBra (1989), "Optimal thruster configurations for the GP-B spacecraft," *XI IFAC Symposium on Automatic Control in Aerospace*, Ibaraki, Japan.

Wiktor, P. (1990), "Thruster control for GP-B," GP-B internal report, Jan. 16, Stanford University.

Yekutiel, O. (1989), "GP-B orbit altitude," GP-B internal report, Apr. 28, Stanford University.